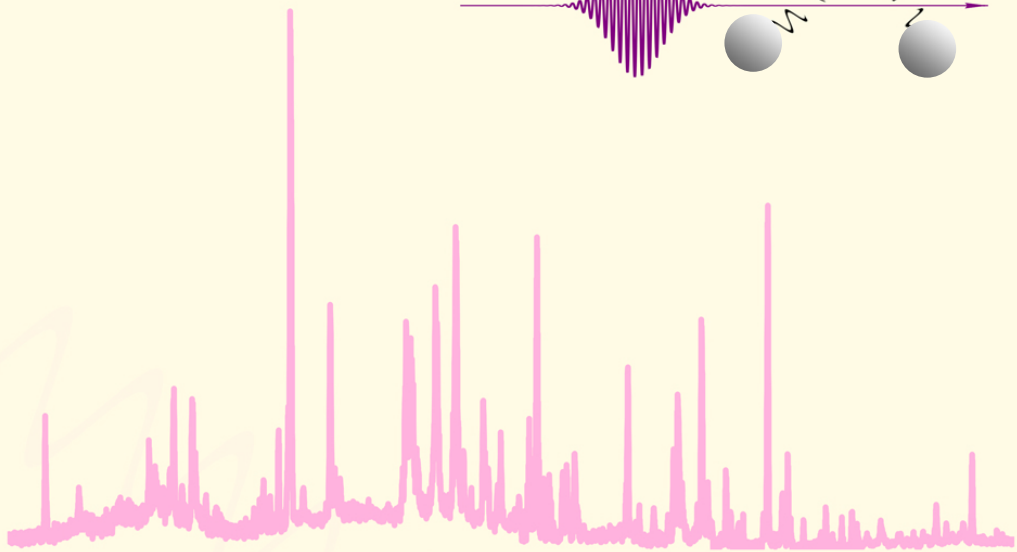
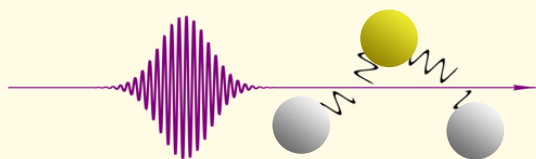


**Laser Precision Spectroscopy on
Hydrogen Isotopologues:
Tritiated molecules
and vibrationally excited H₂**



Kin Fung Lai

VRIJE UNIVERSITEIT

Laser Precision Spectroscopy on Hydrogen Isotopologues: Tritiated molecules and vibrationally excited H₂

ACADEMISCH PROEFSCHRIFT

ter verkrijging van de graad Doctor aan
de Vrije Universiteit Amsterdam,
op gezag van de rector magnificus
prof.dr. J. Geurts,
in het openbaar te verdedigen
ten overstaan van de promotiecommissie
van de Faculteit der Bètawetenschappen
op dinsdag 28 Juni 2022 om 11.45 uur
in de aula van de universiteit,
De Boelelaan 1105

door

Kin Fung Lai
geboren te Guangdong, China

promotor: prof.dr. W.M.G. Ubachs

copromotoren: dr. E.J. Salumbides
dr. M. Beyer

promotiecommissie: dr. J. Rojo
dr. N.J. van Druten
dr. S. Bruenken
prof. E. Matyus
prof.dr. H.L. Bethlem

Contents

1	Introduction	1
1.1	Theory of molecular hydrogen	2
1.2	Tritium-containing isotopologues	4
1.3	Vibrationally excited state and quasi-bound resonance of H ₂	6
1.4	Outline of this thesis	9
2	Precision tests of nonadiabatic perturbation theory with measurements on the DT molecule	13
2.1	Introduction	14
2.2	Experiment	15
2.3	Theory	18
2.4	Discussion and Summary	22
3	Precision measurement of the fundamental vibrational frequencies of T₂, DT, HT	25
3.1	Introduction	26
3.2	Experiment	27
3.2.1	Tritium gas samples	28
3.2.2	Precision CARS setup	29
3.2.3	Frequency calibration	31
3.2.4	ac-Stark shift	33
3.2.5	Pressure shift	35
3.2.6	Frequency uncertainty in the CARS measurements	35
3.3	Results and Discussions	36
3.3.1	HT, DT and T ₂ transitions	37
3.3.2	Benchmark measurements on D ₂	42
3.3.3	Comparison with calculations	42
3.4	Lineshape analysis	43
3.4.1	Saturation CARS spectroscopy	43
3.4.2	Asymmetric profile of weak transitions	45
3.4.3	Lineshape simulation for interference effects	48
3.4.4	Lineshape fitting	52
3.5	Conclusion and outlook	53
4	Two-photon Doppler-free ultraviolet laser spectroscopy on sulphur atoms	57
4.1	Introduction	58
4.2	Experiment	58
4.3	Results and Interpretation	60
4.4	Discussion: Level energies	63

4.5	Conclusion	66
5	Photolysis production and spectroscopic investigation of the highest vibrational states in H_2 ($X^1\Sigma_g^+$ $v = 13, 14$)	69
5.1	Introduction	70
5.2	Experiment	71
5.3	Results	74
5.4	Discussion	78
5.5	Conclusion	83
6	Shape resonances in H_2 as photolysis reaction intermediates	85
6.1	Introduction	86
6.2	Experiment	88
6.3	Theory	90
6.4	Results and Discussions	91
7	Precision measurement of quasi-bound resonances in H_2 and the $\text{H} + \text{H}$ scattering length	99
7.1	Introduction	100
7.2	Experimental	102
7.3	Theory	107
7.3.1	The $X^1\Sigma_g^+$ state	107
7.3.2	The $F^1\Sigma_g^+$ state	113
7.4	Detection, identification and precision measurement of the quasi-bound resonances	113
7.5	Discussion	120
7.5.1	Test of the H_2 potential	120
7.5.2	$\text{H} + \text{H}$ scattering	126
7.6	Conclusion	128
8	Summary and outlook	131
	Bibliography	135
	List of publications	159
	Acknowledgment	161

Introduction

Hydrogen gas was discovered before the 18th century from the reaction of acid with metals by various scientist such as Philippus Aureolus Paracelsus, Turquet De Mayerne and Robert Boyle [1]. Cavendish was the first one to publish studies on the generation of hydrogen gas from the reaction of sulfuric acid and zinc, iron and tin metals [2]. Hydrogen has shown many applications, especially in petroleum industry and chemical industry [3]. Most of the uses are based on the power of "hydrogenation", such as hydrocracking and desulphurization in oil refinery industry. Recently, hydrogen is drawing more attention as an energy carrier for the goal of decarbonization [4].

Hydrogen also plays an important role in research of fundamental physics as the subject of this thesis. H_2 is the simplest neutral molecule consisting of two protons and two electrons. Because of its simplicity, it serves as a benchmark molecule for testing quantum chemical theories. Since the introduction of quantum mechanics to molecular systems in the 1920's, a tremendous improvement in the precision of theoretical calculations of the H_2 system has been achieved. Heitler and London proposed the valence-bond theory by assuming the interatomic interaction as a perturbation of two isolated H atoms [5]. Later in 1933, James and Coolidge suggested the variational method with a set of basis functions in elliptical coordinates, suitable for two-center problems like H_2^+ , to calculate the binding energy of H_2 with uncertainty only 0.02 eV and showed good agreement with the experimental value [6]. Starting in the 1960's, a series of papers by Kołos and Wolniewicz presented the most extensive calculation on ground and excited electronic states of H_2 and its isotopologues, including relativistic and QED corrections [7–14]. In the past decade, further improvements on the calculations were achieved by Pachucki and coworkers using a perturbative approach to calculate separately the Born-Oppenheimer (BO) energies [15], adiabatic and non-adiabatic corrections [16, 17], relativistic and quantum electrodynamic corrections [18, 19]. Until now, the calculation uncertainty of the H_2 binding energy is as accurate as 10^{-4} cm⁻¹. This has been made possible by implementing a pre-BO approach of nonrelativistic energy [20–22].

On the experimental side, the determination of the H_2 dissociation energy in $X^1\Sigma_g^+$ state was improved alongside with the theoretical accuracy. The H_2 dissociation energy was determined by spectroscopic techniques starting from Witmer [23] using the anharmonicity constant. Later, Herzberg was inspired by Beutler [24] and determined the $n = 2$ dissociation limit from the onset

of the absorption continuum of the Werner band [25], presenting a 0.3 cm^{-1} uncertainty. Eyler and coworkers used laser double resonance spectroscopy to reach the onset of the dissociation continuum and improve the accuracy of dissociation energy to $0.010 - 0.016 \text{ cm}^{-1}$ for all stable isotopologues [26, 27]. The next generation of dissociation energy measurements started by Liu and coworkers with the determination of ionization energy of H_2 with only 0.00037 cm^{-1} uncertainty [28]. Using a similar scheme, the uncertainty of the dissociation energy of H_2 was reduced to about $3 \times 10^{-5} \text{ cm}^{-1}$ over the past decade [29]. Aside from the dissociation energy, the measurements of ro-vibrational transitions have been greatly improved, such as the fundamental bands of HD and D_2 [30,31] and overtone transitions on all stable isotopologues [32–40].

This thesis will present two distinct topics of precision spectroscopic measurement of rarely studied isotopologues of molecular hydrogen and highly ro-vibrationally excited levels of molecular hydrogen to test theoretical calculations, with a specific focus on the non-adiabatic contributions. In the following section, a brief introduction of the theoretical framework to obtain molecular hydrogen level energies will be presented.

1.1 Theory of molecular hydrogen

The nonrelativistic Hamiltonian for molecular hydrogen and isotopologues in their center-of-mass frame, with the geometric center of the nuclei as origin, is given by

$$H = H_{\text{el}} + H'_1 + H'_2 + H'_3, \quad (1.1)$$

where

$$H_{\text{el}} = -\frac{1}{2}(\nabla_1^2 + \nabla_2^2) - \frac{1}{r_{1a}} - \frac{1}{r_{1b}} - \frac{1}{r_{2a}} - \frac{1}{r_{2b}} + \frac{1}{R}, \quad (1.2)$$

$$H'_1 = -\frac{1}{2\mu_n} \nabla_R^2, \quad (1.3)$$

$$H'_2 = -\frac{1}{8\mu_n} (\nabla_1 + \nabla_2)^2 \quad \text{and} \quad (1.4)$$

$$H'_3 = -\frac{1}{2} \left(\frac{1}{M_a} - \frac{1}{M_b} \right) \nabla_R \cdot (\nabla_1 + \nabla_2). \quad (1.5)$$

All the terms are presented in atomic units. Labels 1,2 denotes the electrons while a, b are for nuclei, R denotes the internuclear separation and r_{ij} the separation of particle i and j . The nuclear reduced mass is defined as $\mu_n = (1/m_a + 1/m_b)^{-1}$. H_{el} contains the electronic kinetic energy in the

center-of-mass frame of the nuclei and all potential energy terms. H'_1 , H'_2 and H'_3 represent the relative motion of the nuclei, the coupling between nuclear and electronic motion, while H'_3 is only non-vanishing for heteronuclear isotopologues, HD, HT and DT, resulting in *gerade/ungerade* (*g/u*) electronic state mixing.

However, solving this Hamiltonian is computationally intensive. One way to simplify the problem is by neglecting the coupling of the fast electronic motion and the slow nuclear motion, known as the Born-Oppenheimer (BO) approximation. The total wavefunction $\Psi(\vec{r}_1, \vec{r}_2, \vec{R})$ is represented as the product of electronic $\phi(\vec{r}_1, \vec{r}_2; R)$ and nuclear wavefunction $Y(\vec{R}/R)\chi(R)/R$, $\Psi(\vec{r}_1, \vec{r}_2, \vec{R}) = \phi(\vec{r}_1, \vec{r}_2; R)Y(\vec{R}/R)\chi(R)/R$, where $Y(\vec{R}/R)$ are spherical harmonic functions. H_{el} is solved separately to give the clamped nuclei potential as a function of the internuclear distance,

$$(H_{\text{el}} - \mathcal{E}_{\text{el}}(R))\phi(\vec{r}_1, \vec{r}_2; R) = 0. \quad (1.6)$$

The BO energy of a ro-vibrational level in a given electronic state and with rotational angular momentum J is obtained by solving

$$\left[-\frac{1}{2R^2} \frac{\partial}{\partial R} \frac{R^2}{\mu_{\text{vib}}} \frac{\partial}{\partial R} + \frac{J(J+1)}{2\mu_{\text{rot}}R^2} + \mathcal{E}_{\text{el}}(R) - E \right] \chi(R) = 0, \quad (1.7)$$

where vibrational reduced mass μ_{vib} and rotational reduced mass μ_{rot} equals μ_n . The correction to the BO energy arises from the nuclear and electronic motions and can be treated by a perturbative approach. In first order, a specific electronic state may couple with the nuclear motion, but not mixing between different electronic states. This gives the adiabatic correction $\mathcal{E}_a(R)$ to the clamped nuclear potential $\mathcal{E}_{\text{el}}(R)$, where $\mathcal{E}_a(R) = \langle \phi | H'_1 + H'_2 | \phi \rangle$. Wolniewicz has mentioned that the sum of $\mathcal{E}_{\text{el}}(R)$ and $\mathcal{E}_a(R)$ is sometimes called the best potential energy curve for diatomic molecule at a given electronic state [9]. In the recent studies, Pachucki and coworkers introduced the non-adiabatic perturbation theory (NAPT) to calculate the leading-order non-adiabatic correction of all bound levels in the ground electronic $X^1\Sigma_g^+$ state. This is done in the form of an additional potential $\delta\mathcal{E}_{na}(R)$ and the R -dependent rotational and vibrational reduced masses [15, 17, 41]. In the NAPT formalism, the nonrelativistic energy $E^{(2)}$ is expanded as

$$E^{(2)} = E^{(2,0)} + E^{(2,1)} + E^{(2,2)} + O\left(\left(\frac{m_e}{\mu_n}\right)^3\right), \quad (1.8)$$

where $E^{(2,0)}$ represents the BO energy, $E^{(2,1)}$ represents the adiabatic correction and $E^{(2,2)}$ is the leading-order non-adiabatic correction. Equation (1.8)

is expanded in powers of (m_e/μ_n) , where $E^{(2,1)}$ preserves terms with (m_e/μ_n) and $E^{(2,2)}$ preserves terms with $(m_e/\mu_n)^2$. The uncertainty is limited by the next higher order non-adiabatic correction and estimated to be $E^{(2,2)}m_e/\mu_n$. Pachucki and coworkers have published the program, H2SPECTRE, to perform NAPT calculations of the level energies and the ro-vibrational transition frequencies of all isotopologues [22]. Recently, they employed the pre-BO scheme to calculate nonrelativistic energies for selected levels in several isotopologues with only 10^{-7} cm^{-1} uncertainty [42–45], which are also included in the H2SPECTRE program.

At this level of accuracy, the contribution of relativistic and QED effects need to be considered. The level energies of hydrogen molecules can be expanded perturbatively into powers of the fine-structure constant α [22, 46, 47]

$$E = m\alpha^2 E^{(2)} + m\alpha^4 \left(E^{(4)} + E_{FS} \right) + m\alpha^5 E^{(5)} + m\alpha^6 E^{(6)} + \dots \quad (1.9)$$

The expansion terms correspond to nonrelativistic energy $E^{(2)}$, leading-order relativistic correction $E^{(4)}$, leading-order QED correction $E^{(5)}$ and higher order QED corrections. E_{FS} denotes the correction due to the non-zero electronic wavefunction inside the finite size nucleus. Individual terms can be further expanded into powers of (m_e/μ_n) to separate out the finite-mass correction, for example in Equation (1.8). Most of these terms are evaluated under the BO approximation and the uncertainties are estimated to be $E^{(i)}m_e/\mu_n$. At present $E^{(2)}$ has been evaluated to very high accuracies, so that the largest uncertainty contributions are from the leading-order QED corrections, $E^{(5)}$ and $E^{(7)}$ terms, which amount to 10^{-4} and 10^{-5} cm^{-1} , respectively. However, this estimation method is not guaranteed. In 2017, the recalculations of the leading-order relativistic correction led to a disagreement of dissociation energies between the experimental [28, 48, 49] and theoretical value for the stable isotopologues [18]. The revision of the experimental value of the H_2 dissociation energy with an improved accuracy of the $\text{EF}^1\Sigma_g^+ - \text{X}^1\Sigma_g^+$ transition [50], or an improved ionization energy of H_2 via $\text{GK}^1\Sigma_g^+ - \text{X}^1\Sigma_g^+$ and $56p\ 1_1$ transitions [51], still showed disagreement with the theoretical value, which suggested that the problem was in the calculation. Later in 2018, Wang et al. and Pachucki et al. found the non-adiabatic relativistic correction is 10 times larger than previously estimated [21, 52]. The discrepancy between experimental and calculation values of H_2 and D_2 dissociation energy can be explained by this missing term in the calculation, while the discrepancy for HD remains unresolved.

1.2 Tritium-containing isotopologues

In contrast to typical stable isotopologues H_2 , HD and D_2 , tritium-containing isotopologues, HT , DT and T_2 , are rarely studied experimentally due to its

handling difficulties.

Tritium is a radioactive isotope of hydrogen. Its nucleus consists of 1 proton and 2 neutrons, and is about three-times heavier than hydrogen. Tritium was first discovered in the 1930's by Oliphant from the bombardment of deuterated compounds with deuterium nuclei [53]. The radioactive nature of tritium was then found by Alvarez and Cornog [54]. The tritium nucleus will undergo β -decay



with a half-life of 12.3 years [55]. A natural source of tritium on Earth is the bombardment of air with cosmic rays [56]. The most abundant natural occurring form is in tritiated water, HTO [57]. Massive production of tritium is mainly based on the interaction of fission neutrons in pressurized heavy water moderators [58].

By its radioactive nature, only tiny amounts of tritium samples are allowed in non-specialized laboratories. The extension of high resolution spectroscopic studies of hydrogen molecules including tritium-containing species provide a wider range of parameter space for testing quantum chemical theory. The largest uncertainty contributions in most recent calculation of the $X^1\Sigma_g^+$ state in molecular hydrogen and its isotopologues originates from the finite-nuclear-mass correction in leading QED correction $E^{(5)}$. The uncertainty is estimated via $E^{(5,0)}(m_e/\mu_n)$ [22, 45], to be on the order 10^{-4} cm^{-1} , and varying with isotopic species. As the tritium nucleus is about three-times heavier than hydrogen, this contribution is expected to be the smallest for the heaviest isotopologue T_2 . Studies on all isotopologues might help in disentangling the mass-dependent terms in the calculations. Besides, there is an unresolved discrepancy between the calculated and experimental value of the HD dissociation energy [59], while the homonuclear isotopologues H_2 and D_2 are in good agreement. The spectroscopic studies on the two tritium containing heteronuclear isotopologues HT and DT might help resolve this mystery by providing additional information on the g/u mixing effects.

Dieke and Tomkins performed the first emission spectra on tritium bearing isotopologues from 300 nm to 3000 nm where only transitions between excited electronic states were recorded [60, 61]. Later in the 1970's to the 1980's, spectroscopic measurements were done on the vibrational transitions in ground $X^1\Sigma_g^+$ state using Raman spectroscopy [62–64] and intracavity laser absorption [65] with uncertainty down to $5 \times 10^{-3} \text{ cm}^{-1}$. Obviously, orders of magnitudes improvement in measurement accuracy are necessary to obtain a valuable comparison with the latest calculated values.

Our group collaborates with the Karlsruhe Institute of Technology in Germany to access all three tritium-containing isotopologues gas samples for the spectroscopic studies carried out in Amsterdam. Regarding radiation safety,

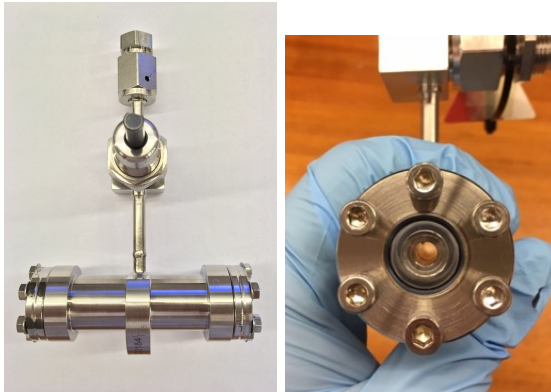


Figure 1.1: Well-sealed tritium gas cell with planar surface aperture.

tritium-containing isotopologue gas samples have to be contained in a well-sealed gas cell with proven material for the tritium contamination as shown in Fig. (1.1). The total radioactivity should be kept below 1 GBq, corresponding to 11.5 mbar cm^3 of T_2 at room temperature. Under these strict safety regulations, spectroscopic studies on these static gas samples are performed using Coherent Anti-Stokes Raman Spectroscopy (CARS) to measure the fundamental vibrational interval ($v = 0 \rightarrow 1$). Several Q-branch lines ($\Delta J = 0$) of tritium-containing species were measured at 10^{-4} cm^{-1} uncertainty, presenting an over 100-times improvement. Trivikram et al. measured the heaviest isotopologue T_2 with about $3 \times 10^{-4} \text{ cm}^{-1}$ uncertainty [66]. In this thesis, measurements on the other two tritium containing isotopologues, DT and HT, and revised measurements of T_2 will be presented.

1.3 Vibrationally excited state and quasi-bound resonance of H_2

The majority of the precision measurements on H_2 focus on the lowest vibrational levels. For example, Dickenson determined the fundamental vibrational interval ($v = 0 \rightarrow 1$) using combination differences of Doppler-free two-photon transition from $\text{X}^1\Sigma_g^+$ $v = 0$ and $v = 1$ levels to a common $\text{E}^1\Sigma_g^+$ excited state in a molecular beam with 5 MHz uncertainty [67]. The second vibrational overtone S(3) transition ($v = 0 \rightarrow 3$, $J = 1 \rightarrow 3$) was measured using Doppler-broadened cavity-ring down spectroscopy at 6 MHz uncertainty [68]. The dissociation energy in both para- and ortho-hydrogen were recently determined at sub-MHz accuracy [29, 51, 69]. The wavefunctions of these deeply

bound states, $v = 0 - 3$, have a radial probability density localized in the range of $1 - 3 a_0$. In Fig. 1.2, the potential energy curves of the adiabatic correction, the R -dependent rotational and vibrational reduced masses and the leading-order non-adiabatic correction are presented. The deeply bound levels $v = 0 - 3$ are not sensitive to the non-monotonic behaviour of the potential curve from non-adiabatic effect in the range of $2 a_0 \leq R \leq 6 a_0$. As the non-adiabatic contribution arises from the coupling of electronic and nuclear motion, higher vibrational states are expected to show stronger effects of non-adiabatic correction. The non-adiabatic correction is known to be maximized at $v = 9$ [70]. Precision measurements on these vibrationally excited states of H₂ can therefore test the calculations over a wider range of the potential energy curve of the X¹Σ_g⁺ state.

Apart from the calculated 302 bound states, there are more than 20 quasi-bound resonances. These resonance states of H₂ can be obtained from Equation (1.7) by grouping rotational and BO potential energy, corresponding to the second and third terms, together as an effective potential. For $J \neq 0$, hence the rotating H₂ molecule, this effective potential shows a local maximum, with a centrifugal barrier, possibly high enough to accommodate one or more quasi-bound resonances at high J . The resonance energies and lifetimes of these resonances were first calculated by Waech and Bernstein using the BO potential of Kolos and Wolniewicz [71]. They found 47 quasi-bound resonances and 5 more "unbound" resonances (resonances at an energy higher than the centrifugal barrier). In 2012, Selg presented a calculation of improved accuracy on the 23 quasi-bound resonances with inclusion of the non-adiabatic, relativistic and QED contributions with [72]. These levels are potentially observable with lifetimes in the range from 10^{-13} to 10^{-12} s.

However, there is a lack of experimental measurements on these high vibrational states and quasi-bound resonances for comparison with calculation. Herzberg determined level energies of the X¹Σ_g⁺ state up to the highest $v = 14$ from emission spectra of the Lyman band [73]. Dabrowski had revisited the Lyman and the Werner band and found several quasi-bound resonances with 0.1 cm⁻¹ uncertainty in emission spectra [74]. Roncin and Launay have measured the emission spectra from 78 to 170 nm and observed several quasi-bound resonances [75]. In total, 20 quasi-bound resonances from Selg's calculation have been observed.

Various methods were used to produce vibrationally excited H₂, for example using chemical reactions of H atoms with hydrogen halides [76, 77] and in hot filaments [78, 79]. These methods only produced moderately high vibrational levels with $v \leq 11$. In late 1980's, Steadman observed multiple sharp resonances in the studies of resonance-enhanced multiphoton ionization spectra (REMPI) of H₂S between 67000 and 70000 cm⁻¹, which they assigned as EF¹Σ_g⁺ - X¹Σ_g⁺ transitions with X¹Σ_g⁺ $v = 10 - 14$ [80]. Zhou and coworkers

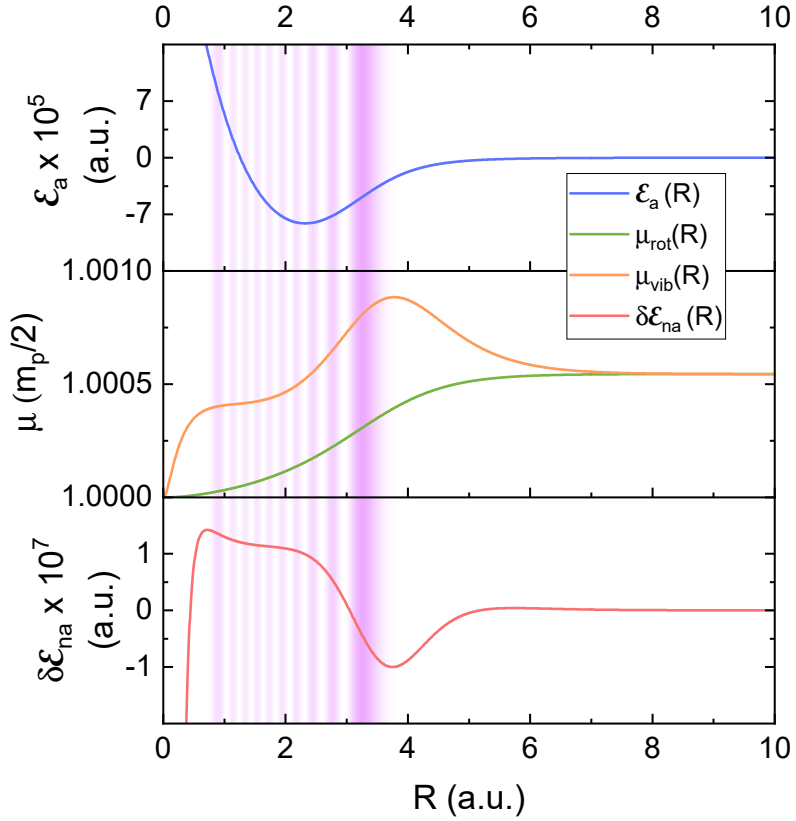


Figure 1.2: Potential energy curve of adiabatic correction (top panel), rotational and vibrational reduced mass (middle panel) and non-adiabatic correction (bottom panel). m_p is the mass of proton. The pink shaded region represents the radial probability density of the $X^1\Sigma_g^+ v = 9 J = 0$ state of H_2 .

observed comb-like features in the $S(^1D)$ translational energy spectrum from the H_2S photodissociation at 139.11 nm, where each peak in the spectrum correlates to different vibrational states of the H_2 co-fragment [81]. Later in 2021, they have observed the change in the $S(^1D)$ translational energy spectrum by selectively exciting ortho-/para- H_2S [82]. From the analysis of the translational energy spectrum, it was concluded that photolysis of H_2S to the 1B_1 electronic state can produce H_2 fragments with vibrational states up to $v = 14$ in the $X^1\Sigma_g^+$ state. From the low translational-energy part of spectrum, they also found indication that quasi-bound resonances of H_2 were produced.

Our group employed Steadman’s method to produce vibrationally excited H_2 using photodissociation of H_2S . H_2S is first excited by two-photon excitation with the UV pulsed laser set at 291.5 nm. The nascent $X^1\Sigma_g^+$ state H_2 fragment produced are then probed by a Doppler-free 2+1’ REMPI scheme. Niu et al. first measured $F^1\Sigma_g^+ (v' = 3) - X^1\Sigma_g^+ (v'' = 12)$ transitions with 0.0035 cm^{-1} uncertainty [83]. Later, Trivikram et al. improved the ionization detection stage by exciting the populated $F^1\Sigma_g^+$ state to np Rydberg levels instead of nonresonant ionization [84, 85]. F0-X11 transitions have been measured to an accuracy at 0.0015 cm^{-1} . In this thesis, measurements of vibrationally excited levels, up to the highest vibrational state $v = 14$ and some quasi-bound states of $X^1\Sigma_g^+ H_2$ will be presented. These states are prepared by photodissociation of H_2S at different wavelengths.

1.4 Outline of this thesis

In the following chapters, spectroscopic studies on two distinct topics will be discussed, (1) tritium containing isotopologues, HT, DT and T_2 , and; (2) vibrationally excited states and quasi-bound resonances of H_2 .

Chapters 2 and 3 focus on the measurement of the vibrational interval in three tritium-containing isotopologues of molecular hydrogen, HT, DT and T_2 . In Chapter 2, the precision measurement on the DT fundamental band $Q(J = 0-5)$ will be presented. The experimental measurements on tritium-containing species were compared to results of non-adiabatic perturbation theory (NAPT) produced by Polish theorists. Some details of the NAPT calculation scheme are presented Chapter 2, following our collaborative publication.

Chapter 3 reports on extended measurements of HT and a revision on T_2 with improved statistics. Detailed discussions on the uncertainty contribution are presented, including the well-known inherent artefacts of CARS measurement, the non-resonant background interferences. Further studies were explored on the observation of Lamp dips in saturated CARS spectra in Ref. [66]. In addition, hybrid pulsed-cw CARS setup was employed, which could potentially improve the accuracy in CARS measurements.

Chapters 4 - 7 cover the studies of highly vibrationally-excited and quasi-bound states of the ground electronic state of H_2 . Chapter 4 starts with the demonstration of the experimental setup by measuring transitions in the neutral sulphur atom produced as a product from H_2S photolysis. Seven two-photon transition $3p^4\ ^3P_J - 3p^34p\ ^3P_J$ are recorded with $9 \times 10^{-4}\ \text{cm}^{-1}$ uncertainty. The fine structure splittings in ground electronic configuration $3p^4$ are determined and found to be in good agreement with highly accurate laser-magnetic-resonance measurements [86]. These measurements produced an accurate anchor level which can be used for determining the excited state level energy structure of the neutral sulphur atom if infrared transitions between the excited states were to be measured.

Chapter 5 presents the production of $v = 13, 14$ states in the ground electronic $X^1\Sigma_g^+$ state of H_2 . These states are detected by two-photon excitation into the $F^1\Sigma_g^+$ outer well. For H_2 in the $v = 13$, the highest bound rotational level $J = 7$, lying only $51\ \text{cm}^{-1}$ below the dissociation limit, has been detected. Only one rotational state $J = 1$ from $v = 14$ is detected with much weaker signal strength. The assignments of the transitions are verified by recording excitation spectra from the populated F-states. The combination differences of transitions from $v = 13$ and $v = 11$ levels [84] yield the vibrational intervals in the ground electronic state H_2 . A comparison with results from NAPT calculations produces good agreement.

Chapters 6 and 7 present the studies of the quasi-bound resonances in the $X^1\Sigma_g^+$ state of H_2 produced from photolysis of H_2S . Four quasi-bound resonances of H_2 $X(v, J) = (7, 21)^*$, $(8, 19)^*$, $(9, 17)^*$ and $(10, 15)^*$, which have level energies above dissociation limit, with lifetimes longer than multiple μs are probed in our setup via two-photon excitation to $F^1\Sigma_g^+$ outer well states. A ns-lived resonance $(11, 13)^*$ is also observed with shorter delay after H_2S photolysis. The signal strengths of these transitions are much stronger than the bound-bound transitions observed in Chapter 5. It is explained by the enhanced Franck-Condon factor between the $X^1\Sigma_g^+$ and the $F^1\Sigma_g^+$ outer-well state from the extended wavefunction density towards larger internuclear separation for $X^1\Sigma_g^+$ quasi-bound resonances. Measurements of the F-X Q-branch ($\Delta J = 0$) and the S/O-branch ($\Delta J = \pm 2$) transitions connect all 5 observed quasi-bound resonances to give the $X^1\Sigma_g^+$ state level intervals.

In Chapter 7, details of the calculation of the $X^1\Sigma_g^+$ state quasi-bound resonances are presented. The well-established NAPT calculation scheme on molecular $X^1\Sigma_g^+$ state is extended to quasi-bound resonances using available potential curves in Ref. [22]. The calculated quasi-bound level intervals agree well with the observation. These quasi-bound resonances help test the $X^1\Sigma_g^+$ state potential energy curve over larger internuclear distance. The s-wave scattering length of the singlet H+H scattering is determined for the first time with inclusion of adiabatic, non-adiabatic, relativistic and QED contribution up to

$m\alpha^6$ terms.

Precision tests of nonadiabatic perturbation theory with measurements on the DT molecule

Abstract

First-principles calculations are presented for fundamental vibrational interval energies of tritium-bearing molecular hydrogen species with the improved treatment of the nonrelativistic, relativistic and quantum electrodynamic energy contributions resulting in a total uncertainty of $0.000\,11\text{ cm}^{-1}$ for DT, or about 100-times improvement over previous results. Precision coherent Raman spectroscopic measurements of DT transitions were performed at an accuracy of $< 0.000\,4\text{ cm}^{-1}$, representing even larger 250-fold improvement over previous experiments. Perfect agreement between experiment and theory is found, within 1σ , for all six transitions studied.

This chapter is reproduction of: Lai, K.-F.; Czachorowski, P.; Schlösser, M.; Puchalski, M.; Komasa, J.; Pachucki, K.; Ubachs, W.; Salumbides, E. J. Precision Tests of Nonadiabatic Perturbation Theory with Measurements on the DT Molecule. *Phys. Rev. Res.* **2019**, 1 (3), 033124

2.1 Introduction

Seventy years after its development, quantum electrodynamics (QED) has emerged to be the best-tested theory in physics. While QED is most accurately tested using a free electron system [87–89], tests in the bound atomic hydrogen system are at present limited by effects of the proton structure [90, 91]. Precision tests in the hydrogen atom rely ultimately on the narrowest transition involving the long-lived 2S quantum state with a natural lifetime of 0.12 s [92]. In contrast, the additional rotational and vibrational degrees of freedom in H₂ give rise to a multitude of states in the ground electronic manifold with extremely long lifetimes in the order of 10⁵ – 10⁶ s [93]. In addition, access to all six isotopic variants of molecular hydrogen enables a robust verification of nonadiabatic perturbation theory.

The additional complexity of the four-body molecular hydrogen system presents formidable challenges in first-principles calculations. The last decade has shown great improvements in calculation of the nonrelativistic energies using a perturbative approach [15, 17], or a recent non-perturbative treatment [42]. Concurrent developments in the calculation of relativistic [18], QED [19], and associated recoil corrections have led to sub-MHz accuracies in level energies of the stable molecular hydrogen species H₂, HD, and D₂ [52], but have not been applied to tritiated isotopologues until now.

Parallel progress in experiments have resulted in an accurate measurement of the dissociation energy of the H₂ molecule [51, 69], the measurement of its fundamental vibrational interval [67], as well as very weak quadrupole overtone transitions [32–34]. Similar spectroscopic studies have also been applied to the other stable D₂ (cf. [35, 36, 48]) and the mixed isotopologue HD (cf. [37–40]). On the other hand, very few precision studies have been undertaken on the tritium-bearing species [62, 64, 65], on account of difficulties in handling radioactive tritium. If these practical challenges would be overcome, access to tritium-bearing species T₂, HT, and DT would double the number of molecular hydrogen test systems.

Here we present highly-accurate calculations of the rovibrational transitions for all tritiated molecular hydrogen that are two orders of magnitude more accurate than previous studies [94]. This improvement is obtained by applying a recently-developed nonadiabatic perturbation theory approach to obtain accurate nonrelativistic energies [17], as well as by systematic treatment of leading, higher-order and recoil relativistic and QED corrections based on nonrelativistic wave functions. The calculations are benchmarked by accurate measurements of DT transition energies, which enables precision tests in tritiated species that are now sensitive to QED effects.

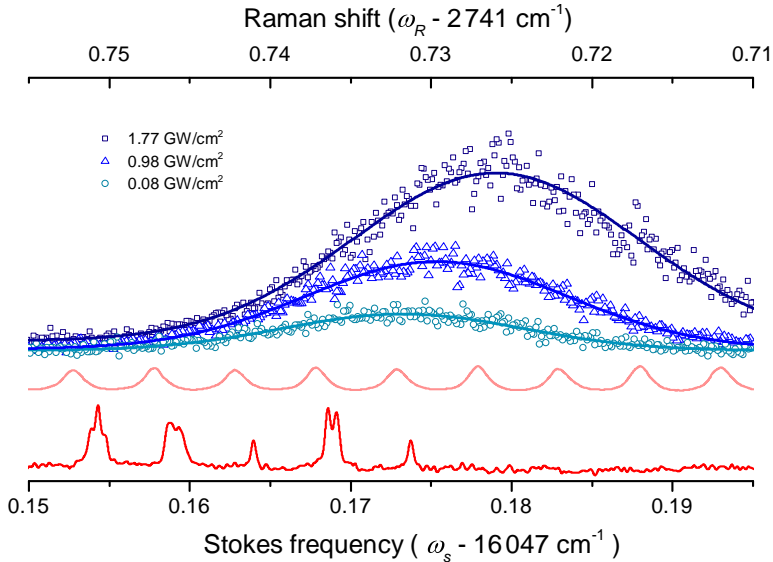


Figure 2.1: Q(1) transition of the DT $X^1\Sigma_g^+(v = 0 \rightarrow 1)$ Raman band, probed at different peak intensities and plotted with respect to the Stokes frequency ω_S (lower frequency axis) and the Raman shift ω_R (upper axis). The solid lines through the DT data points are Gaussian fits, with the line centers exhibiting ac-Stark shifts. The transmission peaks of the stabilized etalon and saturated I_2 spectrum used in the relative and absolute frequency calibrations of ω_S are also plotted. Inset: Nonlinear four-wave mixing scheme.

2.2 Experiment

As for the experimental study, we use the nonlinear frequency-mixing scheme of coherent anti-Stokes Raman spectroscopy (CARS), illustrated in the inset of Fig. 2.1. An anti-Stokes coherent beam is produced for signal detection, at frequency $\omega_{AS} = 2\omega_P - \omega_S$ corresponding to $\lambda_{AS} \sim 464$ nm, whenever the frequency difference between the pump (ω_P) and Stokes (ω_S) frequencies is in resonance with a vibrational mode (ω_R) in the molecule. The high-resolution CARS setup has been described in a previous work on T_2 [66]. An injection-seeded and frequency-doubled Nd:YAG laser provides the pump beam ($\lambda_P \sim 532$ nm), while the Stokes radiation ($\lambda_S \sim 623$ nm) originates from a narrowband pulsed dye amplifier (PDA) system [95], which is seeded by a continuous-wave (cw) ring dye laser. DT at a partial pressure of 4 mbar is contained in a 4-cm^3 gas cell, prepared from a 4:1 mixture of D_2 and T_2 at the Tritium Laboratory Karlsruhe and transported to LaserLaB Amsterdam for the spectroscopic

2. PRECISION TESTS OF NONADIABATIC PERTURBATION THEORY WITH MEASUREMENTS ON THE DT MOLECULE

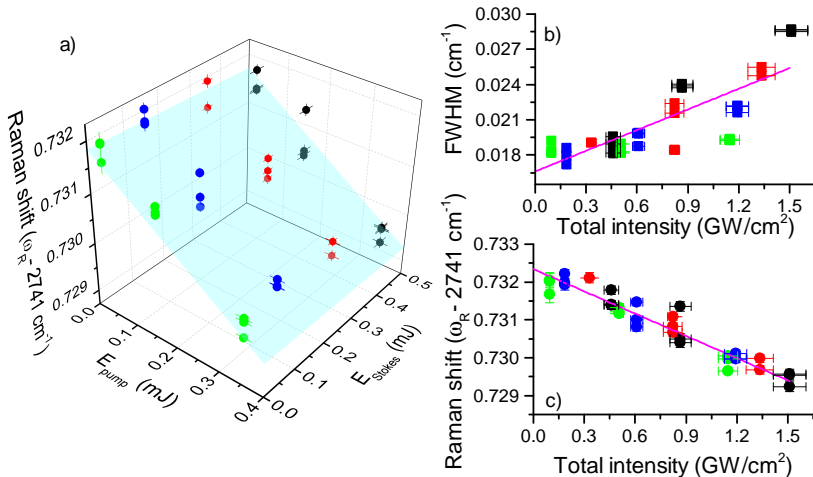


Figure 2.2: a) ac-Stark extrapolation for the Q(1) line position by fitting a plane (blue-shaded area) spanned by the pump, I_P , and Stokes, I_S , laser intensities separately. b) Full-widths at half-maximum plotted against the total intensity $I_P + I_S$. The zero-intensity ω_R value obtained in a) is consistent with a linear fit in c) using the total intensity as independent parameter.

measurements [96].

Recordings of the Q(1) Raman transition at different intensities are shown in Fig. 2.1, manifesting ac-Stark broadening and shifting. The cw-seed frequency for the ω_S radiation is calibrated using a HeNe-stabilized etalon in combination with an absolute frequency reference from saturation I_2 spectroscopy [97]. The cw-pulse frequency offset induced by frequency chirp effects in the pulsed-dye amplification [95, 98, 99] is measured and corrected for [100]. The frequency of the ω_P pulse is monitored online using a high-resolution wavemeter (High Finesse Ångström WSU-30), which is periodically calibrated against several absolute frequency standards at different operating wavelengths, including calibrations against a Cs clock with the aid of an optical frequency comb laser. This wavemeter also measures the correct frequency that includes any chirp-induced frequency offset as verified when using a narrowband titanium sapphire pulsed laser source with an adjustable cw-pulse frequency offset used in Ref. [51]. The Raman shift, $\omega_R = \omega_P - \omega_S$, is derived from the simultaneous frequency calibrations of both pump ω_P and Stokes ω_S laser frequencies.

The ac-Stark shift for the Q(1) transition is plotted in Fig. 2.2 panel a) as a function of the pump I_P and Stokes beam I_S intensities; and in panel c) as a function of the total intensity, $I_P + I_S$, of both pump and Stokes beams.

It was established that the extrapolation to the unperturbed zero-intensity frequency by fitting, a plane in a) or by a line in c), yields the same value within 2 MHz. This linear dependence is expected since the polarizabilities at λ_P and λ_S for both the $v = 0$ and $v = 1$ levels of molecular hydrogen are very similar [101]. In this manner, the ac-Stark dependence on the total intensity for all other $Q(J = 0, 2 - 5)$ transitions was treated by linear extrapolation and found to be accurate to 6 MHz. The full-widths at half-maximum are plotted in Fig. 2.2 b), which extrapolates to the Doppler width at zero intensity. Collisional shifts on the DT transitions are conservatively estimated to be ~ 1 MHz based on investigations of the stable molecular hydrogen species [102–104]. Since we cannot vary the pressure of DT, we have verified the estimates by pressure-dependent measurements of D_2 in an identical gas cell. The hyperfine structure of DT is expected to be similar to that of HD with the hyperfine splittings spanning within ~ 1 MHz, and is not observed in our Doppler-limited linewidths. Possible shifts in the hyperfine center-of-gravity of the transitions are expected to be well below a MHz and are neglected. Table 2.1 shows the uncertainty contributions, where a final uncertainty of 12 MHz or $4 \times 10^{-4} \text{ cm}^{-1}$ is estimated for the $Q(J = 0, 2 - 5)$ lines. The $Q(1)$ transition has a slightly smaller uncertainty due to more measurements collected for the assessment of systematic shifts. The reproducibility of measurements performed on multiple days is indicated in the statistics entry in Table 2.1.

Measurements of the $Q(0)$, $Q(1)$, and $Q(2)$ transitions of the fundamental band of D_2 , with 8-mbar partial pressure inside the same DT cell, were also performed. High-accuracy D_2 measurements using molecular beams have been performed with a completely different spectroscopic approach [67, 105], allowing for the *in situ* assessment of any other systematic effects. D_2 comparisons with Ref. [105] yield an average deviation, shown in Fig. 2.3, that is consistent with and validates the independently estimated uncertainty of the present CARS

Table 2.1: Systematic and statistical contributions to the frequency uncertainties in the DT fundamental vibrational Raman transitions. Values are given in MHz.

Contribution	$Q(J \neq 1)$	$Q(1)$
Pump (ω_P) calibration	6	6
Stokes (ω_S) cw calibration	2	1
Stokes cw-pulse chirp correction	5	5
ac-Stark analysis	6	3
Collisional shift	1	1
Statistics	7	5
Combined (1σ)	12	10

study. These experimental results are compared with the theoretical results presented in the following discussion.

2.3 Theory

In order to calculate molecular rovibrational levels and transition energies accurately, we use a variant of nonrelativistic quantum electrodynamics (NRQED) – an effective theory approximating QED at low energy scales [19]. It assumes an expansion of the binding energy in powers of the fine-structure constant α

$$E(\alpha) = \alpha^2 E^{(2)} + \alpha^4 E^{(4)} + \alpha^5 E^{(5)} + \alpha^6 E^{(6)} + \dots, \quad (2.1)$$

where $E^{(i)}$ is a contribution of order $\alpha^i m$ (with the electron mass m) and may include powers of $\ln \alpha$. Each $E^{(i)}$ can be expressed as an expectation value of some effective Hamiltonian with the nonrelativistic wave function. The $E^{(i)}$ terms can be calculated directly (see e.g. [21, 42, 59, 106]) or expanded further in the m/μ_n mass ratio (with $\mu_n = M_A M_B / (M_A + M_B)$ – the nuclear reduced mass) in the spirit of the nonadiabatic perturbation theory (NAPT) [17, 107]. This yields the well known components of the nonrelativistic energy – the Born-Oppenheimer (BO) energy $E^{(2,0)}$, the adiabatic correction $E^{(2,1)}$, and the nonadiabatic correction $E^{(2,2)}$ for a given rovibronic state. Similarly, NAPT enables the relativistic $E^{(4)}$ and QED $E^{(5)}$ corrections to be evaluated as a sum of the leading (infinite nuclear mass) and the recoil (finite mass) components, although finite mass QED corrections has not yet been incorporated.

The Schrödinger equation for a hydrogen molecule isotopologue, written in a center-of-mass frame, with the origin in the geometric center of the nuclei, is

$$(H + H_n - E^{(2)}) \left| \Psi(\vec{r}_1, \vec{r}_2, \vec{R}) \right\rangle = 0, \quad (2.2)$$

where

$$H = -\frac{1}{2} \left(\vec{\nabla}_1^2 + \vec{\nabla}_2^2 \right) + V, \quad (2.3)$$

$$V = -\frac{1}{r_{1A}} - \frac{1}{r_{1B}} - \frac{1}{r_{2A}} - \frac{1}{r_{2B}} + \frac{1}{r_{12}} + \frac{1}{R}, \quad (2.4)$$

$$H_n = -\frac{1}{2\mu_n} \left(\vec{\nabla}_R^2 + \vec{\nabla}_{\text{el}}^2 \right) + \left(\frac{1}{M_A} - \frac{1}{M_B} \right) \vec{\nabla}_R \vec{\nabla}_{\text{el}}, \quad (2.5)$$

and where the 1, 2 indices denote electrons, A, B denote nuclei, $\vec{R} = \vec{R}_A - \vec{R}_B$, and $\vec{\nabla}_{\text{el}} = (\vec{\nabla}_1 + \vec{\nabla}_2)/2$. The last term in H_n is present in heteronuclear isotopomers and is a source of the *gerade/ungerade* mixing effects, of relevance

to the DT species investigated here. Within NAPT, the wave function is represented as

$$\Psi(\vec{r}_1, \vec{r}_2, \vec{R}) = \psi(\vec{r}_1, \vec{r}_2) Y(\vec{n}) \chi(R) / R + \delta\Psi(\vec{r}_1, \vec{r}_2, \vec{R}), \quad (2.6)$$

where one assumes $\langle \delta\Psi | \psi \rangle_{\text{el}} = 0$ (integration over electronic coordinates only), $Y(\vec{n})$ is a spherical harmonic, and $\vec{n} = \vec{R}/R$. $\psi(\vec{r}_1, \vec{r}_2)$ is an eigenfunction of the electronic Schrödinger equation

$$H |\psi\rangle = \mathcal{E}^{(2,0)}(R) |\psi\rangle, \quad (2.7)$$

with the eigenvalue dependent on the internuclear distance R . In the NAPT leading order, the function χ satisfies the following nuclear equation

$$H_N \chi(R) = E^{(2,0)} \chi(R), \quad (2.8)$$

$$H_N = -\frac{1}{2\mu_n} \frac{d^2}{dR^2} + \mathcal{E}^{(2,0)}(R) + \frac{J(J+1)}{2\mu_n R^2}, \quad (2.9)$$

where J is the rotational quantum number. $\mathcal{E}^{(2,0)}(R)$ from the electronic Schrödinger equation (2.7) serves as a potential for the movement of the nuclei, present in the nuclear equation (2.8). We solve Eq. (2.8) with a discrete variable representation (DVR) method [22, 108] for χ , which is then used in a perturbative manner to calculate the rovibrational energy contributions $\langle \chi | \mathcal{E}^{(i,k)}(R) | \chi \rangle$, where $\mathcal{E}^{(i,k)}(R)$ denotes a correction of the order $\alpha^i m \cdot (m/\mu_n)^k$ to the electronic potential. Regarding $E^{(2)}$, its BO approximation $E^{(2,0)}$ is surely not accurate enough for our purposes. At the same time, direct calculation of $E^{(2,1)}$ and $E^{(2,2)}$ is not very convenient. This is why the nuclear Schrödinger equation is solved again instead – with the NAPT-corrected Hamiltonian, including the nonadiabatic effects up to the $(m/\mu_n)^2$ level

$$\tilde{H}_N = \left[-\frac{d}{dR} \frac{1}{2\mu_{\parallel}(R)} \frac{d}{dR} + \frac{J(J+1)}{2\mu_{\perp}(R)R^2} + \frac{\mathcal{W}'_{\parallel}(R)}{R} + \mathcal{Y}(R) \right]. \quad (2.10)$$

All the functions $\mu_{\parallel}(R)$, $\mu_{\perp}(R)$, $\mathcal{W}'_{\parallel}(R)$, and $\mathcal{Y}(R)$ in the above are defined and provided as analytic fits in Refs. [17, 22, 107]. Note that $\mathcal{Y}(R)$ incorporates both the adiabatic and nonadiabatic effects, and the g/u -mixing term from Eq. (2.5) in particular.

The $E^{(4)}$ and $E^{(6)}$ corrections are calculated as

$$E^{(4)} = E^{(4,0)} + E^{(4,1)}, \quad (2.11)$$

$$E^{(6)} = \langle \chi | \mathcal{E}^{(6,0)}(R) | \chi \rangle \quad (2.12)$$

$$+ \langle \chi | \mathcal{E}^{(4,0)}(R) \frac{1}{(E^{(2,0)} - H_N)'} \mathcal{E}^{(4,0)}(R) | \chi \rangle,$$

2. PRECISION TESTS OF NONADIABATIC PERTURBATION THEORY WITH MEASUREMENTS ON THE DT MOLECULE

where

$$E^{(4,0)} = \langle \chi | \mathcal{E}^{(4,0)}(R) | \chi \rangle, \quad (2.13)$$

$$E^{(4,1)} = \langle \chi | \mathcal{E}^{(4,1)}(R) | \chi \rangle \quad (2.14)$$

$$+ 2 \langle \chi | \mathcal{E}^{(4,0)}(R) \frac{1}{(E^{(2,0)} - H_N)'} \mathcal{E}^{(2,1)}(R) | \chi \rangle.$$

The rest: $E^{(5)}$, $E^{(7)}$, and E_{FS} (the correction due to the finite nuclear sizes), are calculated just as expectation values with $\chi(R)$. All the needed potentials are taken from, respectively: $\mathcal{E}^{(2,0)}(R)$ – Refs. [15, 22], $\mathcal{E}^{(2,1)}(R)$ – Ref. [16], the nonadiabatic potentials – Refs. [17, 107], $\mathcal{E}^{(4,0)}(R)$ – Ref. [18], $\mathcal{E}^{(4,1)}(R)$ – Ref. [52], $\mathcal{E}^{(6,0)}(R)$ – Ref. [19]. The potentials $\mathcal{E}^{(7,0)}(R)$ and $\mathcal{E}_{\text{FS}}(R)$ make use of the electron-nucleus Dirac δ values obtained in Ref. [18]. Their calculation method follows the approach of Refs. [52, 59] respectively (based, in turn, on Ref. [109]). The leading QED contribution $\mathcal{E}^{(5,0)}(R)$ combines results from Refs. [18, 19, 46]. More details concerning particular potentials are available in Ref. [22]. The theoretical uncertainty of an $E^{(i)}$ component includes the missing next term $E^{(i, k_{\text{max}}+1)} \approx E^{(i, k_{\text{max}})} m/\mu_{\text{n}}$, where k_{max} is the highest included term in the m/μ_{n} expansion. For $E^{(2)}$, $E^{(i, k_{\text{max}})}$ is $E^{(2,2)} \approx E^{(2)} - \langle \chi | \mathcal{E}^{(2,1)}(R) | \chi \rangle - E^{(2,0)}$, for $E^{(4)}$ it is $E^{(4,1)}$, and $E^{(i, k_{\text{max}})} = E^{(i,0)} = E^{(i)}$ for $i = 5$ and 6 , as well as for E_{FS} . The uncertainties also include an estimate of the numerical error of the respective potential used, and the E_{FS} error comprises a contribution from uncertainties of the nuclear radii. For $E^{(7)}$, for which only an approximate formula is known, a relative 25% error is used [59] instead. Total theoretical uncertainties of all the transitions reported in this paper are dominated by the missing $E^{(2,3)}$ in the nonrelativistic contribution. The calculated contributions to the Q(1) transition energy in the fundamental vibrational interval ($v = 0 \rightarrow 1$) for all tritiated species DT, HT, and T₂ are listed in Table 2.2. The theoretical results obtained here are in agreement with Ref. [94], with the present accuracy of 0.00011 cm^{-1} representing more than a 100-fold improvement. The 0.02 cm^{-1} uncertainty in Ref. [94] is dominated by the uncertainty in the nonadiabatic nonrelativistic correction ($E^{(2,2)}$), and only included leading order relativistic ($E^{(4,0)}$) and QED corrections using a Bethe logarithm that is 20% off from the modern value, or a deviation of $> 0.001 \text{ cm}^{-1}$ in $E^{(5)}$.

Table 2.2: Calculated contributions to the $Q(1)$ transition energy (in units of cm^{-1}) in the fundamental band of tritium-bearing molecular hydrogen. E_{FS} is the finite nuclear size correction with $r_p = 0.8414(19)$ fm [110], $r_d = 2.12799(74)$ fm [110], and $r_t = 1.7591(363)$ fm [111], for the proton-, deuteron-, and triton sizes, respectively. The fine-structure constant α , Rydberg constant R_∞ , and Bohr radius a_0 are taken from [110], as are the respective proton-, deuteron- and triton-electron mass ratios: $m_p/m = 1836.15267343(11)$, $m_d/m = 3670.48296788(13)$, $m_t/m = 5496.92153573(27)$.

Contribution	T_2	DT	HT
$E^{(2)}$	2463.346322(61)	2741.72999(11)	3431.57340(44)
$E^{(4)}$	0.0148375(1)	0.0163396(1)	0.0198906(1)
$E^{(4,0)}$	0.01480683	0.01629689	0.01980422
$E^{(4,1)}$	0.00003062	0.00004272	0.00008636
$E^{(5)}$	-0.0126866(79)	-0.0141052(96)	-0.0176069(156)
$E^{(6)}$	-0.0001135(3)	-0.0001262(4)	-0.0001578(5)
$E^{(7)}$	0.0000061(15)	0.0000068(17)	0.0000085(21)
E_{FS}	-0.0000082(3)	-0.0000113(2)	-0.0000070(2)
Total	2463.348358(62)	2741.73209(11)	3431.57553(44)

2.4 Discussion and Summary

The experimental and theoretical values for $Q(J = 0 - 5)$ transition energies in DT are listed in Table 2.3. The present measurements with 0.0004 cm^{-1} accuracy are consistent with, but are two orders of magnitude more precise than the previous investigation in Ref. [64]. The comparison of the present experimental and theoretical values demonstrates excellent agreement as listed in Table 2.3 and shown graphically in Fig. 2.3, with the differences falling well within 1σ of the combined measurement and calculation uncertainty.

In summary, we have determined $Q(J = 0 - 5)$ transition energies of the fundamental band of DT with a 250-fold improvement over all other previous measurements. Highly-accurate calculations are also presented with similar improvements of uncertainty. Studies using the heavier tritiated species are useful in disentangling various mass-dependent effects that have been frequently overlooked in the literature [112]. In view of a present 2.7σ discrepancy in experiment and calculations in the dissociation energy of HD [106] while there is perfect agreement for H_2 and D_2 , investigations on heteronuclear species such as DT may be helpful in the resolution of the HD discrepancy.

Since the present experimental and theoretical values are in very good agreement, these can be used to constrain hypothetical long-range fifth forces between hadrons [113]. In fifth-force investigations on diatomic molecules, the hypothetical interaction is parameterized as a Yukawa potential

$$V_5(R; \alpha_5, \lambda_5) = N_1 N_2 \frac{\alpha_5 \exp\{-R/\lambda_5\}}{R}, \quad (2.15)$$

where α_5 and λ_5 are the interaction strength and length parameters, respectively, while R is the distance between the two nuclei of nuclear number N_1

Table 2.3: Fundamental vibrational ($v = 0 \rightarrow 1$) intervals of the $Q(J)$ transitions in DT. The measured values appear in the second column while the theoretical values are listed in the third column, with uncertainties indicated within parentheses. The last column is the difference ($\omega_{\text{exp}} - \omega_{\text{calc}}$) with the combined experiment-calculation uncertainty indicated. All values in units of cm^{-1} .

line	experiment	calculation	difference
Q(0)	2743.341 71 (40)	2743.341 74 (11)	-0.000 03 (41)
Q(1)	2741.732 04 (33)	2741.732 09 (11)	-0.000 05 (35)
Q(2)	2738.516 59 (40)	2738.516 97 (11)	-0.000 38 (41)
Q(3)	2733.704 70 (40)	2733.704 66 (11)	+0.000 04 (41)
Q(4)	2727.307 34 (40)	2727.307 55 (11)	-0.000 21 (41)
Q(5)	2719.341 93 (40)	2719.342 02 (11)	-0.000 09 (41)

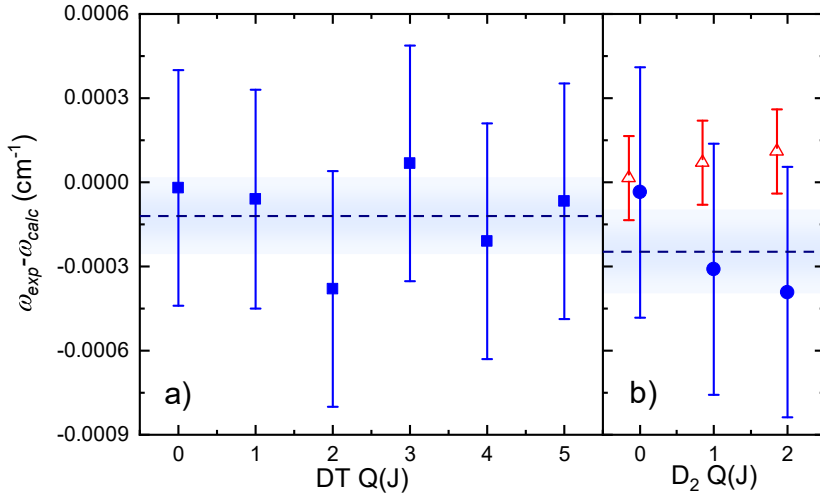


Figure 2.3: a) Comparison of the experimental and calculated DT Raman intervals (squares) demonstrating very good agreement. b) A comparison of D₂ Q(J) lines (circles) also measured with the present CARS setup and DT gas cell are also shown. A comparison of D₂ molecular beam measurements in Ref. [105] (triangles) is also plotted in b). The dashed lines indicate the average in the experiment-calculation differences, $\omega_{\text{exp}} - \omega_{\text{calc}}$, while the shaded regions indicate the standard deviation.

and N_2 . The most stringent constraint for these hypothetical fifth forces in the range $\lambda_5 = 1 \text{ \AA}$ is derived from HD⁺ [114] of $\alpha_5 < 1 \times 10^{-9}\alpha$, where α is the electromagnetic coupling strength. This tight bound is largely due to the sub-MHz uncertainties obtained in the HD⁺ measurements. Applying the method in Ref. [113] on the DT Q(1) transition, the strength of a fifth force for an interaction range of $\sim 1 \text{ \AA}$ is constrained at $\alpha_5 < 2.1 \times 10^{-8}\alpha$, which is more than an order of magnitude weaker than the HD⁺ derived bound. Averaging over the six DT transitions results in a slightly tighter of constraint $\alpha_5 < 8.4 \times 10^{-9}\alpha$, which is still about an order-of-magnitude weaker than the HD⁺ derived bound. With the sixfold enhanced sensitivity of DT with respect to the lightest species H₂ as seen from Eq. 2.15, the present DT results yield a limit that is slightly more stringent than that of H₂. This is despite the H₂ ($v = 0 \rightarrow 1$) Q lines [67, 105] having 2.7 times better accuracy than the present DT study. With the inherent sensitivity of the heavier tritiated species (with $N_t = 3$) this limit can be further tightened when an accuracy in the kHz level

is reached, for example by using techniques recently applied to HD [39].

Acknowledgments

We are grateful to Tobias Falke, David Hillesheimer, Stefan Welte and Jürgen Wendel of TLK for the preparation and handling of the tritium cell. WU thanks the European Research Council for an ERC-Advanced grant (No 670168). The calculations were supported by the National Science Center (Poland) Grants No. 2017/27/B/ST2/02459 (KP) and 2016/23/B/ST4/01821 (MP) and by PL-Grid Infrastructure. The research leading to these results has received funding from LASERLAB-EUROPE (grant agreement no. 654148, European Union's Horizon 2020 research and innovation programme).

Precision measurement of the fundamental vibrational frequencies of T₂, DT, HT

Abstract

High-resolution coherent Raman spectroscopic measurements of all three tritium-containing molecular hydrogen isotopologues T₂, DT and HT were performed to determine the ground electronic state fundamental Q-branch ($v = 0 \rightarrow 1, \Delta J = 0$) transition frequencies at accuracies of 0.0005 cm^{-1} . An over hundred-fold improvement in accuracy over previous experiments allows the comparison with the latest ab initio calculations in the framework of Non-Adiabatic Perturbation Theory including nonrelativistic, relativistic and QED contributions. Excellent agreement is found between experiment and theory, thus providing a verification of the validity of the NAPT-framework for these tritiated species. While the transition frequencies were corrected for ac-Stark shifts, the contributions of non-resonant background as well as quantum interference effects between resonant features in the nonlinear spectroscopy were quantitatively investigated, also leading to corrections to the transition frequencies. Methods of saturated CARS with the observation of Lamb dips, as well as the use of continuous-wave radiation for the Stokes frequency were explored, that might pave the way for future higher-accuracy CARS measurements.

This chapter is reproduction of: Lai, K.-F.; Hermann, V.; Trivikram, T. M.; Diouf, M.; Schlösser, M.; Ubachs, W.; Salumbides, E. J. Precision Measurement of the Fundamental Vibrational Frequencies of Tritium-Bearing Hydrogen Molecules: T₂, DT, HT. *Phys. Chem. Chem. Phys.* **2020**, 22 (16), 8973–8987

3.1 Introduction

Molecular hydrogen represents a benchmark molecule for testing quantum chemical theories. The comparison between precision spectroscopic measurements on the level structure of hydrogen and the results from calculations has made H₂ and its isotopologues a test bed for searches of fifth forces [113], higher dimensions [115], and physics beyond the Standard Model of physics [116]. On the experimental side the measurement of the dissociation energy of H₂ has witnessed great improvements in the past decade [28, 29, 51, 69] now reaching a relative accuracy of 3×10^{-10} . Each isotopologue supports over 300 bound and long-lived rovibrational levels, that provide an extended playing field for performing fundamental tests, such as the ground tone vibrational interval [67], the quadrupole overtone transitions of H₂ [32–34] and in the D₂ species [35, 36], as well as in the mixed isotopologue HD [37–40].

On the theoretical side level energy calculations of the molecular hydrogen four-body system have undergone equally great improvements, producing highly accurate level energies of H₂ and D₂ [117] as well as for HD [107]. These methods were based on calculations of Born-Oppenheimer energies [15], and separate approaches for adiabatic [16] and non-adiabatic [17] corrections, as well as computations of relativistic [18] and quantum electrodynamic effects [19]. This development has led to the comprehensive approach of non-adiabatic perturbation theory (NAPT) [22, 52], which now enables the rapid computation of all bound rovibrational states in the ground electronic manifold of the hydrogen isotopologues. In addition, and alongside, an even more refined and more accurate method involving direct 4-body calculations is being pursued, but this is currently limited to the computation of the binding energy of the lowest rovibrational level [42, 59].

Most of the experimental precision spectroscopic studies were performed in the typical environment of molecular beams that can be easily applied to the stable, non-radioactive, hydrogen isotopologues H₂, HD and D₂. Tritium-containing isotopologues, HT, DT and T₂ have been much less frequently studied, because of limited access and handling difficulties due to safety requirements holding for radioactive species. The first spectroscopic studies on tritium bearing hydrogen molecules were performed by Dieke and Tomkins at Argonne National Laboratories recording emission spectra [60, 61]. Later, other methods were applied, such as spontaneous Raman spectroscopy [62–64] and intracavity laser absorption, combined with an optophone [65]. A rationale for exploring tritium spectroscopy is that the heavier, tritiated molecular hydrogen species exhibit smaller non-adiabatic contributions to the level energies. High precision studies on these species may help to disentangle the effect of mass-dependent terms in the calculation of hydrogen level energies. Also, inclusion of tritium provides two additional heteronuclear species, HT and DT.

These species provide information on the g/u mixing effects present in heteronuclear species. Such studies might help resolve the discrepancy observed in HD, between the experimental value for the dissociation energy [49] and the theoretical value [59].

The precise level structure of the tritium bearing hydrogen molecules is of relevance for the Karlsruhe Tritium Neutrino experiment (KATRIN) focusing on the β decay from T_2 [118]. The β -electron spectrum depends on the final state distribution of the ${}^3\text{HeT}^+$ daughter molecules [119], requiring accurate level energies of ${}^3\text{HeT}^+$, but also on the isotopologue distribution, parent quantum state distribution, and the level structure of the parent states [120–122]. The Raman spectroscopic techniques for molecular hydrogen isotopologues, including tritium-bearing species, were further developed to determine composition and concentration of the isotope mixtures for the KATRIN experiment [123–125].

Here we present a study of transition frequencies in the fundamental vibrational band of all tritiated species, T_2 , DT and HT, via Coherent Anti-Stokes Raman Scattering (CARS). After preliminary reports on the CARS detection [126], on the spectroscopy of the T_2 isotopologue [66] and DT [127], we now present a comprehensive report, including results on HT and further detailing the experimental methods. It is noted that remeasurements were performed for the T_2 species yielding improved statistics, following up on a previous set of data [66]. A comparison is made with the findings of theoretical calculations in the NAP-T-framework [22].

3.2 Experiment

For designing an experiment on tritium-bearing hydrogen isotopologues aspects of obtainable experimental precision have to be matched to safety regulations with regard to radioactivity. The requirement of a legal upper limit of 1 GBq of tritium stored in the laboratory, corresponding in case of T_2 to a gas amount of $11.5 \text{ mbar}\cdot\text{cm}^3$ at room temperature, and the prohibition of pumping gas into an exhaust, sets constraints on the experimental method. Whereas in many previous precision studies on molecular hydrogen multi-step laser excitation was combined with ion detection [28, 50, 51, 69] this is not possible in case of tritium, in view of the $\sim 10^9$ fast electrons and ions being produced per second from the radioactive sample. In view of containment requirements molecular beam studies are ruled out as well.

A closed-cell environment with a fill of static gas is chosen as a safe solution. Spectroscopic detection via coherent Raman processes is more sensitive than direct linear infra-red absorption, while in both cases Doppler broadening scales linearly with the vibrational energy, so imposing the same level of fre-

3. PRECISION MEASUREMENT OF THE FUNDAMENTAL VIBRATIONAL FREQUENCIES OF T₂, DT, HT

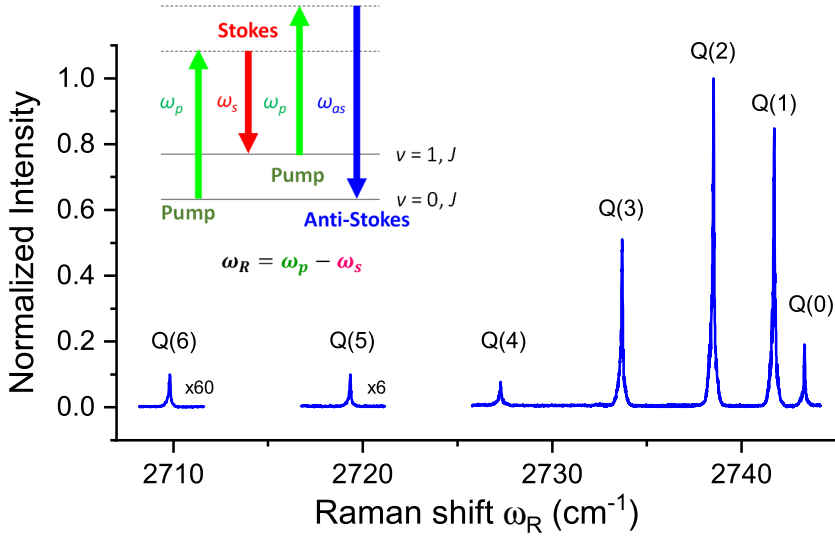


Figure 3.1: Overview recording of the $X \Sigma_g^+$ ($v = 0 \rightarrow 1$) Q(0–6) lines in DT using a combination of an injection-seeded Nd:YAG laser and a grating-based pulsed-dye laser. The inset shows an energy diagram for the CARS four-wave mixing scheme.

quency uncertainty. These arguments led us to the choice of performing CARS experiments for the tritium-bearing hydrogen molecules. In this section the handling of the tritium gas cell, the optical layout of the CARS setup, and the frequency calibration are detailed, while systematic effects are discussed.

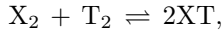
3.2.1 Tritium gas samples

The sample cell for the present CARS measurements is specially built from well-proven materials for tritium gas containment, and has been described previously [126]. The cell with an inner volume of 4 cm^3 has input and output windows placed at a distance of 8 cm, so that focusing at $f = 20 \text{ cm}$ is possible without burning window surfaces and avoiding a too high intensity in the focus, in view of issues related to the ac-Stark effect (see below).

First, a high purity T₂ gas sample was prepared in the Tritium Laboratory Karlsruhe (TLK). The cell filled was filled to 2.5 mbar to be below the legal activity limit including a safety margin.

The heteronuclear molecules HT or DT can be generated by catalytic self-exchange reactions driven by ions [128] produced in the constant β -radiation

intensity from tritium decay.



with X being H or D. The estimated HT and DT partial pressures are derived from equilibrium constants K_{eq} :

$$K_{\text{eq}} = \frac{[\text{XT}]^2}{[\text{X}_2][\text{T}_2]},$$

Values for K_{eq} are determined [129] at 2.58 for HT and 3.82 for DT at 300 K.

For the preparation of DT, first D_2 and T_2 were injected at a 4:1 ratio into a large mixing vessel. After a short time DT is formed via radio-chemical equilibration. A sample was extracted and filled into the CARS cell up to a total pressure of 12.7 mbar. The partial pressure of DT is estimated to be about 3.8 mbar. At the time of the preparation of the HT cell, this accurate mixing procedure was not available due to constraints with other running experiments. Thus, HT preparation needed to be performed inside the CARS-cell. The 2.5 mbar T_2 sample was topped up with H_2 up to a total pressure of 11.5 mbar. This would lead to a theoretical partial pressure of 3.6 mbar. It should be noted that this procedure is less accurately controllable as tritium gas might have been partially back-diffused from the cell reducing the actual HT yield.

In view of the tritium radioactive half-life of 12.3 years these (partial) pressures effectively remained constant during the measurements performed in time windows of months. The safety-controlled and tritium-gas filled cell was transported to LaserLaB Amsterdam, where the CARS measurements were carried out.

3.2.2 Precision CARS setup

In the present study, the fundamental band ($\nu = 1 \leftarrow 0$) Q-branch transitions of all three tritiated species are measured by the CARS non-linear optical technique. The specific resonant four-wave mixing scheme of the CARS process is shown in Fig. 3.1 alongside with an overview spectrum of the Q-lines in DT. An anti-Stokes field is generated, at frequency $\omega_{\text{AS}} = 2\omega_{\text{P}} - \omega_{\text{S}}$, using input fields of a pump frequency ω_{P} and a Stokes frequency ω_{S} . The integrated anti-Stokes signal intensity I_{AS} is produced as a coherent light beam in the forward direction under phase-matching conditions and is proportional to [130]:

$$I_{\text{AS}} \propto \int \int |\chi^{(3)}|^2 I_{\text{P}}^2(z, t) I_{\text{S}}(z, t) dz dt, \quad (3.1)$$

where $I_{\text{P}}(z, t)$ and $I_{\text{S}}(z, t)$ are the spatial and temporal evolution of pump and Stokes intensity and z is the optical path. The third order nonlinear

3. PRECISION MEASUREMENT OF THE FUNDAMENTAL VIBRATIONAL FREQUENCIES OF T₂, DT, HT

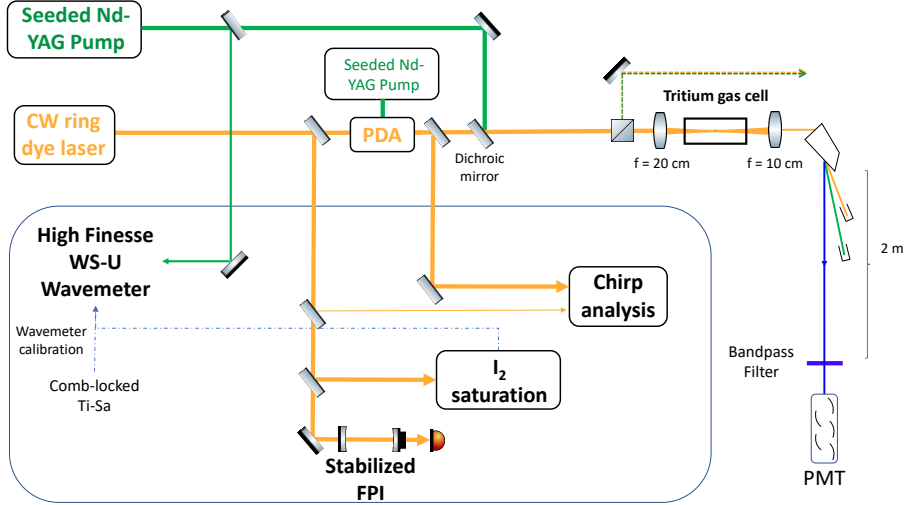


Figure 3.2: Optical layout for the CARS spectroscopy setup. The frame encloses the setups for frequency calibration of the pump and Stokes beams. See text for more details.

susceptibility $\chi^{(3)}$ depends on the molecular number density and the differential Raman cross-section [130].

The optical layout of the CARS setup is shown in Fig. 3.2. The pump beam is obtained from a frequency-doubled injection-seeded Nd-YAG laser (Spectra-Physics GCR-330) delivering pulses at 532 nm, of 8 ns duration, which would correspond to a bandwidth of about 55 MHz in case of Fourier transform (FT) limited laser pulses. During the measurements, only low pulse energies were used, ranging from 30 to 500 μJ in the interaction range.

For the precision CARS measurements the Stokes beam is obtained from an injection-seeded traveling-wave pulsed dye amplifier (PDA) operating on 4-(dicyanomethylene)-2-methyl-6-(4-dimethylaminostyryl)-4*H*-pyran (DCM) dye in methanol [95]. The continuous-wave (cw) seed light for the PDA is obtained through an optical fiber from a ring-dye laser, covering the range from 590 nm to 650 nm. With 150 mW seed power and 50 mJ pumping from a second frequency-doubled injection-seeded Nd-YAG laser (Spectra-Physics Pro-250), the output energy reaches about 5 mJ at 633 nm (peak performance wavelength) at 6 ns pulse duration, which would correspond to a bandwidth of about a 74 MHz in case of FT-limited laser pulses; the actual width will be slightly larger in view of the chirp phenomena detected (see below). The pulse energy of the Stokes beam in the CARS experiment was kept unchanged for

most part of the measurement campaigns at $< 20 \mu\text{J}$.

The pump and Stokes beams are combined on a longpass dichroic mirror and passed through a polarization beam splitter cube to ensure parallel polarizations. The two pulses are focused co-linearly into a gas cell with a $f = 20$ cm lens. The flat-top pump pulse beam waist is about $44 \mu\text{m}$, as measured by a CCD camera, for a 3 mm Rayleigh length. The Stokes pulse is estimated to be 1.7 times larger in diameter than the pump beam. Part of the merged beams is sampled out over a long distance for alignment purposes, with the angle mismatch estimated to be better than 2 mrad. The generated CARS signal (at $\lambda \sim 450 - 470$ nm) travels along the same propagation axis of the pump and Stokes beams. The CARS-signal beam is collimated with a $f = 10$ cm lens, dispersed from the incident beams by a Pellin-Broca prism, and propagated over a 2 m separation path. The signal beam is then passed through an aperture and bandpass filter, and detected by photomultiplier tube (Philips XP-1911) mounted inside a dark box.

The measurements are performed with few-mbar pressure gas samples, and the spectra obtained are expected to be Doppler-limited. The expression for Doppler broadening (FWHM) of forward spontaneous Raman scattering is [131]:

$$\Delta\nu = \frac{2\nu_0}{c} \left(\frac{2k_B T \ln 2}{m} \right)^{1/2} \quad (3.2)$$

where ν_0 is the fundamental vibrational frequency interval, m is the molecular mass, k_B the Boltzmann constant, c the speed of light, and T the temperature. This results in a Doppler width at room temperature of 370 MHz for the heaviest species T_2 , and about 450 MHz and 630 MHz for DT and HT, respectively. CARS spectral profile simulations by Lucht and Farrow [131] showed that the spectral width of the CARS resonances is about 1.2-times that of the spontaneous Raman scattering in the forward direction. These values for the width are to be further increased by contributions of the laser bandwidth of both lasers, some additional broadening caused by the timing jitter in the temporal overlap of the two pulses (within 3.5 ns), and by ac-Stark broadening.

3.2.3 Frequency calibration

The frequency calibration of the Stokes beam was performed in two stages. As shown in Fig. 3.2, part of the cw seed-radiation was split off to perform I_2 -saturation spectroscopy for absolute calibration against well-calibrated I_2 -standards [97], and another part for measuring transmission markers from an etalon (FSR = 150.67(2) MHz) stabilized by a HeNe laser (Thorlabs HRS-015). The resulting uncertainty in the absolute frequency calibration of the cw seed laser amounts to 2 MHz.

3. PRECISION MEASUREMENT OF THE FUNDAMENTAL VIBRATIONAL FREQUENCIES OF T_2 , DT, HT

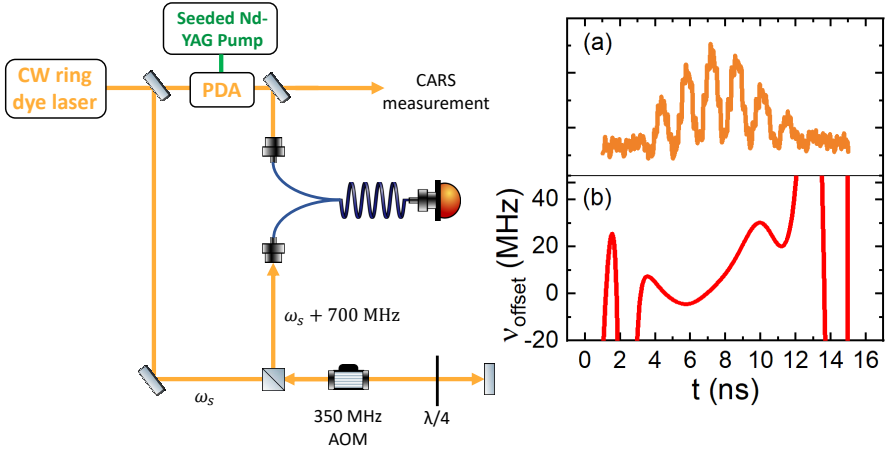


Figure 3.3: Setup for the frequency chirp measurement of the output of the PDA laser system. The cw-seed laser is shifted by double-passing an AOM at 350 MHz modulation frequency. The shifted cw and pulsed laser outputs are coupled through a single mode 2 x 2 fused fibre coupler for imposing spatial overlap. The beat note in (a) is detected on a fast photo-detector (Thorlabs DET025AFC) and stored in a Tektronix TDS7404 oscilloscope. b) The instantaneous frequency offset, $\nu_{\text{offset}} = \nu_{\text{pulse}} - \nu_{\text{cw}}$, is obtained from the phase evolution of the 700 MHz carrier signal [132].

In a second step the chirp-induced pulse-cw frequency offset was measured by techniques previously employed for frequency calibration of a PDA-system [95, 98, 99]. The frequency of the cw-seed was shifted by +700 MHz by an acousto-optic modulator (AOM) in a double-pass configuration and the beatnote between the shifted cw-seeding and Stokes pulses was recorded using a fast photodetector and a 4-GHz bandwidth oscilloscope. The setup for producing a beat-note signal is displayed in Fig. 3.3a. Following Hannemann et al. [132] for the frequency chirp analysis, the time-dependent phase in the duration of the pulse is extracted from the beat-note signal, to yield a time-dependent frequency offset curve as plotted in Fig. 3.3b. The reported average frequency offset values are obtained by time-integrating the frequency offset over the pulse duration, weighted by the instantaneous intensity.

A systematic study of frequency deviations between the cw-seed frequency and the PDA frequency was performed for various settings of the PDA. Typical results for measured frequency offsets in the PDA, running on DCM in methanol, are displayed in Fig. 3.4. The chirp-offset is found to vary from

23 MHz at 610 nm (Stokes wavelength for T₂) to 5 MHz at 650 nm (Stokes wavelength for HT) as shown in Fig. 3.4a, while also a dependence on the intensity was observed as shown in Fig. 3.4b. In addition, the effect of frequency chirp over the spatial beam profile of the Stokes beam was measured, and was observed to vary within 2 MHz. During the CARS measurements the chirp analysis was performed after co-propagating the output of the pulsed laser with that of the AOM-shifted cw-laser output in a single mode fiber, so that this spatial effect was averaged out. Systematic chirp-analysis measurements were performed for the laser settings during every measurement day. The frequency calibration of the PDA-laser was corrected for the chirp results during the CARS precision measurements, for which an estimated uncertainty of 5 MHz represents the standard deviation over different measurement days, as shown in Fig. 3.4c.

The frequency of the 532 nm pump pulse, obtained from the injection-seeded Nd:YAG laser, was directly measured by a High Finesse WSU-30 (Toptica) wavemeter. The absolute calibration of the wavemeter was verified during each measurement run by measurements of I₂-hyperfine transitions in the range 600 to 650 nm, as well as measurement of a cw Ti:Sa laser at 718 nm locked to a frequency comb laser [51]. These measurements result in a value for the typical drift of the wavemeter, determined at 0.3 MHz/hr. In addition the effect of measuring cw laser vs. pulsed laser radiation was verified by measuring the frequency of the output of the cw ring laser seed frequency vs. the output of the PDA. As a result of these repeated procedures the uncertainty of the frequency of the pump pulse is estimated at 6 MHz. In a recent study a similar model wavemeter (WSU-2) was used in measurements of several ⁴⁰Ca⁺ ion transitions and the calibrations methods led to an absolute accuracy of 5 MHz [133].

3.2.4 ac-Stark shift

The ac-Stark effects occurring in CARS measurements of the hydrogen molecule have been investigated in detail [101, 134, 135]. In our current setup, the ac-Stark shift is caused by both Stokes and pump pulses and can be approximated in terms of pulse energies E_P, E_S , areas at the beam waist A_P, A_S and pulse durations (FWHM) τ_P, τ_S , and the ac-Stark shift can be expressed as:

$$\delta\nu = \kappa_P \frac{E_P}{A_P \tau_P} + \kappa_S \frac{E_S}{A_S \tau_S}.$$

The constant κ , for both P and S depends on the difference of the ac-Stark shift in upper and lower states via [135]:

$$\kappa = -\frac{2\pi}{hc} \left((\alpha_{v'} - \alpha_{v''}) + \frac{2}{3} \frac{J(J+1) - 3m_J^2}{(2J+3)(2J-1)} (\gamma_{v'} - \gamma_{v''}) \right) \quad (3.3)$$

3. PRECISION MEASUREMENT OF THE FUNDAMENTAL VIBRATIONAL FREQUENCIES OF T₂, DT, HT

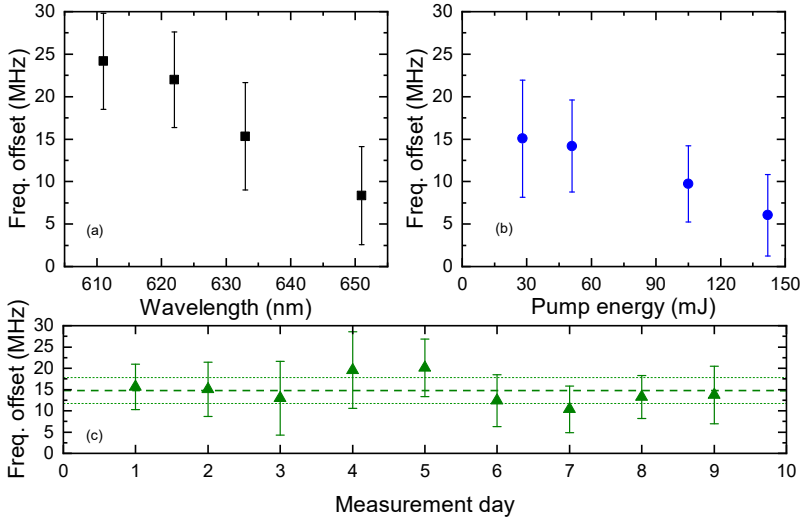


Figure 3.4: Result of frequency chirp measurements of the PDA laser system. a) Pulse-cw frequency offset Stokes beam from PDA (DCM in Methanol) at different wavelengths with 50 mJ pump energy. b) Frequency offset of the PDA at 633 nm for different pump energies. c) Daily variation of frequency offset of the PDA at 633 nm.

where $\alpha_{v'}$ and $\gamma_{v'}$ are the dynamic (frequency-dependent) isotropic polarizabilities and anisotropic polarizabilities at frequencies v' and v'' , respectively. The zero field transition frequency can be obtained by performing measurements at different Stokes and pump energies and extrapolation to zero. Since the frequencies used in CARS are far from the dipole-allowed transitions in molecular hydrogen, the polarizability term only weakly depends on the frequency in the optical range [101] and the expression can be approximated as (with $\kappa_P = \kappa_S = \kappa$):

$$\delta\nu = \kappa \left(\frac{E_P}{A_P \tau_P} + \frac{E_S}{A_S \tau_S} \right).$$

As the effective area and pulse width of the pump and Stokes beams are affected by spatial and temporal overlap between the two pulses, the value and the reproducibility of the shift coefficient in terms of pulse energy for pump and Stokes were measured extensively on the DT Q(1) transition [127], yielding $\frac{\kappa_P}{A_P \tau_P} = -0.0064(7) \text{ cm}^{-1} \text{ mJ}^{-1}$ and $\frac{\kappa_S}{A_S \tau_S} = -0.0006(2) \text{ cm}^{-1} \text{ mJ}^{-1}$. To find a balance between minimal ac-Stark shift and sufficient signal strength, the Stokes pulse energy was kept below 10 μJ for the T₂ and DT measurements. In such conditions, the uncertainty of the ac-Stark shift from the Stokes beam,

upon extrapolation to zero intensity, is estimated to be less than 1 MHz. Due to the weaker signal strengths obtained in the HT experiments, the Stokes energy was raised to 20 μJ , while the pump energy was varied from 90 to 500 μJ . Here the the pump energy was not increased further in view of saturation and asymmetry phenomena observed in the spectra, as discussed below.

3.2.5 Pressure shift

Collisional shift coefficients of Raman transitions in stable molecular hydrogen isotopologues are well studied in the large pressure range from tens of millibars to a few bars of total pressure [102–104]. For the reported shift coefficients the presently measured CARS lines are estimated to undergo shifts below ~ 1 MHz. In addition, the collisional shift of D_2 was investigated in the present study by pressure-dependent CARS measurements of pure D_2 in an identical gas cell. The shift coefficient is found to equal 0.06 MHz/mbar under room temperature conditions.

For the T_2 measurements, the sample contains 93.4 % of T_2 [126]. The collisional shift is assumed to be similar to the self-collisional shift coefficient of H_2 and D_2 yielding a shift of about 0.3 MHz. From the reported result of HD [103], the pressure shift in this heteronuclear species was found to be twice that of H_2 and D_2 , which was ascribed to the presence of a small permanent dipole moment and the lack of a selection rule prohibiting para-ortho conversion during rotationally inelastic collisions [136]. The DT and HT samples inevitably contain some amounts of D_2 and H_2 , respectively. We conclude that based on previous studies [102–104], and on present data for D_2 , the collisional shift in the present CARS experiments is well below 1 MHz.

Some of the CARS measurements on D_2 were performed from the DT gas sample cell, hence under conditions of a low-density plasma environment, undergoing constant production of about 10^9 electrons per second at an average kinetic energy of 5 keV and the same rate of ion production from the primary beta decays. In addition, secondary electrons and ions are produced from ionization of the neutral gas. The transition frequencies of the D_2 CARS signals were not found to deviate from the signals from a different gas cell filled with 4 mbar of pure D_2 , without addition of radioactive species. We conclude that there occurs no measurable plasma shift on the transition frequencies as reported in Table 3.2.

3.2.6 Frequency uncertainty in the CARS measurements

Table 3.1 lists all the uncertainty contributions to the line center determination in the present CARS study. For T_2 $\text{Q}(J = 1 - 5)$ and DT $\text{Q}(J = 0 - 5)$, the total uncertainty is about 12 MHz. For the T_2 $\text{Q}(0)$ and DT $\text{Q}(6)$ lines the

3. PRECISION MEASUREMENT OF THE FUNDAMENTAL VIBRATIONAL FREQUENCIES OF T₂, DT, HT

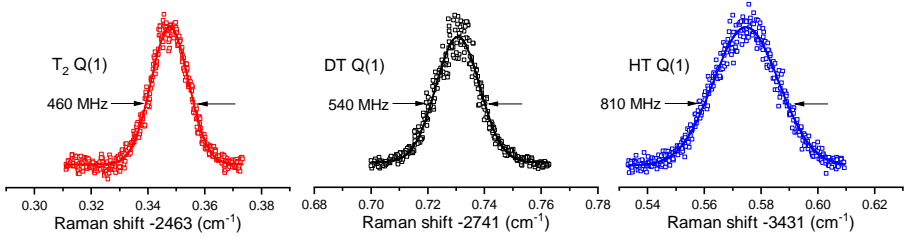


Figure 3.5: High resolution CARS spectra of the Q(1) lines in the fundamental vibrational band ($v = 0 \rightarrow 1$) of T₂, DT, and HT.

uncertainty is estimated at 20 MHz, due to interference effects, which will be discussed in the last section. For HT, the lowest pulse energy used in the measurement was about 2.5 times larger than that for T₂ and DT measurements, thus resulting in a larger uncertainty from the ac-Stark effects. In addition, the Doppler width for the HT lines is 1.4 times larger than that for DT. Such differences are also found in results from different measurement days. For HT, the total uncertainty is about 16 MHz for the Q($J = 0 - 3$) lines.

3.3 Results and Discussions

Representative high-resolution CARS spectra of the ($v = 0 \rightarrow 1$) Q(1) transition for tritiated molecular hydrogen species T₂, DT, and HT are displayed in

Table 3.1: Uncertainty budget for the CARS measurements. Systematic and statistical contributions to the frequency uncertainties in the fundamental vibrational Raman Q($J < 6$) transitions, excluding T₂ Q(0). Values in units of 10^{-4} cm^{-1} and representing 1σ .

Contribution	T ₂ / DT	HT
Pump (ω_P) calibration	2	2
Stokes (ω_S) cw calibration	0.7	0.7
Stokes chirp correction	1.7	1.7
ac-Stark analysis	2	3.3
Collisional shift	0.3	0.3
Plasma shift	0.3	0.3
CARS interference shift	1	1
Statistics	2.3	3
Combined (1σ)	4.2	5.3

Fig. 3.5. The line widths of the Q(1) transitions exhibit the expected Doppler widths with the broadest width for HT (lightest) and narrowest for T₂ (heaviest). While the Q($J = 0 - 5$) transitions in T₂ were previously reported in Ref. [66], these lines have been remeasured in this study and the Q-branch extended up to $J = 7$. Moreover, the ($v = 0 \rightarrow 1$) S($J = 0 - 3$) transitions, which are much weaker than the Q lines, were also investigated in the present work. The DT ($v = 0 \rightarrow 1$) Q($J = 0 - 5$) transitions were recently reported in Ref. [127] and extended here up to $J = 7$. The high-resolution measurements of the HT Q-branch transitions are presented here for the first time. The transition frequencies of the Q-branch lines in the fundamental band interval ($v = 0 \rightarrow 1$) of all tritiated species are listed in Table 3.2.

3.3.1 HT, DT and T₂ transitions

The HT measurements include Q transitions from $J = 0 - 3$, where the signal strength involving higher J states is limited due to decreasing population. The HT partial pressure was somewhat lower than the targeted equilibrium partial pressure of 3.6 mbar due to issues in the HT gas filling procedure. In addition, the lower transmission of the bandpass filter in the spectral region of the HT Q-branch lines, led to a weaker observed signal strength. To compensate for the weaker signals higher pulse energies were employed to obtain sufficient signal-to-noise ratio (SNR). This resulted, however, in a larger ac-Stark uncertainty. These factors as well as the larger Doppler width lead to a larger total uncertainty in the HT transition energies than those of the DT and T₂ measurements. The present Q-branch transition energies are 6.4 cm^{-1} higher than the values reported by Edwards et al. [63]. These discrepancies were already pointed out in the subsequent studies of Chuang and Zare [65] and Veirs and Rosenblatt [64]. The present HT Q-branch measurement results are consistent with and improve the measurement uncertainty of Veirs and Rosenblatt [64] by a factor of 200. Chuang and Zare [65] performed absorption measurements of weakly-allowed dipole P- and R-branch transitions in the (1,0) fundamental band, as well as the (4,0) and (5,0) overtone bands of HT. When converting the transition frequencies of that study [65] into fitted molecular constants, good agreement is found with the present results, which are more accurate by seventeen-fold.

Measurements of the DT Q-branch were reported in our recent work [127] and are extended here to include Q(6) and Q(7) lines. The uncertainty for the much weaker Q(7) line is substantially larger than those for $J < 5$, caused mainly by the asymmetric line profile, which is discussed below. A comparison of the present DT Q-branch transition frequencies with the Q($J = 0 - 4$) values reported by Edwards et al. [63] shows differences of some 0.15 cm^{-1} , hence much larger than their claimed uncertainty of 0.005 cm^{-1} . [63] Veirs and

3. PRECISION MEASUREMENT OF THE FUNDAMENTAL VIBRATIONAL FREQUENCIES OF T₂, DT, HT

Table 3.2: Fundamental vibrational ($v = 0 \rightarrow 1$) intervals of the Q(J) transitions in T₂, DT, and HT. The weaker S($J = 0 - 3$) transitions in T₂ are also listed. The measured values appear in the second column while the theoretical values are listed in the third column, with uncertainties indicated within parentheses in units of the last digit in the indicated value. The last column represents the difference ($\omega_{\text{exp}} - \omega_{\text{calc}}$) with the combined uncertainty from experiment and calculation indicated. Experimental values include corrections from the interference phenomena affecting the CARS lineshape. Lines indicated with asterisks (*) include uncertainty contributions from line profile asymmetry, while those with uncertainties of $5 \times 10^{-3} \text{ cm}^{-1}$ are dominated by ac-Stark broadening. All values in units of cm^{-1} .

Line	Experiment	Calculation	Difference
T₂			
Q(0)	2 464.503 94 (67)*	2 464.504 15 (6)	-0.000 21 (67)
Q(1)	2 463.348 17 (42)	2 463.348 36 (6)	-0.000 19 (42)
Q(2)	2 461.039 17 (42)	2 461.039 17 (6)	+0.000 00 (42)
Q(3)	2 457.581 35 (42)	2 457.581 37 (6)	-0.000 02 (42)
Q(4)	2 452.982 33 (42)	2 452.982 11 (6)	+0.000 22 (42)
Q(5)	2 447.250 61 (42)	2 447.250 85 (6)	-0.000 25 (42)
Q(6)	2 440.397 (5)	2 440.399 34 (6)	-0.002 (5)
Q(7)	2 432.442 (5)	2 432.441 52 (6)	+0.000 (5)
S(0)	2 581.114 (5)	2 581.105 22 (6)	+0.009 (5)
S(1)	2 657.281 (5)	2 657.282 90 (6)	-0.002 (5)
S(2)	2 731.716 (5)	2 731.710 84 (6)	+0.006 (5)
S(3)	2 804.164 (5)	2 804.164 21 (6)	-0.000 (5)
DT			
Q(0)	2 743.341 60 (42)	2 743.341 74 (11)	-0.000 14 (43)
Q(1)	2 741.732 04 (39)	2 741.732 10 (11)	-0.000 06 (40)
Q(2)	2 738.516 62 (42)	2 738.516 97 (11)	-0.000 35 (43)
Q(3)	2 733.704 79 (42)	2 733.704 66 (11)	+0.000 13 (43)
Q(4)	2 727.307 45 (42)	2 727.307 55 (11)	-0.000 10 (43)
Q(5)	2 719.342 21 (42)	2 719.342 02 (11)	+0.000 19 (43)
Q(6)	2 709.828 35 (67)*	2 709.828 32 (11)	+0.000 03 (68)
Q(7)	2 698.787 (5)	2 698.790 48 (11)	-0.003 (5)
HT			
Q(0)	3 434.812 48 (53)	3 434.813 33 (44)	-0.000 85 (69)
Q(1)	3 431.575 09 (53)	3 431.575 53 (44)	-0.000 44 (69)
Q(2)	3 425.112 65 (53)	3 425.113 24 (44)	-0.000 59 (69)
Q(3)	3 415.452 58 (53)	3 415.452 98 (44)	-0.000 40 (69)

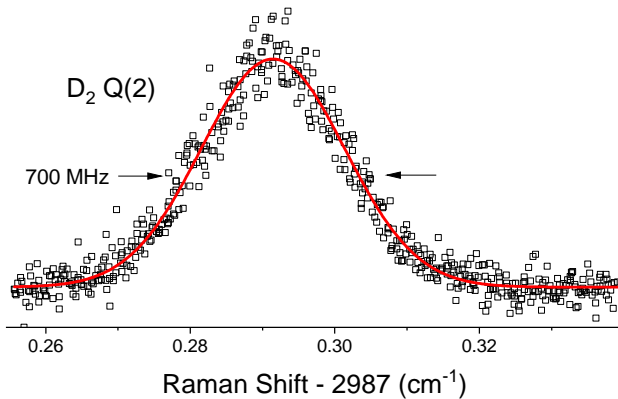


Figure 3.6: Quasi-cw CARS spectra of the Q(2) line in the fundamental band of D₂ recorded at 8 mbar using continuous wave Stokes radiation at 80 mW and a 8-ns pump pulse with 0.47 mJ pulse energy.

Rosenblatt [64] already had cast doubt on the accuracy claimed by Edwards et al. [63] given the discrepancies in the analogous HT and T₂ measurements. The DT Q-branch measurements presented here are consistent with those of Veirs and Rosenblatt [64] and improve the measurement uncertainty by a factor of more than 200 for the Q($J = 2 - 7$) transitions.

The present T₂ Q($J = 0 - 5$) values were obtained after implementing improvements in the setup used in Ref. [66]. Comparing the T₂ results listed in Table 3.2 with the values reported in Ref. [66], reveals an offset of < 0.001 cm⁻¹ for the Q(0), Q(1), and Q(3) transitions while showing consistent values for Q(2), Q(4) and Q(5). We attribute these discrepancies to several difficulties in the measurements of T₂ in the previous study. For example, the cw-seed instability of the pump laser for both CARS laser beams resulted in substantial time jitter leading to poor SNR, especially for weaker transitions. To compensate for such signal loss, the Stokes and the pump pulse energies used during the previous experiment were much higher than in the present study. The cross-sectional areas of both laser beams are now more accurately determined using two methods, a CCD camera beam profiler system and knife-edge method, leading to consistent values. Compared to the estimates of laser intensities in the previous study, [66] these could be off by a factor of three, which is important in the ac-Stark extrapolation studies. A set of measurements, carried out during a day, is based on an extrapolation relying only on relative intensities, assuming little alignment drift, and should lead to robust results. This becomes an issue when combining results of different days where

3. PRECISION MEASUREMENT OF THE FUNDAMENTAL VIBRATIONAL FREQUENCIES OF T₂, DT, HT

any misalignment may lead to a slightly different overlap of the pump and Stokes laser beams, yielding a different effective area for production of CARS signal. Moreover, in the previous study the ac-Stark analysis for all transitions except Q(1) was performed by altering the pump beam intensity only, and thus the ac-Stark shift contribution due to differences in the Stokes beam overlap could be another source for the offset. These shortcomings were repaired in the present study leading to more reliable results.

The frequency calibration of the Stokes laser is also improved in the present study. Some transitions exhibit a more than 0.15 cm^{-1} separation from the calibration line, represented by a particular I₂ hyperfine component. Since such frequency span covers more than 30 markers of the reference etalon, length stabilization is now ensured over the whole recording time by locking to a stabilized HeNe-laser. Improved frequency calibration of the free spectral range (FSR=150.67(2) MHz) of the reference cavity is also applied. The issues discussed here could have led to an underestimate of the uncertainties in the previous study [66]. In addition, the present measurements of T₂ lines in the improved setup allowed for recordings at lower pulse energies than in Ref. [66], resulting in a reduced uncertainty of ac-Stark shift described in the previous section. These improvements have reduced systematic shifts, while at the same time have achieved better sensitivity and enhanced SNR of the recordings. These in turn enabled extending the measurements to weaker Q(6) and Q(7) transitions, as well as the T₂ S-branch with the transition frequencies listed in Table 3.2. The T₂ Q($J = 0 - 5$) results obtained in our new measurements represent a nearly 200-fold improvement compared with results from spontaneous Raman spectroscopy by Veirs and Rosenblatt [64].

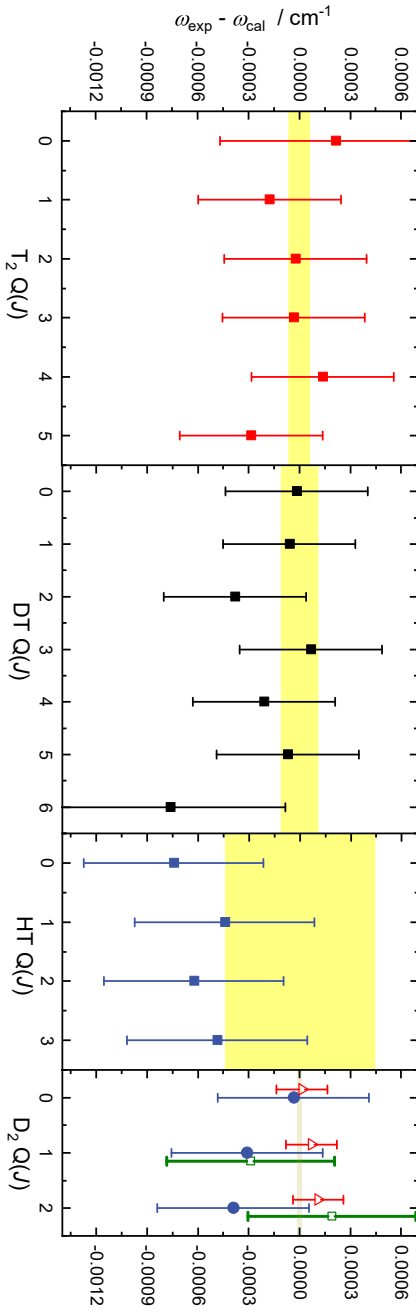


Figure 3.7: Comparison of the experimental and calculated fundamental vibrational intervals of all tritiated species. The error bars on the data points indicate the measurement uncertainty while the (yellow) shaded regions indicate the uncertainty of the calculations. The rightmost trace shows results of CARS spectra for D_2 , measured in a molecular beam expansion (red triangle), from a quasi-cw CARS measurement (green square), and measurements with pulsed pump and Stokes laser beams (blue circle) as used for the tritiated species. The D_2 points are slightly displaced horizontally for clarity.

3.3.2 Benchmark measurements on D₂

CARS measurements on pure D₂ were performed in an identical gas cell focusing on studies of systematic effects, such as the validation of pressure shift effects. This allowed for the comparison of D₂ Q(0), Q(1) and Q(2) of the fundamental vibrational interval with previous precision studies using molecular beams and a deep-UV REMPI scheme [67, 105].

In addition, quasi-cw CARS measurements were performed on D₂ Q(1) and Q(2) lines, using a cw Stokes beam, in combination with a pulsed pump beam. A quasi-cw CARS spectrum of the D₂ Q(2) transition is shown in Fig. 3.6. Such experiments bear the advantage that frequency chirp effects in the Stokes beam are absent. With 80 mW of cw Stokes radiation and a 20 μm beam waist, it was possible to detect the CARS signal using a pump energy of as low as 300 μJ in a cell containing 8 mbar of D₂ gas. The accuracy of these quasi-cw CARS measurements is estimated to be 15 MHz, limited by the ac-Stark extrapolation.

Results of a number of test experiments performed on D₂ are included in the rightmost panel of Fig. 3.7. The results of these studies using pulsed pump and Stokes radiation for Q(*J* = 0 – 2), as well as using pulsed pump and cw Stokes beams for Q(1) and Q(2) are in good agreement with the precision molecular beam experiments in Refs. [67, 105]. These test experiments on D₂ verify the assessment of pressure shifts in the present CARS study. In addition, the use of chirp-free Stokes radiation in the quasi-cw CARS measurements on D₂ validates the chirp correction procedures implemented for the majority of data recorded with the PDA-laser system.

3.3.3 Comparison with calculations

Ab initio calculations, in the framework of NAPT, on level energies in the ground electronic state, are described in Refs. [22, 127] for all tritiated species. Rovibrational level energies and transition frequencies for all molecular hydrogen isotopologues in the ground electronic state can now be accessed through a publicly available program [137]. The differences between experimental results and calculated values, expressed as $\omega_{\text{exp}} - \omega_{\text{calc}}$, are plotted in Fig. 3.7 and listed in Table 3.2.

In Fig. 3.7, the experimental values are represented by data points with error bars attached, while a yellow-shaded region represents the uncertainty of the calculation. Very good agreement between measurement and theory is found for all tritiated species, as can be read from Fig. 3.7. For the tritium-bearing species, the major contribution to the theoretical uncertainty derives from the non-relativistic energy, $E^{(2)}$, which is about $\sim 6 \times 10^{-5} \text{ cm}^{-1}$ for the heaviest T₂ species, and about $\sim 4 \times 10^{-4} \text{ cm}^{-1}$ for HT, owing to its lighter

mass [127]. Hence, the results from the calculations are more accurate than from experiments for T₂ and DT, while for the case of HT a similar accuracy is obtained, due to the less accurate $E^{(2)}$ term.

For the stable species H₂, HD and D₂, the $E^{(2)}$ terms have been calculated directly in a 4-particle variational approach (i.e. without invoking the Born-Oppenheimer approximation and corrections, hence outside the NAPT-framework), achieving 10^{-7} cm⁻¹ uncertainty levels [22]. Therefore, the frequencies for the D₂ species are extremely accurate (1.2×10^{-5} cm⁻¹) [22], as represented by the narrow yellow strip in the rightmost panel of Fig. 3.7.

A similar calculation of improved accuracy might in future be performed for the tritiated species, thereby reducing the total uncertainty to the 10^{-5} cm⁻¹ level, limited by higher-order $E^{(5)}$ and $E^{(6)}$ terms. However, the current theoretical uncertainty of the NAPT-framework is sufficient for a comparison with experimental values, with uncertainties on the order of a few 10^{-4} cm⁻¹ for the tritiated molecular hydrogen species.

3.4 Lineshape analysis

For most lines observed at good signal-to-noise ratios presented in this study, the lineshapes were found to be symmetric. These resonances were fitted with Voigt profiles, dominated by a Gaussian component with Doppler and instrumental contributions. At sufficiently high intensities for strong transitions, saturation dips are observed and were in fact exploited for T₂ spectroscopy in Ref. [66] for the ac-Stark extrapolation. We discuss this saturation effect in this section and its consequence for extracting the line position from the profile. For the weaker transitions such as those in the S-branch of T₂, some asymmetry in the lineshape is observed. We discuss several contributions that result in the asymmetric profiles including the ac-Stark effect, non-resonant background and interference effects occurring in the non-linear optical CARS process.

3.4.1 Saturation CARS spectroscopy

The accuracy of the current CARS measurements is mainly limited by the Doppler-broadened linewidth. In view of testing future improvements of QED-calculations beyond the NAPT-framework experimental uncertainties at the level of $< 10^{-5}$ cm⁻¹ would be desired. Such reduced measurement uncertainties might be achievable via saturated CARS spectroscopy, where a narrow Doppler-free Lamb dip is detected. Saturated CARS profiles were explored by Lucht and Farrow [138] and a theoretical description proposed via a density matrix formalism. In that study, a mechanism for the saturation effect

3. PRECISION MEASUREMENT OF THE FUNDAMENTAL VIBRATIONAL FREQUENCIES OF T_2 , DT , HT

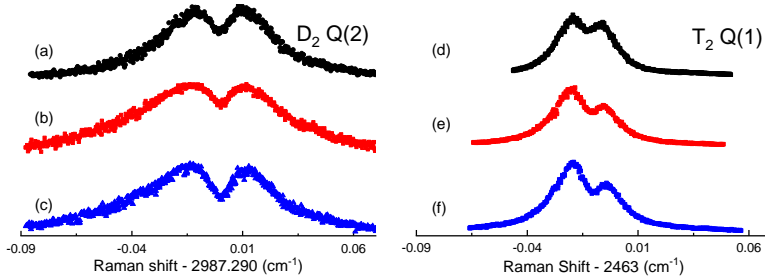


Figure 3.8: Observed spectral profiles for CARS signals exhibiting saturation Lamb dips for two lines recorded at different pump pulse energies. Specific conditions: D_2 Q(2) with Stokes pulse energy 0.74 mJ and pump energy: a) 0.58 mJ; b) 1.2 mJ; c) 1.7 mJ; and T_2 Q(1) with Stokes pulse energy 1 mJ and pump energy: d) 1.5 mJ; e) 1.75 mJ; f) 2 mJ.

was invoked either via strong population pumping or by spectral interference between different velocity classes. The population hole-burning effect in saturation spectroscopy gives rise to typical Lamb dips at the resonance positions, while the spectral interference effect, discussed in detail below, results in the cancellation of the real part of the third order susceptibility of a particular velocity class \vec{u} with that of the opposite direction $-\vec{u}$. Such cancellation is also most pronounced at the resonance position, which then also contributes to saturation of the CARS signal. In a different approach Owyong and Esherrick [139] have demonstrated saturation in stimulated Raman loss spectroscopy of D_2 in a fashion of typical pump-probe spectroscopies, using a three and four-beam counterpropagating configuration. The observed saturation dip exhibited a width of 110 MHz, limited by laser bandwidth [139]. This suggests that with a narrower laser bandwidth and improved frequency calibration procedures, sub-MHz accuracies could potentially be achieved for tritiated species.

We performed systematic studies of saturation CARS on the D_2 Q(2) and T_2 Q(1) transitions. The D_2 Q(2) measurements were performed using a gas cell containing 4 mbar of pure D_2 . A clear saturation feature appears when the pump and Stokes intensity product is $I_P \cdot I_S \sim 5 \text{ GW}^2/\text{cm}^4$. Fig. 3.8 shows recordings at various pump pulse energies. As shown, the width of the Lamb dip in D_2 is about 300 MHz, while the Doppler-limited profile is more than 1.2 GHz wide, with width contributions from the instrument function and power broadening. The spectra were fitted with two Gaussian function components, with opposite amplitude signs to represent the saturation dip and the Doppler-broadened profile. It turned out that the ac-Stark extrapolation curves of the Lamb dip feature and that of the Doppler-broadened envelope do

not produce consistent values for the zero-field transition frequency. The Lamb-dip positions did not show any significant ac-Stark shift, while the Doppler profile followed the ac-Stark shift trend observed at lower intensities, in absence of the saturation feature.

Saturated spectra of the T₂ Q(1) transition, recorded at similar alignment and intensity conditions as for D₂ Q(2), are shown in Fig. 3.8. The T₂ Q(1) saturation dip is observed to be blue-shifted with respect to the center of the Doppler-broadened profile at increasing pump energy, which is qualitatively different to the case of D₂. This may be due to the increasing asymmetry in the ac-Stark broadened profiles at higher pulse energies. Trivikram et al. [84] studied a related phenomenon on the electronic transitions of H₂, where the line shift no longer follows a linear trend at sufficiently high intensities as the transitions exhibit skewed line profiles. This presents a serious difficulty in the ac-Stark extrapolation, as high intensity measurements cannot be used in a linear extrapolation to the ac-Stark free value. The intensity values reported in the previous T₂ study [66] was probably overestimated thus staying in the linear regime for the ac-Stark shift. In the present study, the line positions of the T₂ peaks in Fig. 3.8(d)-(f) already showed a nonlinear dependence.

These phenomena are suspected to be caused by asymmetric ac-Stark broadening due to spatial and temporal intensity variations, such as those discussed in Refs. [84, 140]. While in principle the Lamb-dips should produce more accurate results in determining transition frequencies, more refined studies are required to obtain a quantitative understanding of the saturation effect in CARS and to extract the most accurate line positions from the narrower resonance features.

3.4.2 Asymmetric profile of weak transitions

The CARS measurements were extended to transitions involving higher rotational states up to $J = 7$ for T₂ and DT and also to the weaker S-branch of T₂, with $\Delta J = +2$. The lineshapes for these weaker lines were observed to give rise to asymmetric profiles. These effects are partly caused by the required high intensity in the measurements to compensate for the weakness of transition probabilities, either from having a smaller Raman cross-section or a lower population. The weak transitions are barely detectable with 1 mJ pump and Stokes energy and show different degrees of asymmetry in their spectral profile. Nearly all these weak transitions show different tailing behavior in the flanks below and above the resonance and, despite the higher pulse energy used, no saturation effect at resonance is apparent. As a consequence the accuracy for which the Q($J = 6, 7$) transition frequencies in T₂ and DT, as well as T₂ S($J = 0 - 3$) lines can be determined is much lower than for the strong CARS lines (the transition frequencies of these weak lines are included Table 3.2). We

3. PRECISION MEASUREMENT OF THE FUNDAMENTAL VIBRATIONAL FREQUENCIES OF T₂, DT, HT

discuss three possible effects contributing to the asymmetry: 1) spatial beam profile and time evolution of pulses; 2) ac-Stark splitting of the magnetic sublevels, and; 3) resonant cross interference between lines and interference with the non-resonant background [130].

The first two effects were discussed by Moosmüller et al. [135], studying the spectral profile from coherent Stokes Raman scattering (CSRS) of N₂ exhibiting the effects of spatial and temporal variation of intensity. Similarly as for the CARS profiles investigated here, molecules at different positions in the interaction volume and throughout the time evolution of tightly focused pump and Stokes pulses will have varying contributions to the overall spectrum, because of the spatial and temporal variation of the intensities. It is expected that signal contributions near the focal point, which is highly red-shifted by ac-Stark effect in this case, are the strongest.

Apart from the ac-Stark shift due to the spatial and temporal intensity distribution, the ac-Stark induced splitting of the m_J sublevels, which are unresolved in the measurements, will lead to an asymmetry of the spectral profile. From Eq. (3.3), the second term refers to the ac-Stark splitting for different m_J , where higher $|m_J|$ values experience less shift and overall produce a broadening of the spectrum. Such phenomena of ac-Stark splittings in CARS were quantitatively investigated previously [101, 141]. Here we address such effects phenomenologically in the line fitting of asymmetric lines (see below).

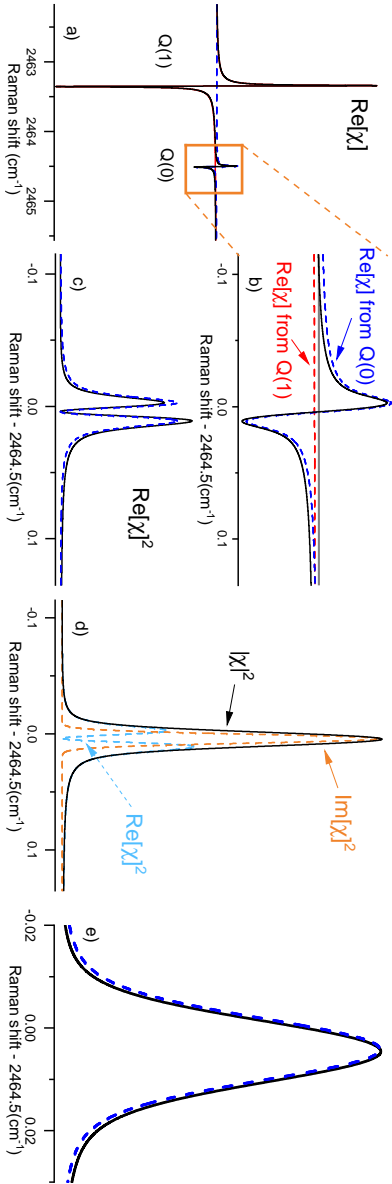


Figure 3.9: Simulation of the CARS spectrum of the $Q(0)$ line of T_2 , focusing on the effect of CARS spectral cross-interference. The real and imaginary contributions of the $Q(0)$ line are drawn in subfigures a) to d). See text for extensive discussion. e) The line profile of the $Q(0)$ line with the cross-interference effect is shown as the solid curve, while the dashed curve represents the case when the effect of interference is neglected. The cross-interference causes a shift of +13 MHz of the $Q(0)$ peak position.

3. PRECISION MEASUREMENT OF THE FUNDAMENTAL VIBRATIONAL FREQUENCIES OF T₂, DT, HT

Another well-known artifact in CARS spectra is the spectral interference in the third order susceptibility $\chi^{(3)}$. The main contribution to the third order non-resonant susceptibility at 532 nm for the pump and 683 nm for the Stokes wavelengths is from the electronic polarizability, with only a smaller contribution due to molecular vibration and rotation [142]. In Eq. (3.1), the third-order susceptibility $\chi^{(3)} = \chi_{\text{NR}} + \chi_{\text{R}}$ comprises of a resonant and non-resonant part giving rise to interference effects in the CARS signal, $I_{\text{AS}} \propto |\chi_{\text{NR}} + \chi_{\text{R}}|^2$ (where the superscript ⁽³⁾ is dropped). The real and positive χ_{NR} , from far off-resonance contributions, will interfere with the real part of χ_{R} and distort the spectrum resulting in a dispersive-like signal.

In the following, we first discuss a numerical study to simulate the effects of the spectral interference effect on the lineshape that eventually shifts the peak position of the resulting profiles. Such shifts are included in the frequency determinations as listed in Table 3.2. Thereafter, a fitting procedure is described using an asymmetric profile applied to the experimental spectra to assess shifts in the peak position. In the latter, it remains difficult to decouple the separate contributions of the ac-Stark effect and spectral interference, giving at best an estimate of possible systematic frequency shifts due to the asymmetric profile. For these cases the uncertainties in the frequency values as listed in Table 3.2 were appropriately enlarged.

3.4.3 Lineshape simulation for interference effects

Following the analyses in Refs. [143, 144] simulations were performed to account for the interference effects in the CARS lineshape that is proportional to the square of the third-order nonlinear susceptibility $|\chi|^2$:

$$|\chi|^2 = \left| \chi_{\text{NR}} + \sum_J a_0(J) \int_{-\infty}^{\infty} \frac{\frac{1}{\sqrt{\pi}u} e^{-v_z^2/u^2} dv_z}{\omega_0(J) - (\omega_{\text{P}} - \omega_{\text{S}}) - i\Gamma - \frac{1}{2\pi}(k_{\text{P}} - k_{\text{S}})v_z} \right|^2, \quad (3.4)$$

where $\omega_0(J)$ is the resonance frequency of a particular transition, Γ is the relaxation rate, $(k_{\text{P}} - k_{\text{S}}) \frac{v_z}{2\pi c}$ is the Doppler shift, and u is the most probable speed $\sqrt{2k_{\text{B}}T/M}$ for temperature T . The integration over the Maxwell-Boltzmann distribution for all velocities v_z along the CARS beam propagation direction can be performed and the equation recast using a Faddeeva function $w(\zeta)$

$$|\chi|^2 = \left| \chi_{\text{NR}} - i \sum_J a_0(J) \frac{\sqrt{\pi}c}{\omega_{\text{R}}u} w \left(\frac{-\omega_0 + \omega_{\text{R}} + i\Gamma}{\omega_{\text{R}} \frac{u}{c}} \right) \right|^2 \quad (3.5)$$

where $\omega_{\text{R}} = (\omega_{\text{P}} - \omega_{\text{S}})$. The $(v = 1, J)$ states are extremely long-lived, hence the Lorentzian width Γ is set to zero in the present low-pressure and Doppler-

limited case. The $a_0(J)$ coefficients for the Q-branch transitions,

$$a_0(J) = \frac{Np(J)}{h} \left(\alpha_0^1(J)^2 + \frac{4}{45} b_J^J \gamma_0^1(J)^2 \right), \quad (3.6)$$

depend on the population number density $Np(J)$ for the rotational ground states J and b_J^J is the Placzek-Teller coefficient. The isotropic α_0^1 and anisotropic γ_0^1 polarizabilities between $v = 1$ and $v = 0$ are estimated from that of H₂, HD and D₂ from Ref. [145], since no values for the tritiated species are available. For $J = 0$, $\alpha_0^1(0) = 0.61$ a.u. and $\gamma_0^1(0) = 0.50$ a.u. and these values do not vary significantly for other J states.

There are two contributions to the interference effect in CARS. Firstly, the summation over all populated states gives rise to cross-interferences χ_R between all lines in the $\nu = 0 \rightarrow 1$ fundamental band, and secondly a nonresonant term χ_{NR} that represents the contribution from the far-lying electronic resonances. The χ_{NR} value is estimated from the H₂ value of 6.7×10^{-18} cm³/erg amagat given in Ref. [146]. For the 2.5 mbar T₂ sample at 298 K, this value converts to 1.5×10^{-20} cm³/erg or 1.5×10^{-20} esu, while for the DT sample with 12.7 mbar total pressure a value of 7.6×10^{-20} esu is estimated. The presence of D₂ in the DT sample results in additional cross-resonance contribution from the D₂ Q-branch (Raman shift at ~ 2991 cm⁻¹) on the DT Q-branch (Raman shift at ~ 2743 cm⁻¹) which is estimated to be 1.8×10^{-20} esu.

Fig. 3.9 illustrates the effect of CARS interference on the T₂ Q(0) line, for which the dominant interference contribution is from the neighboring T₂ Q(1) transition. Since Q(1) is the most intense and the nearest lying resonance, it produces the strongest effect as follows from Eq. (3.5). The real part $\text{Re}[\chi]$ is plotted in Fig. 3.9b showing the spectral region that spans T₂ Q(0), with the grey horizontal line indicating zero amplitude. The dashed blue dispersive line belongs to Q(0) while the dashed red line below zero represents the contribution of the Q(1) line, yielding the solid blue dispersive line as the sum. At the Q(0) resonance position, the nonresonant contribution χ_{NR} is more than a hundred times smaller than the resonant χ_R contribution from Q(1). It is noted that this holds for the present specific case, given the rather low pressures in the sample yielding a small χ_R . The square of the real part of χ is plotted in Fig. 3.9c, with the dashed curve indicating the pure contribution from Q(0) and the solid curve from the summation. Fig. 3.9d, shows both contributions of the real $\text{Re}[\chi]$ and imaginary parts $\text{Im}[\chi]$ of the third-order susceptibility as well as the square $|\chi|^2$. Finally, Fig. 3.9e shows the line profile of the T₂ Q(0) line. The solid line includes the cross-interference effect, while the dashed curve represents the case when the effect of interference is neglected. This numerical example demonstrates how the large CARS susceptibility contribution from T₂ Q(1), due to the factor of 7 higher population in $J = 1$ compared to that of

3. PRECISION MEASUREMENT OF THE FUNDAMENTAL VIBRATIONAL FREQUENCIES OF T₂, DT, HT

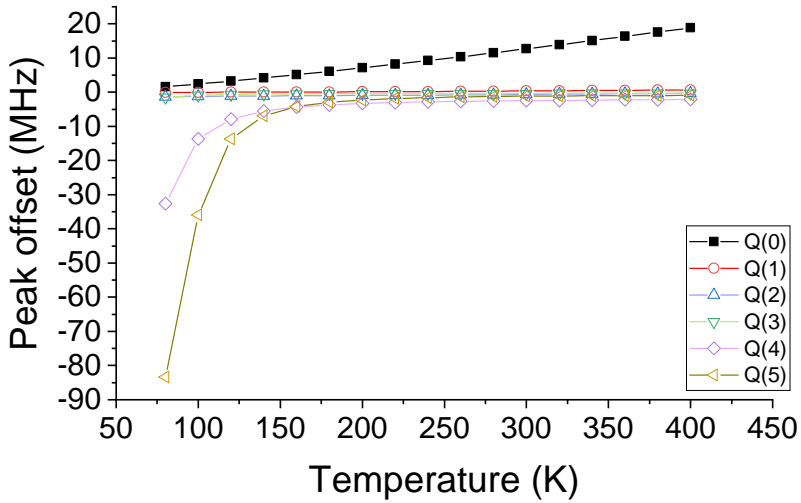


Figure 3.10: Simulated shifts of peak positions of the T₂ Q-branch transitions due to spectral cross-interference as a function of temperature.

$J = 0$ (under room-temperature conditions), results in a large interference with the nearby Q(0) transition leading to a +13 MHz shift in Q(0). The positive sign of the shift in T₂ Q(0) is due to the negative contribution of the real part of the χ susceptibility from the Q(1) transition (see Fig. 3.9b).

Systematic shifts of the line centers due to spectral interference were simulated for all T₂ Q-branch transitions as a function of temperature, and results are shown in Fig. 3.10. The Q(0) line is blue-shifted due to cross-interference with other Q($J \neq 0$) lines. For increasing temperature there are two effects that enlarge the cross-interference shift on the Q(0) line: the population ratio between $J = 1$ and $J = 0$ grows and approaches 9:1 while also the larger Doppler width leads to a stronger interference experienced by Q(0). The sharp drop in the peak position offset of the Q(4) and Q(5) lines below 200 K is due to the drastic decrease in population of the $J = 4, 5$ states. At around 300 K where the measurements were performed, systematic shifts of the line centers for the T₂ Q($J = 1 - 5$) lines were found to be less than 3 MHz.

The Doppler-limited spectra for the DT lines were also simulated and depicted in Fig. 3.11. For the strong DT transitions Q($J = 0 - 5$), the asymmetry in the line profiles is not apparent, and the interference-induced shifts in the line positions are found to be below 3 MHz for Q($J = 0 - 4$), while it is -8 MHz for Q(5). However, for the weaker Q(6) and Q(7) lines, the interference

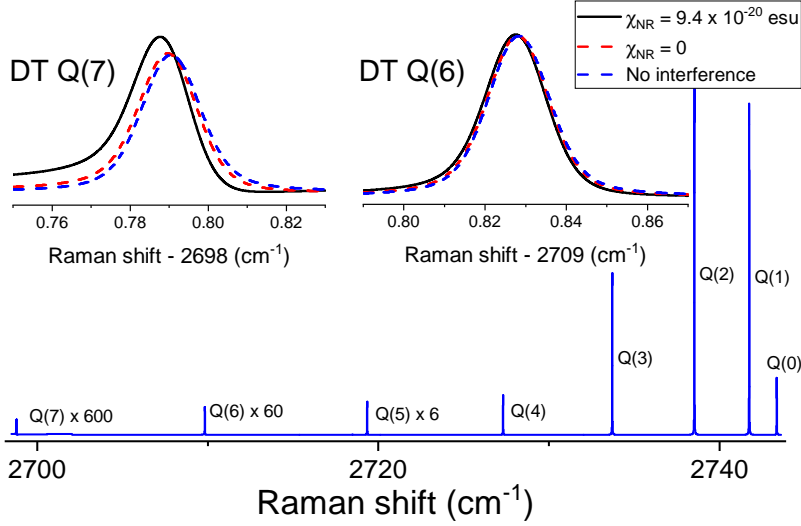


Figure 3.11: Simulation of CARS spectra of DT displaying relative intensities for Q(0-7) lines at room temperature. Zoomed-in spectra of Q(6) and Q(7) are displayed showing the resonant and non-resonant interference effects on these weak lines; a) the blue line represents a symmetric line profile without considering other contributions in the susceptibility; b) the red line represents the cross-interference from nearby line contributions in the fundamental band Q-branch susceptibility; c) the black line represents the inclusion of both interference effects: estimated electronic nonresonant susceptibility χ_{NR} and off-resonance fundamental band Q-branch susceptibility. The shift in peak position of Q(6) and Q(7) from a) and c) is about -24 MHz and -83 MHz, respectively.

effect is more visible as shown in the inset of Fig. 3.11. Based on Eqs. (3.5) and (3.6) the effects of the cross-interferences between the lines as well as the effects of the interference of the non-resonant background are quantitatively evaluated. A shift of -24 MHz is observed for Q(6) and a much higher shift of -83 MHz for the weaker Q(7) line. It is worth noting that for the DT Q(6) and Q(7) lines, the non-resonant susceptibility contribution χ_{NR} is an important contribution that is comparable to the cross-interference contributions, as shown in the insets of Fig. 3.11. The χ_{NR} for the DT sample is higher than in the case of T₂ mainly caused by the higher total pressure in the DT gas cell. Similar simulations were also performed on the HT Q($J = 0 - 3$) lines, with the resulting shifts in peak positions due to CARS interference were found to be less than 3 MHz. The line positions reported in Table 3.2 include corrections to these estimated CARS interference effects.

3.4.4 Lineshape fitting

A phenomenological approach is adopted in fitting asymmetric profiles to experimental data from the combined effects of the ac-Stark and spectral interference phenomena, especially for the weak transitions. While a full quantitative assessment that would separate the contributions of these effects is not possible at present, the lineshape study enables us to better estimate the contribution to the systematic uncertainty resulting from the line profile asymmetry.

For the strong transitions with symmetric line profiles such as Q transitions from $J = 0 - 5$ in T₂, DT and HT, a symmetric Gaussian or Voigt fitting function is used. However, despite the T₂ Q(0) and the DT Q(6) lines appearing to be symmetric, the simulations suggest that interference effects may potentially shift the line center. To estimate a systematic uncertainty contribution due to a choice of the line profile in the fitting of the T₂ Q(0) and DT Q(6) lines, a Faddeeva function $w(\zeta)$ is employed:

$$I_{AS} = y_0 + \left| \chi_{NR} - i a_0 w \left(\frac{-\omega_0 + \omega_R + i\Gamma}{\Delta\omega} \right) \right|^2, \quad (3.7)$$

where $\Delta\omega$ is the Gaussian width and Γ is the Lorentzian width, while y_0 sets the experimental baseline. For T₂ Q(0) and DT Q(6), a 16 MHz discrepancy is observed from the fitting result between a simple symmetric Gaussian profile and the Faddeeva profile in Eq. (3.7). This systematic offset is included in the uncertainty budget of these two lines as listed in Table 3.2.

For other weak lines such as the T₂ Q(6) and S(1) transitions shown in Fig. 3.13, the poor SNR makes it more difficult to separate the effects of the dispersive feature due to spectral interference and the ac-Stark splitting and broadening, leading to larger uncertainties in the line position determination. Note that when compared to the DT Q(6) line in Fig. 3.12, the analogous T₂ Q(6) line in Fig. 3.13 exhibits a more pronounced asymmetry. This is due to the ortho-para spin statistics leading to a lower population for $J = 6$ in homonuclear T₂ species, which is not present in DT. On the other hand, despite the T₂ S(1) line being of comparable strength to T₂ Q(6) (Fig. 3.13), the S(1) line at 2657 cm⁻¹ exhibits a more symmetric profile. This can be explained from competing contributions of opposite sign: the cross-interference χ_R from the T₂ Q-branch at 2464 cm⁻¹ having a negative sign and the non-resonance χ_{NR} background having a positive sign.

In addition to the cross-interference induced shifts in the peak positions (included in Table 3.2), the transition frequencies of the weaker lines are corrected for the ac-Stark shift, using the slope of low-intensity ac-Stark measurements in stronger transitions (e.g. Q(1) transition of the respective species). However, the dominant contribution to the uncertainties of 5×10^{-3} cm⁻¹ for the weak

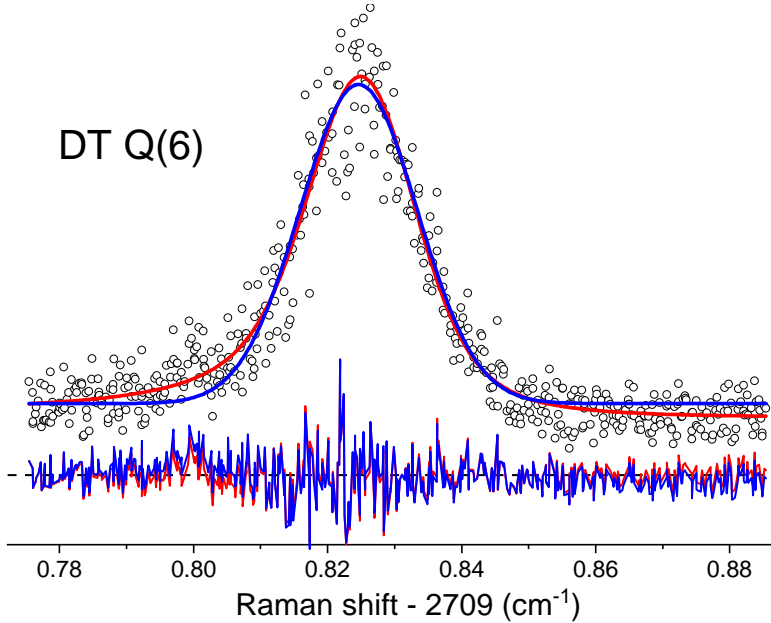


Figure 3.12: Comparison of lineshape fitting of the DT Q(6) transition using the asymmetric profile of Eq. (3.7) (red) and a symmetric Gaussian function (blue). Fitting with the Faddeeva profile, as in Eq. (3.7), gives a better fit especially in the the wing of the spectrum. The difference of central frequency between the two fitting functions is 20 MHz.

lines derives from the large fitting uncertainty in the peak positions given the significant ac-Stark broadening.

3.5 Conclusion and outlook

In summary, we have accurately determined transition frequencies of the fundamental vibrational band ($v = 0 \rightarrow 1$) of HT, DT and T_2 . For most Q-branch transitions with ($J = 0 - 5$), uncertainties below 0.0005 cm^{-1} are achieved, which represent more than a hundred-fold improvement over previous studies. For the weak Q($J = 6, 7$) transitions in T_2 and DT and the S-branch of T_2 , the high pulse intensities required for the measurements cause significant ac-Stark broadening. The transition frequencies of these weak lines are thus reported with a much higher uncertainty of 0.005 cm^{-1} . All measured transition ener-

3. PRECISION MEASUREMENT OF THE FUNDAMENTAL VIBRATIONAL FREQUENCIES OF T_2 , DT, HT

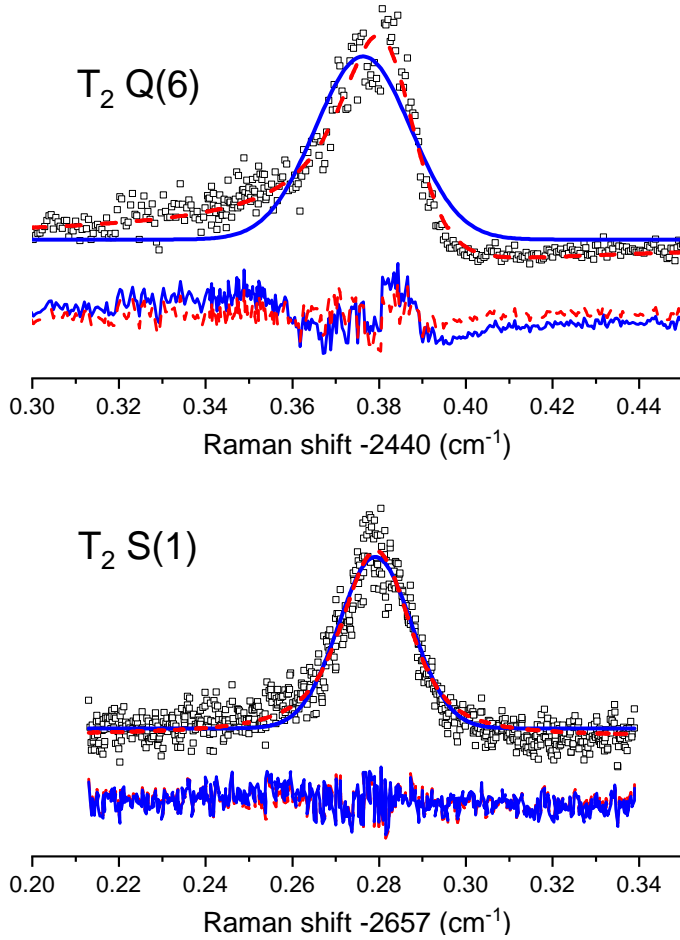


Figure 3.13: Line fitting of the T_2 Q(6) line and the weaker S(1) transition, both with pronounced asymmetries, using a symmetric Gaussian fit (solid - blue) and asymmetric Faddeeva profile (dashed - red). Below the spectra the residuals of different fitting functions are plotted.

gies are in very good agreement with the latest *ab initio* calculations based on NAPT theoretical framework [52, 137]. This work demonstrates that measurements on tritiated species can be achieved at high accuracy, to within a factor of three compared to the accuracy for the non-radioactive species. This doubles the number of benchmark candidates for testing the most accurate quantum chemical calculations of the energy structure of molecular hydrogen.

Due to interference effects with the non-resonant background in CARS spectra, the resulting asymmetric line profiles in weak transitions lead to a higher uncertainty in the line center determination. Cross-interference between resonances can be a limiting factor for the spectroscopic accuracy of CARS measurements; it is shown here that this phenomenon can be quantitatively approached and corrections to transition frequencies calculated.

Future improvements in experiments on tritium-bearing molecular hydrogen would require sub-Doppler techniques, to enable improved comparison with ever advancing calculations. This could be achieved by exploiting Lamb dip spectroscopy with hybrid pulsed-cw CARS, using a pulsed pump beam and a continuous wave Stokes beam, as demonstrated here for D_2 . From these test studies it follows that an improved understanding of line shape profiles, in particular of the ac-Stark effect on Lamb-dips, is required to effectively achieve higher accuracy on the transition frequencies. Improvements might be achieved by using higher cw-Stokes powers, allowing measurements to be performed at even lower pump pulse energies, thereby reducing ac-Stark effects induced by the pump laser. With the narrower cw laser bandwidth and improved frequency calibration procedures, sub-MHz accuracies could potentially be achieved. Ultimately the application of novel cavity-enhanced cw-spectroscopies such as the NICE-OHMS technique on the heteronuclear species HT and DT, with the possibility of Doppler-free saturated absorption, may result in accuracy improvements by orders of magnitude [39], provided that those techniques can be combined with safe handling of radioactive species.

Acknowledgements

Paweł Czachorowski, Krzysztof Pachucki, Jacek Komasa and Mariusz Puchalski are acknowledged for sharing results on theoretical NAPT calculations. We are grateful to Tobias Falke, David Hillesheimer, Stefan Welte and Jürgen Wendel of TLK for the preparation and handling of the tritium cell and gas samples. WU thanks the European Research Council for an ERC-Advanced grant (No 670168). The research leading to these results has received funding from LASERLAB-EUROPE (grant agreement no. 654148, European Union's Horizon 2020 research and innovation programme).

Two-photon Doppler-free ultraviolet laser spectroscopy on sulphur atoms

Abstract

The $3p^4\ ^3P_J - 3p^34p\ ^3P_J$ transition in the sulphur atom is investigated in a precision two-photon excitation scheme under Doppler-free and collision-free circumstances yielding an absolute accuracy of 0.0009 cm^{-1} , using a narrowband pulsed laser. This verifies and improves the level separations between amply studied odd parity levels with even parity levels in S I. An improved value for the $^3P_2 - ^3P_1$ ground state fine structure splitting is determined at $396.0564\ (7)\text{ cm}^{-1}$. A $^{34}\text{S} - ^{32}\text{S}$ atomic isotope shift was measured from combining time-of-flight mass spectrometry with laser spectroscopy.

This chapter is reproduction of: Lai, K.-F.; Salumbides, E. J.; Ubachs, W. Two-Photon Doppler-Free Ultraviolet Laser Spectroscopy on Sulphur Atoms. *J. Phys. B: At. Mol. Opt. Phys.* **2020**, 53 (17), 175002

4.1 Introduction

The odd parity level energies for the neutral sulfur atom have been extensively studied through VUV absorption spectroscopy from the ground electronic configuration [147–150]. The connection with even parity excited states is studied through visible and infrared spectroscopy involving transition between excited states [151–154]. In addition, direct measurements of transitions between even parity states are studied through 2+1 resonance enhanced multiphoton ionization (REMPI) spectroscopy [155, 156].

The level energies of the 1D_2 and 1S_0 states of the $3p^4$ ground electronic configuration, were investigated via electric dipole-forbidden transitions, first measured by McConkey et al. [157], and revisited at higher accuracy by Eriksson [158]. Based on the combination differences between the forbidden transitions, $^3P_1 - ^1S_0$, $^1D_2 - ^1S_0$ and $^3P_2 - ^1D_2$ the level energies of the lowest five levels are determined at an uncertainty of 0.005 cm^{-1} [158]. Later, Brown et al. measured the fine structure transition $^3P_1 - ^3P_0$ using laser magnetic resonance yielding an accuracy better than 10^{-4} cm^{-1} [159]. The resulting level structure of the sulphur atom including a comprehensive compilation of lines and level energies is now well documented [86, 160, 161].

In the present study, high-resolution spectra of $3p^4 \ ^3P_J - 3p^3 4p \ ^3P_J$ transitions of ^{32}S are measured by using 2+1 REMPI employing a narrowband pulsed laser amplifier in a scheme with counter-propagating laser beams, thus allowing for Doppler-free spectroscopy at high resolution and high accuracy. The study is aimed at accurately bridging the large energy gap between the ground state and the manifold of excited states, which can be probed at high accuracy via infrared and visible spectroscopies. Via this means the measurement of a few transitions will allow for improving the accuracy of the entire level structure of the S atom. Moreover it will be shown that isotope shifts can be resolved in such Doppler-free precision experiment.

4.2 Experiment

The experimental setup, schematically shown in Fig. 4.1, is similar to that used for the production and detection of vibrationally excited states in molecular hydrogen, also obtained from photolysis of H_2S [84, 85, 162]. Two ultraviolet (UV) pulsed laser systems are used to produce sulphur atoms and perform the precise two-photon spectroscopy. Sulphur atoms in the $3p^4 \ ^3P_J$ ground state triplet are formed by UV-photodissociation of H_2S molecules, a well studied photolysis process [80, 81, 163, 164]. The first UV-laser pulse, inducing the dissociation, is obtained from a frequency-doubled pulsed dye laser (PDL) pumped by an injection-seeded pulsed Nd-YAG laser. Pulse energies of up to 4.5 mJ

pulse are used for the photolysis. The wavelength of the dissociation laser is chosen at 291 nm following the original work of Steadman and Baer [80, 163].

The two-photon transition is measured by a traveling-wave pulsed-dye-amplifier (PDA) system amplifying the output of a narrowband cw-ring dye laser. The amplification is realized in three consecutive dye cells, pumped with the same Nd-YAG pump laser also used to pump the PDL [95]. The output of the PDA at 616 - 621 nm is frequency-doubled in a KDP crystal to provide UV-pulses in the range 308 - 311 nm with ~ 4 ns pulse width. The frequency of the cw-seed light is calibrated against the standard of I_2 saturated hyperfine lines combined with the transmission markers of a stabilized Fabry-Perot interferometer [97]. The chirp effect on the pulses, giving rise to an effective frequency offset between the pulsed output of the PDA and the cw-light is assessed via optical heterodyne measurements and analyzed via known techniques [95, 165]. The narrowband UV beam is then split and configured in a counter-propagating beam setup to induce the Doppler-free two-photon transitions. The angle mismatch of the counter-propagating beams is reduced based on Sagnac interference fringes [166].

The UV beams are focused into a spot of size few tens of μm spatially overlapping a pulsed H_2S beam, in a low-density region of a skimmed and

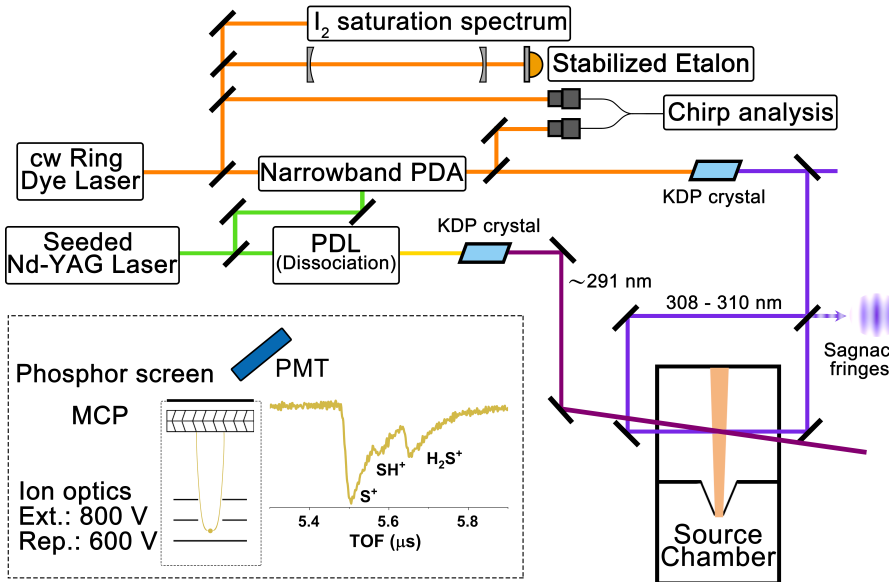


Figure 4.1: Schematic layout of the experimental setup. For details see text.

4. TWO-PHOTON DOPPLER-FREE ULTRAVIOLET LASER SPECTROSCOPY ON SULPHUR ATOMS

Table 4.1: Measured frequencies for the two-photon transitions $3p^4\ ^3P_J - 3p^34p\ ^3P_J$ of ^{32}S , with uncertainties indicated in parentheses.

Initial state	Excited state	Obs. (cm^{-1})
3P_2	3P_1	64888.9317 (9)
	3P_0	64891.3536 (9)
	3P_2	64892.5494 (9)
3P_1	3P_1	64492.8751 (9)
	3P_2	64496.4917 (23)
3P_0	3P_0	64317.7561 (9)
	3P_2	64318.9561 (9)

collimated pulsed effusive gas expansion. To avoid ac-Stark disturbances from the dissociation laser, the PDA spectroscopy laser is optically delayed by 10 ns with respect to the photolysis laser, such that there is no temporal overlap. Sulphur atom signal is generated via 2+1 REMPI, whereby ions are extracted through a mass-resolving time-of-flight (TOF) tube, detecting S^+ ions. Ion optics are triggered at a delay of ~ 50 ns from the spectroscopy laser, so that the laser-excitation takes place in zero DC field. The ion signal is amplified by a microchannel plate (MCP) with phosphor imaging screen with detection on a photomultiplier tube. Mass-selected spectra are recorded with a box-car integrator probing only a narrow channel of the TOF-trace. The large amounts of SH^+ and H_2S^+ signal in nearby mass channels, as well as S^+ background signals from various dissociation/ionization channels are limiting factors on the signal-to-noise-ratio of the S-atom spectra. In case of spectral recording of measuring spectra of ^{34}S this is even more detrimental.

4.3 Results and Interpretation

All of the seven two-photon allowed transitions between $3p^4\ ^3P_J$ and $3p^34p\ ^3P_J$ were measured in the wavelength interval 308-311 nm. Figure 4.2 displays recordings of all observed lines under Doppler-broadened conditions. Note that the combination $J = 0 \leftrightarrow 1$ is forbidden by two-photon selection rules [167].

The spectra for the $3p^4\ ^3P_2 - 3p^34p\ ^3P_2$ and $3p^4\ ^3P_2 - 3p^34p\ ^3P_1$ lines, recorded under Doppler-free conditions, are shown in greater detail in Figs. 4.3 and 4.4. The width of the spectral lines, measured at the lowest power, is about 290 MHz (FWHM), only slightly larger than expected by assuming exact Fourier-transform limited laser pulses of Gaussian spectral profile. The power

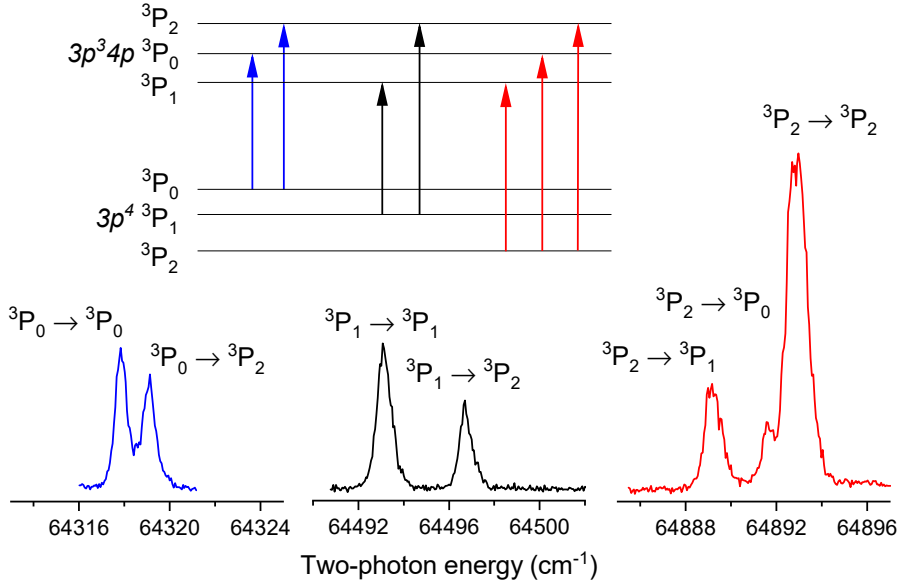


Figure 4.2: Recorded two-photon spectra of all seven components in the $3p^4 \ ^3P_J - 3p^3 4p \ ^3P_J$ multiplet under Doppler-broadened conditions. The inset shows a level diagram connecting the levels probed.

dependence (or ac-Stark effect) for the transition frequencies is studied by varying the PDA pulse energy as shown in the inset of the figures. Table 4.1 lists the transition frequencies, upon extrapolation to zero field, as measured for the seven transitions with the boxcar gate set to ^{32}S .

The sources of uncertainty are summarized in an error budget presented in Table 4.2. A statistical analysis of the determination of the line centers gives an uncertainty of $3 \times 10^{-4} \text{ cm}^{-1}$, including averaging over multiple recordings. The ac-Stark effect is the dominant systematic effect in the present study. It causes a shift of line centers, accompanied by broadening, and due to the spatial variation of laser intensity over the laser focus, also results in an asymmetry of the line profile [84]. The asymmetry was addressed by skewed Voigt profile fitting. Analysis of the line shape results in an additional contribution to the uncertainty of $2 \times 10^{-4} \text{ cm}^{-1}$. The ac-Stark shift is further analyzed by performing measurements over a range of pulse energies of 20 - 100 μJ with extrapolation of the center frequency to zero energy. This adds a contribution to the error budget of $5 \times 10^{-4} \text{ cm}^{-1}$. Further contributions are associated with the frequency chirp in the PDA-system and the absolute frequency cali-

4. TWO-PHOTON DOPPLER-FREE ULTRAVIOLET LASER SPECTROSCOPY ON SULPHUR ATOMS

Table 4.2: Error budget for the two-photon frequencies for the S atom measured in the present study, except for the $3p^4\ ^3P_1 - 3p^34p\ ^3P_2$ line, where the uncertainty is larger.

Contribution	Uncertainty ($\times 10^{-4}\ \text{cm}^{-1}$)
Line profile (fitting)	2
Statistics	3
AC-Stark extrapolation	5
Frequency calibration	3
Cw-pulse offset (chirp)	6
Residual Doppler	< 1
DC-Stark effect	< 1
Total	9

bration against I_2 -hyperfine components, which were analyzed by established techniques [95, 168] and result in a contribution of $6 \times 10^{-4}\ \text{cm}^{-1}$ for the frequency uncertainty. The absolute frequency calibration against I_2 hyperfine components involves uncertainty in the reference frequencies [97] and measurement of the FSR, amounting to $3 \times 10^{-4}\ \text{cm}^{-1}$. For the latter two contributions multiplication by four, for the frequency doubling and the two-photon process, is included. The experiment is essentially Doppler-free, although small shifts of the frequency center may be associated with a non-isotropic velocity distribution of the S-atoms, similar to the case of H_2 investigated [51]. For this reason the counter-propagating laser beams were aligned in a Sagnac interferometer [166] limiting this effect to below $1 \times 10^{-4}\ \text{cm}^{-1}$. Excitation was performed in zero field, hence the DC-Stark effect is negligible on the scale of the present accuracy. Taking the contributions in quadrature leads to a total uncertainty of $0.0009\ \text{cm}^{-1}$ for the frequencies of the two-photon resonances for all observed transitions except for one. The uncertainty of $3p^4\ ^3P_1 - 3p^34p\ ^3P_2$ is estimated at $0.0023\ \text{cm}^{-1}$ with larger uncertainty from statistics, a long measurement trace to be covered for reaching an I_2 resonance, and problems encountered in ac-Stark extrapolation.

In a single case, for the strongest line $^3P_2 - ^3P_2$, a study was made of the resonance line in ^{34}S from the 5% naturally abundant isotope in the sample. The spectrum, shown in Fig. 4.5, and recorded with a boxcar gate probing mass-34, displays the much lower signal-to-noise ratio, caused by spurious signal on mass-34 of H_2S^+ ions. When only considering the statistical line fitting and relative calibration errors the isotope shift on the resonances amounts to $0.0179\ (4)\ \text{cm}^{-1}$. The spectrum of Fig. 4.5 shows that the spectral contributions of

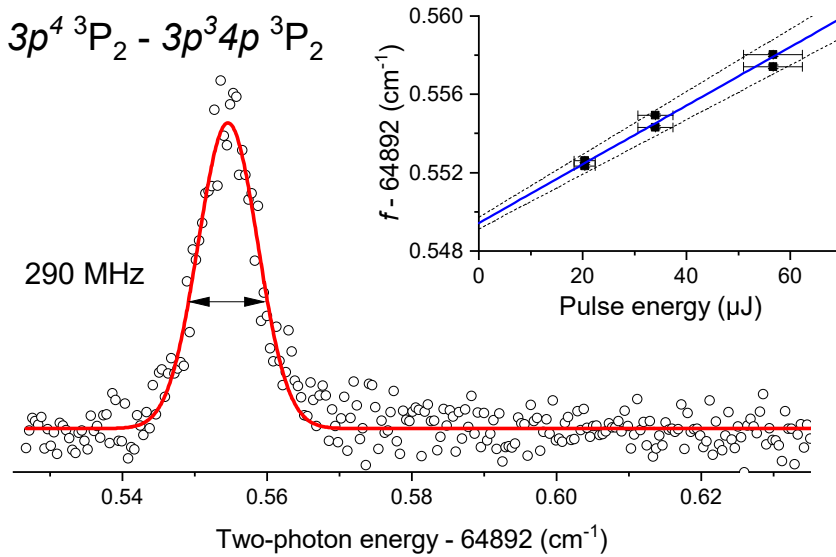


Figure 4.3: Spectrum of $3p^4 \ ^3P_2 - 3p^3 4p \ ^3P_2$ two-photon transition of S I recorded at lowest power and fitted with Voigt function. The inset shows the power dependence of the transition frequency denoted with f .

^{32}S and ^{34}S are well separated, thus verifying that the listed entries for the transition frequencies in Table 4.1 pertain to the main ^{32}S isotope, and do not correspond to a mixture of isotopes.

The isotope shift for a transition can be separated into normal mass shift, specific mass shift and field shift contributions [169]. In view of the very small wave function amplitude of the p outer electron within the nuclear charge radius, the field shift (or finite size) contribution is negligible for the differential isotope effect. The Bohr shift or normal mass shift ($\Delta E_{\text{NMS}} = E_{\text{NMS}}(^{34}\text{S}) - E_{\text{NMS}}(^{32}\text{S})$) is calculated to be 0.0650 cm^{-1} . From the experimental isotope shift obtained here, a specific mass shift of $\Delta E_{\text{SMS}} = -0.0471(4) \text{ cm}^{-1}$ is extracted for the $3p^4 \ ^3P_2 \rightarrow 3p^3 4p \ ^3P_2$ transition. The ΔE_{SMS} experimental value will be useful in validating *ab initio* calculations of electron correlations.

4.4 Discussion: Level energies

The precise determination of transition frequencies can be cast into a least-squares analysis to determine level energies in both ^3P states in the $3p^4$ and

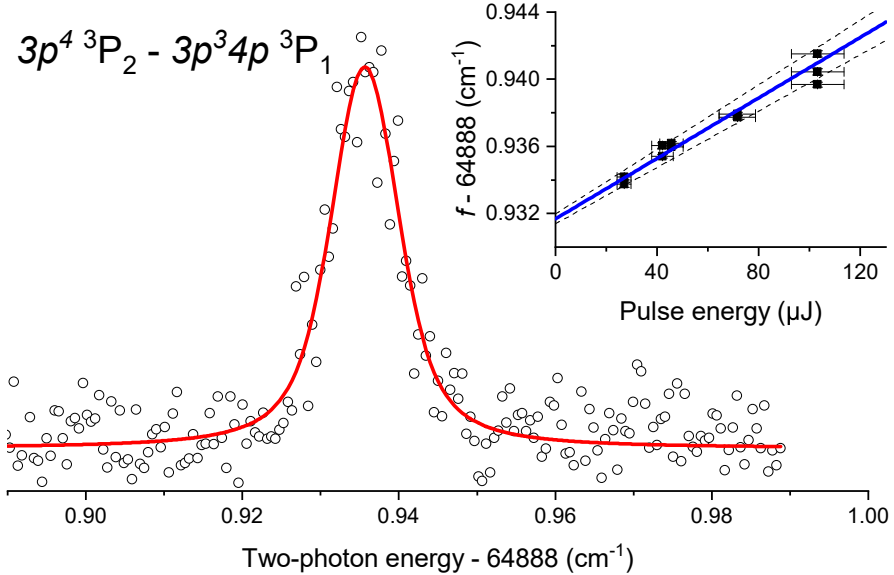


Figure 4.4: Spectrum of $3p^4\ ^3P_2 - 3p^3 4p\ ^3P_1$ two-photon transition of S I; same details as Fig. 4.3.

$3p^3 4p$ configurations using the LOPT program [170]. First the internal consistency of the measurements can be tested by including only the presently obtained data set, as is done in Table 4.3. The LOPT analysis provides a consistent set of level energies at an accuracy in most cases below 10^{-4} cm^{-1} . More importantly the deduced ground state splitting between 3P_1 and 3P_0 levels is in full agreement (within 1σ) with the very accurate laser-magnetic-resonance measurement [159], the most precise level splitting determined in the sulphur atom. This agreement provides proof that the uncertainties of the present study are not underestimated.

In Table 4.3 also a comparison is made with the results from VUV spectroscopy, which are at the basis of the comprehensive published line and level lists [86, 147, 160]. In these compilations a single spectral line in the VUV is included (a transition to the $4s\ ^3S_1$ level) for which an uncertainty as low as 0.025 cm^{-1} is stated [147]. We adopt this value as the general uncertainty for the level energies for the excited states, although the uncertainty for the overall level structure might be somewhat larger. The increased precision on the 3P ground state level energies in the compilations, so better than the quoted 0.025 cm^{-1} , in fact derive from the rather accurate measurement of the forbidden

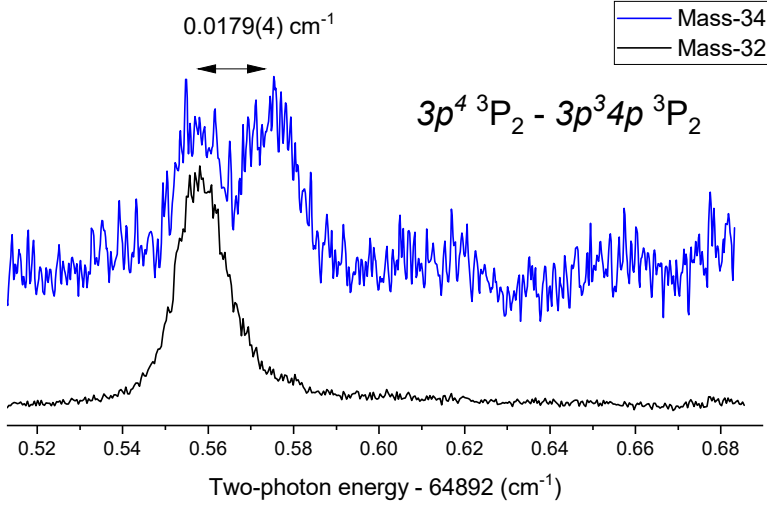


Figure 4.5: Isotope shift in the $3p^4 \ ^3P_2 \rightarrow 3p^3 4p \ ^3P_2$ transition of the ^{34}S isotope (blue curve) recorded by gating on the mass-34 channel, which coincides with the H_2S^+ signal. Resonance signal from the main isotope ^{32}S is still observable in the mass-34 channel, overlapping the spectrum observed in mass-32 channel (black curve).

Table 4.3: Least-square fitting for level energy of $3p^3 4p \ ^3P_J$ and $3p^4 \ ^3P_J$ of ^{32}S , with uncertainties relative to ground $3p^4 \ ^3P_2$ state indicated in parentheses. A comparison is given with values given in Ref. [86]; for the quoted uncertainties see text. All values are given in cm^{-1} .

Level	This work	Ref. [86]	Difference
$3p^4 \ ^3P_2$	0	0	—
$3p^4 \ ^3P_1$	396.0570 (11)	396.055 (5)	0.0020
$3p^4 \ ^3P_0$	573.5953 (9)	573.640 (16)	-0.0447
$3p^3 4p \ ^3P_1$	64888.9319 (9)	64888.964 (25)	-0.0321
$3p^3 4p \ ^3P_0$	64891.3525 (8)	64891.386 (25)	-0.0335
$3p^3 4p \ ^3P_2$	64892.5503 (7)	64892.582 (25)	-0.0317
	This work	Ref. [86]	Ref. [159]
$^3P_0 - ^3P_1$	177.5383 (14)	177.585 (17)	177.539253 (93)

Table 4.4: Least-square fitting for level energy of ground electron configuration $3p^4$ of ^{32}S , with uncertainties indicated within parentheses. The transition from Ref. [158, 159] and this work are included in fitting, and a comparison is made with the data compilation of Ref. [86]. All values are given in cm^{-1} .

Level	This work	Ref. [86]
$^3\text{P}_2$	0	0
$^3\text{P}_1$	396.0564 (7)	396.055 (5)
$^3\text{P}_0$	573.5956 (7)	573.640 (16)
$^1\text{D}_2$	9238.6097 (23)	9238.609 (5)
$^1\text{S}_0$	22179.9548 (22)	22179.954 (5)

transitions by Eriksson [158]. The $^3\text{P}_0$ level was not accessed in the measurement of Ref. [158], hence its uncertainty relies on VUV-data. Viewed in this context the deviations between present results and the VUV-compilation [147], as listed in Table 4.3 both for ground state splittings and $3p^34p$ excitation energies are close to the expected uncertainties. This includes the consistent shift -0.032 cm^{-1} for all three levels in the $3p^34p$ $^3\text{P}_J$ excited triplet. This finding is indicative for an overall systematic shift of all excited level in the data compilation by 0.03 cm^{-1} .

Finally a LOPT least-squares analysis can be performed to determine the level energies of the entire $3p^4$ ground electronic configuration including $^1\text{D}_2$ and $^1\text{S}_0$ levels, based on the present study in combination with the high-precision measurements of magnetic dipole transitions in Ref. [158, 159]. Table 4.4 lists the fitted level energy values with individual uncertainties relative to ground state and comparison with the corresponding values listed in the S-atom data compilation [86]. This results in an improved level structure for $3p^4$, in particular for the lowest fine structure splitting $^3\text{P}_2 - ^3\text{P}_1$ which is determined at $396.0564 (7) \text{ cm}^{-1}$, corresponding to a far-infrared wavelength of $25.24893 (4) \mu\text{m}$.

4.5 Conclusion

In conclusion, seven transitions in the of $3p^4$ $^3\text{P}_J - 3p^34p$ $^3\text{P}_J$ multiplet are measured by narrowband laser spectroscopy at an uncertainty of 0.0009 cm^{-1} . For the first time a $^{34}\text{S} - ^{32}\text{S}$ isotope shift has been measured in atomic sulphur, from which a value for the specific mass-shift was derived, a measure for electron correlations in the atom. The accurate transition frequencies improve the level energies of the $3p^4$ ^3P ground electronic configuration by factor of two. The

$3p^34p\ ^3P_J$ excited state level energies are determined at an absolute accuracy of less than 0.001 cm^{-1} . The present study provides an indication of an overall systematic shift for the excited level energies as listed in spectroscopic data compilations for the sulphur atom [86, 147, 160]. The precise measurement of even parity excited states may help optimizing the level energies of odd parity levels by future improved measurements between excited states in the infrared and visible regions, therewith using the $3p^34p\ ^3P_J$ levels as anchor levels, in a similar fashion as applied to H_2 [171].

Acknowledgement

WU acknowledges the European Research Council for an ERC Advanced grant (No: 670168).

Photolysis production and spectroscopic investigation of the highest vibrational states in H₂ (X¹Σ_g⁺ $v = 13, 14$)

Abstract

Rovibrational quantum states in the X¹Σ_g⁺ electronic ground state of H₂ are prepared in the $v = 13$ vibrational level up to its highest bound rotational level $J = 7$, and in the highest bound vibrational level $v = 14$ (for $J = 1$) by two-photon photolysis of H₂S. These states are laser-excited in a subsequent two-photon scheme into F¹Σ_g⁺ outer well states, where the assignment of the highest (v, J) states is derived from a comparison of experimentally known levels in F¹Σ_g⁺, combined with *ab initio* calculations of X¹Σ_g⁺ levels. The assignments are further verified by excitation of F¹Σ_g⁺ population into autoionizing continuum resonances which are compared with multi-channel quantum defect calculations. Precision spectroscopic measurements of the F-X intervals form a test for the *ab initio* calculations of ground state levels at high vibrational quantum numbers and large internuclear separations, for which agreement is found.

This chapter is reproduction of: Lai, K.-F.; Beyer, M.; Salumbides, E. J.; Ubachs, W. Photolysis Production and Spectroscopic Investigation of the Highest Vibrational States in H₂ (X¹Σ_g⁺ $v = 13, 14$). *J. Phys. Chem. A* **2021**, 125 (23), 1221–1228

5.1 Introduction

The hydrogen molecule has been the benchmark species of molecular spectroscopy since the first analysis of its dipole-allowed absorption spectrum, now over a century ago [172]. Over decades further detailed experiments on the electronic spectrum were performed [73, 173, 174], while also the measurements of forbidden vibrational transitions were explored [175]. Alongside, and stimulated by experimental observations, the quantum theory of the ground state of smallest neutral molecule was developed with major contributions from James and Coolidge [6], Kołos and Wolniewicz [10], and Wolniewicz [13]. The excited states and the strong effects of non-adiabatic interactions were investigated by Dressler and coworkers [176]. The theoretical program of refined calculations of the ground state structure was further extended by Pachucki and coworkers including effects of non-adiabatic, relativistic and quantum-electrodynamical (QED) effects [22, 117], which has now produced an on-line program (H2SPECTRE [177]) to compute level energies for all rovibrational states of the hydrogen isotopomers [52].

Spectroscopic studies of molecular hydrogen have included the behavior at long internuclear separation. Characteristic for the level structure of H_2 is the occurrence of double-well potential energy curves for excited states, induced by strong non-adiabatic interactions in this light molecule. In the manifold of g -symmetry the lowest of these is the $\text{EF}^1\Sigma_g^+$ state, for which the outer well was investigated [178, 179], followed by the $\text{GK}^1\Sigma_g^+$ and $\text{HH}^1\Sigma_g^+$ states [11, 180]. Similarly double-well states of $^1\Pi_u$ symmetry [181, 182] and of $^1\Sigma_u^+$ symmetry were investigated [183, 184]. These studies on long-range effects in the hydrogen molecule were extended to higher energies, leading to observation of exotic phenomena as ion-pair or heavy Rydberg states [185], quasi-bound states [186] and shape resonances [187] in the molecular ion.

Various approaches have been followed to investigate H_2 in vibrationally excited states of the $X^1\Sigma_g^+$ electronic ground state, also exhibiting wave function density at large internuclear separation. Moderately excited v -levels were probed in chemical reaction dynamical studies [76, 77], with hot filaments [78, 79], and in a high voltage discharge [179]. Instead of producing the vibrationally excited states over a wide population distribution, Zare and coworkers proposed Stark-induced Raman passage to prepare a single desired state of H_2 [188] and recently showed controlled transfer of large population to $v = 7, J = 0$ [189].

Steadman and Baer investigated the production of vibrationally excited states via the two-photon ultraviolet photolysis of H_2S [80]. The results of this one-laser experiment was further investigated in two-laser [83] and three-laser experiments [84, 85] leading to accurate level energies and test of quantum electrodynamics in $X^1\Sigma_g^+$, $v = 11 - 12$. Alternatively, the UV-photolysis of

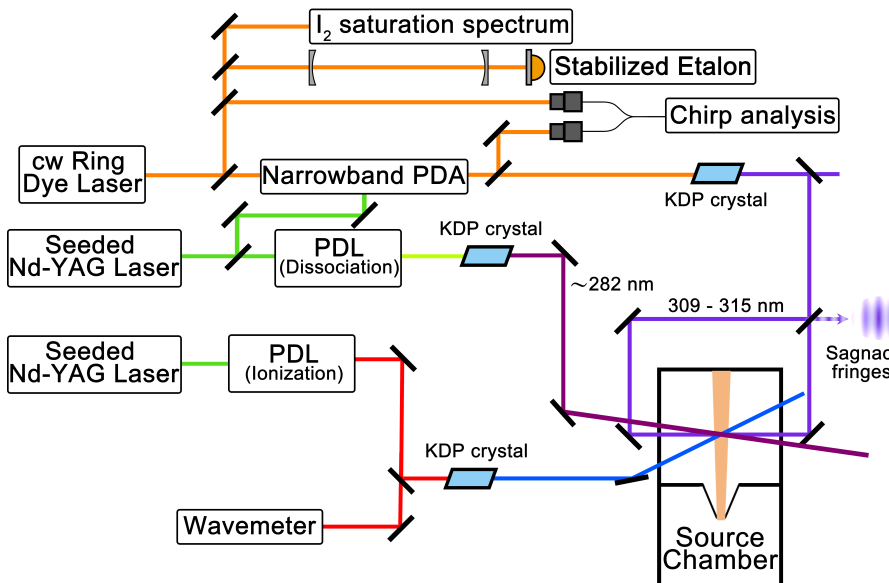


Figure 5.1: Schematic layout of the experimental setup including the three UV-lasers, the calibration units and the vacuum chambers. For details see text.

formaldehyde (H_2CO) was used for the production and investigation of H_2 in $X^1\Sigma_g^+$, $v = 3 - 9$ [190]. In these studies the wave function density at large internuclear separation, as occurring in high- v states, was probed via two-photon excitation to the $F^1\Sigma_g^+$ outer well state.

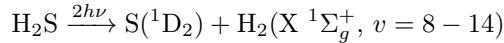
In the present study, the two-photon UV photolysis production of vibrationally excited H_2 from H_2S is extended by increasing the photon energy of the dissociation laser. By this means the dissociation channel for producing $X^1\Sigma_g^+$, $v = 13 - 14$ becomes energetically possible. These highly excited vibrations are interrogated with Doppler-free $2+1'$ resonance multiphoton ionization (REMPI) spectroscopy in a three-laser scheme. Precision measurements probing $F^1\Sigma_g^+$, $v = 0, 1$ outer well levels allow for testing high-accuracy quantum chemical calculations of H_2 in the regime of large internuclear separation.

5.2 Experiment

The experimental layout, shown in Fig. 5.1, is similar to the one used in previous studies probing H_2 in $v = 11, 12$ [84,85]. Three ultraviolet (UV) pulsed laser systems are involved for producing the highest vibrational levels in H_2 from

5. PHOTOLYSIS PRODUCTION AND SPECTROSCOPIC INVESTIGATION OF THE HIGHEST VIBRATIONAL STATES IN H₂ (X¹Σ_g⁺ v = 13, 14)

H₂S photolysis and detection by 2+1' REMPI. The two-photon UV-photolysis proceeds via the path:



The wavelength of the dissociation laser is set at 281.8 nm, as opposed to 291 nm in the previous studies, since the energy required for complete dissociation of H₂S to form an S(¹D₂) atom and two H(²S) atoms is about 69935(25) cm⁻¹ [81]. The two-photon energy for 281.8 nm dissociation lies about 1000 cm⁻¹ above this limit, which is needed to produce H₂ in the highest vibrational levels close to the dissociation limit. Focused UV-pulses at energies of 4.5 mJ are used for the photolysis step.

Vibrationally excited H₂ is interrogated by a narrowband pulsed-dye-amplifier (PDA) system via probing of the F¹Σ_g⁺-X¹Σ_g⁺ two-photon transition. The PDA is seeded by the output of a continuous wave (cw) ring-dye laser and its pulsed output is frequency doubled in a KDP crystal to deliver wavelength tunable UV pulses in the range 309 - 315 nm. The bandwidth of this PDA is about 150 MHz in the UV. The UV pulse is split and configured into a counter-propagating geometry, shown in Fig. 5.1, and adjusted into a Sagnac interferometric alignment for reducing possible Doppler shifts [166]. The absolute frequency of the cw-seed light is calibrated by measurement of hyperfine-resolved saturation spectra of I₂ for reference, where markers of a stabilized etalon are used for interpolation. The chirp of the pulses of the PDA is analyzed and corrected for following known procedures [95].

The third UV pulse, obtained from another frequency-doubled pulsed-dye-laser (LIOP-TEC), excites population in the F¹Σ_g⁺-state into the H₂⁺ ionization continuum for detection. The autoionization spectra from F-states are recorded by scanning through 315 - 320 nm. The frequency of PDL output is calibrated with a HighFinesse WSU-30 (Toptica) wavemeter. In the case when precision measurements on the F-X transitions are performed, the third UV-laser is set on a strong autoionization resonance for signal optimization. Figure 5.2 illustrates the level structure of the H₂ molecule and the various excitation steps induced in the three-laser scheme.

All three UV beams are focused to a few tens of μm and are spatially overlapped with the H₂S effusive molecular beam. The PDA-spectroscopy laser is optically delayed by 10 ns from the dissociation laser, which is pumped by the same Nd:YAG pump laser. This is to avoid an ac-Stark shift induced by the photolysis laser. For the same reason, the ionization laser is electronically delayed from the spectroscopy laser by 30 ns. H₂⁺ ions produced are extracted into the mass-resolving time-of-flight tube and detected on an multichannel plate. The ion optics are triggered at about 50 ns delay from the ionization laser for avoiding dc-Stark fields during excitation.

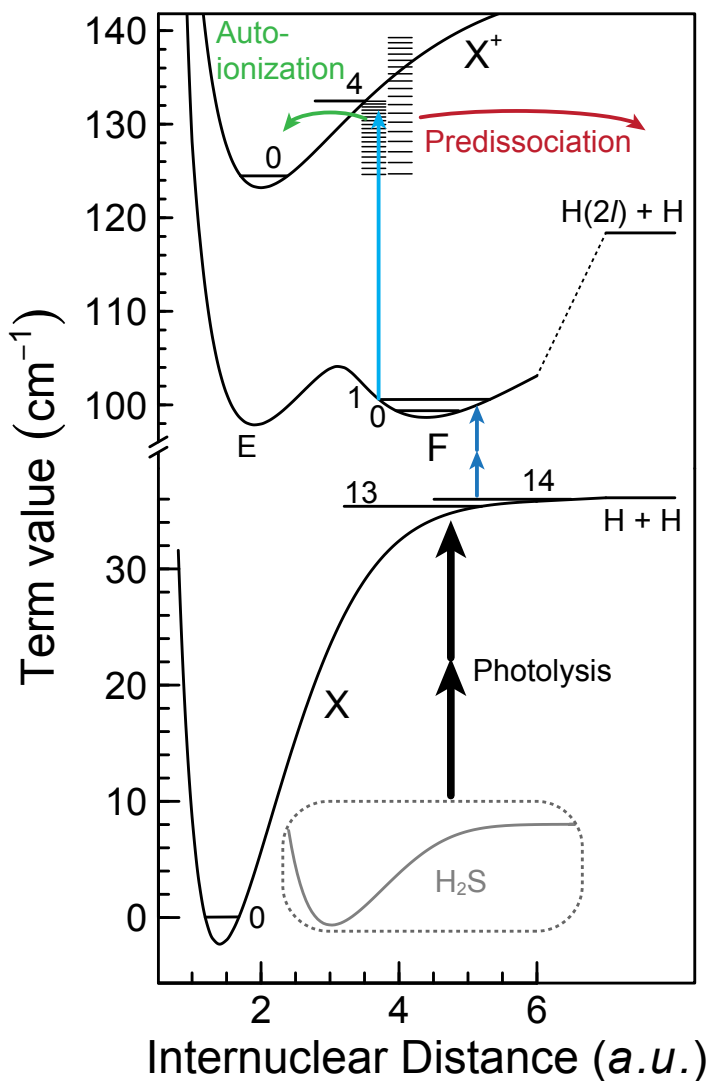


Figure 5.2: The excitation scheme followed in the present study. The highly excited H₂ ($v = 13, 14$) states are produced by two photon UV-photolysis of H₂S. These states are subsequently interrogated via 2+1' resonance-enhanced multi-photon ionization (three-laser scheme), while some overview spectra are recorded via 2+1 REMPI (two-laser scheme). For further details see text.

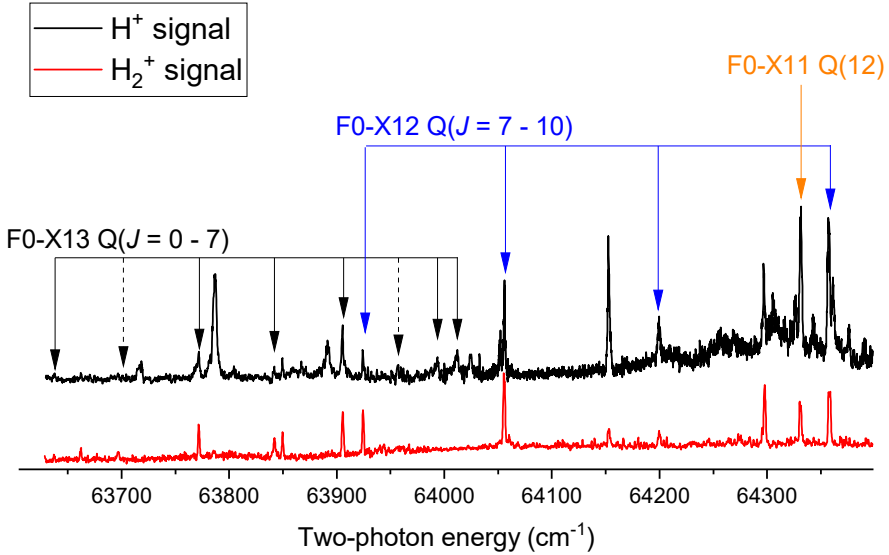


Figure 5.3: Low-resolution overview spectra of the $F^1\Sigma_g^+-X^1\Sigma_g^+(0,13)$ and $F^1\Sigma_g^+-X^1\Sigma_g^+(0,12)$ bands probed via one-color 2+1 REMPI with a tunable frequency-doubled pulsed dye laser upon H_2 photolysis. Signals are recorded for both H^+ and H_2^+ .

5.3 Results

First an overview spectrum was recorded using 2+1 REMPI on the $F^1\Sigma_g^+-X^1\Sigma_g^+$ system in H_2 probing the population of high vibrational states in $X^1\Sigma_g^+$. This is done in a two-laser experiment, photolysis followed by one-color 2+1 REMPI, similar as in [83], using both H_2^+ and H^+ detection. Here the resolution is limited by the bandwidth of the frequency-doubled pulsed dye laser ($\sim 0.1 \text{ cm}^{-1}$) used in the spectroscopy step. This overview spectrum, presented in Fig. 5.3, displays rotational Q-lines in the F0-X12 and F0-X13 bands, along with some additional resonances, some of which could not be assigned. It is noted that the intensity of the lines is affected by the excitation step into the autoionization continuum via the resonant photon energy. The assignment of the F-X resonances derives from a comparison with combination differences between experimental level energies in $F^1\Sigma_g^+$ [171] and those of $X^1\Sigma_g^+$, obtained from the precise *ab initio* computations [177].

Subsequently, precision measurements of the $F^1\Sigma_g^+-X^1\Sigma_g^+$ electronic transitions are recorded under Doppler-free conditions, applying 2+1' two-color

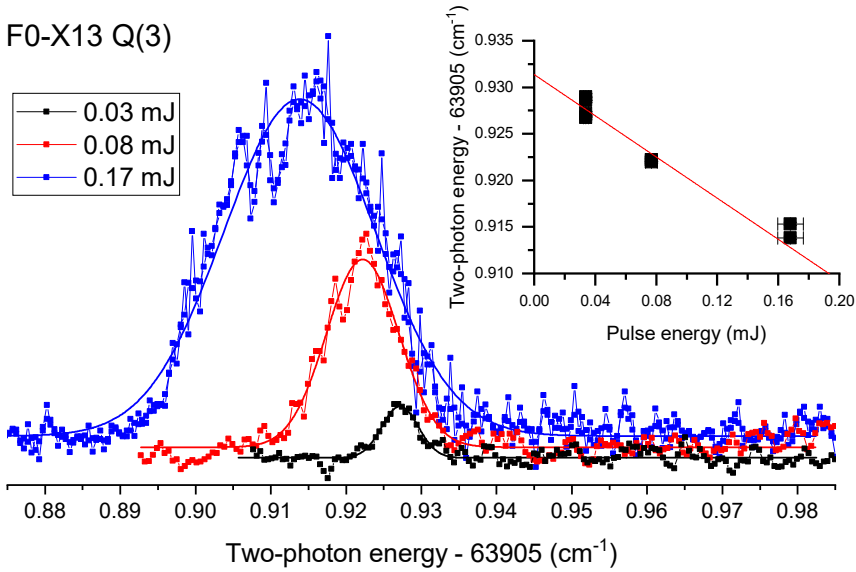


Figure 5.4: Spectra of the F0 - X13 Q(3) transition recorded in a two-color 2+1' REMPI scheme with tuning of the narrowband frequency-doubled PDA-system with counter-propagating UV-beams. The inset shows the ac-Stark extrapolation to zero power levels.

REMPI in the three-laser scheme. While scanning the narrowband frequency-doubled PDA-system over the resonance, the third laser is set at a wavelength probing a strong as possible autoionization resonance, to be found in an iterative process. For these measurements H_2^+ ions are detected for registration of the spectra. Several Q-branch lines are measured probing $\text{X}^1\Sigma_g^+$, $v = 13$ levels (denoted as X13) in excitation to the lowest vibrational level (F0) in the $\text{F}^1\Sigma_g^+$ outer well for which the Franck-Condon factor is favorable [191]. All the odd J states of $v = 13$ are detected, where $J = 7$ is the highest bound state for $v = 13$ in H_2 . Additionally, the Q(2) line in F0-X13 could be recorded, while the other even J states of para-hydrogen appeared to be too lowly populated to be detected in the high resolution measurement. Two of such spectra, for the Q(3) and Q(7) lines, are displayed in Figs. 5.4 and 5.5.

For the $\text{X}^1\Sigma_g^+$, $v = 14$ ground vibration a high resolution recording could only be recorded for the $J = 1$ level at a low signal-to-noise ratio. Power-dependent spectral recordings are shown in Fig. 5.6, where also an ac-Stark extrapolation curve is displayed. Excitation from other levels in $v = 14$ re-

5. PHOTOLYSIS PRODUCTION AND SPECTROSCOPIC INVESTIGATION OF THE HIGHEST VIBRATIONAL STATES IN H_2 ($X^1\Sigma_g^+$ $v = 13, 14$)

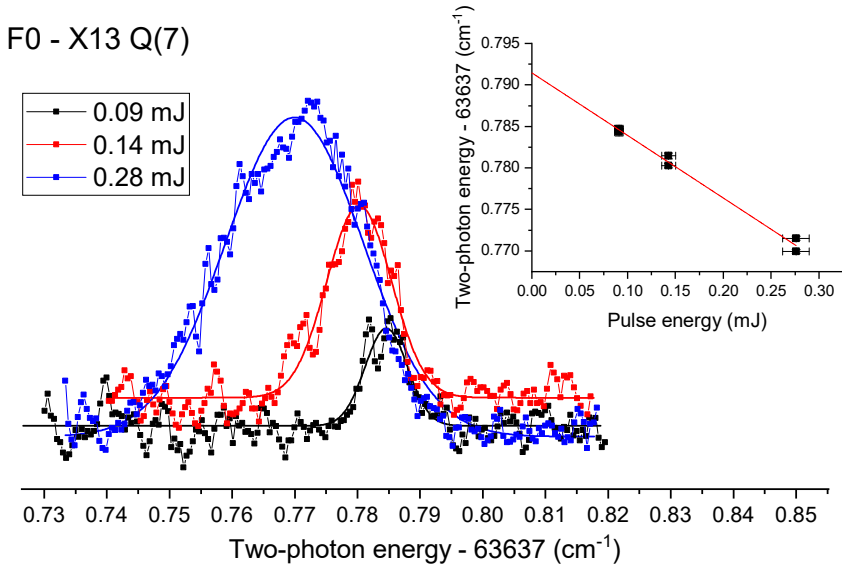


Figure 5.5: Spectra of the F0 - X13 Q(7) transition; details as in Fig. 5.4.

mained below the noise level.

The various sources of measurement uncertainty for the F1-X13 Q-branch lines, recorded in the three-laser scheme, are listed in Table 5.1. The major contribution to the total uncertainty is the statistical analysis over multiple sets of measurements, amounting to $2 \times 10^{-3} \text{ cm}^{-1}$. The uncertainty in the frequency calibration of the cw-seed light, from the measurement of I_2 -hyperfine lines and interpolation of FSR-markers of the reference etalon, contributes overall $3 \times 10^{-4} \text{ cm}^{-1}$ to the uncertainty. The chirp-induced frequency offset between the pulse generated from PDA system and the cw-seed light has been analyzed through established techniques [95], adding $6 \times 10^{-4} \text{ cm}^{-1}$ to the frequency uncertainties. For the latter two contributions a multiplication by a factor of four is included, for the frequency doubling and the two-photon process. The Doppler-free two-photon excitation with counter-propagating beams, enforced by the Sagnac interferometric alignment [166], constrains the uncertainty from a residual Doppler effect below $1 \times 10^{-4} \text{ cm}^{-1}$. Since the ion optics are triggered at least 80 ns delayed from the spectroscopy laser a dc-field-free environment is created, giving rise to a negligible dc-Stark effect to the accuracy.

The spectral recordings of the Doppler-free REMPI spectra undergo strong ac-Stark effects that contribute to the measurement uncertainty in two ways:

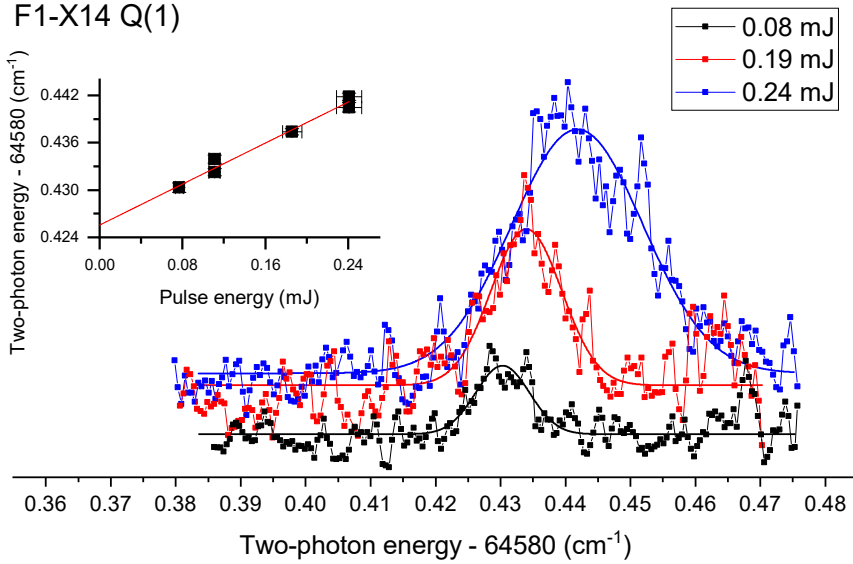


Figure 5.6: Spectra of the F1 - X14 Q(1) transition; details as in Fig. 5.4.

asymmetric line profiles and shift of line center. The tightly focused PDA beams induce asymmetry of the line profile which limits the determination of line center. The spectra are fitted with Gaussian and skewed Gaussian profile to account for this line profile asymmetry. The uncertainty estimated from the extrapolation to zero-power yields 0.0005 cm^{-1} . For the low-power spectrum of the F0-X13 Q(3) line, with 0.03 mJ UV pulse energy, the line width is symmetric and about 180 MHz (FWHM), close to the expected instrumental linewidth determined by the laser bandwidth. For higher UV pulse energies, the spectral profiles become broadened and show a significant degree of asymmetry as result of spatial distribution of ac-Stark shifts in a tightly focused beam [140]. These lines are fitted with skewed Voigt profiles to determine the transition frequencies, as discussed previously [84]. The field-free transition frequencies are determined by extrapolation to zero power levels as shown in the insets of the figures.

The overall uncertainty results in 0.0024 cm^{-1} , corresponding to 70 MHz, by summing in quadrature for the F0-X13 Q-branch. For the F1-X14 Q(1) line 0.0040 cm^{-1} uncertainty is estimated, in view of the larger statistical uncertainty as a result of the poor signal-to-noise ratio obtained. Transition frequencies determined for the observed F0-X13 Q(J) and F1-X14 Q(1) lines,

5. PHOTOLYSIS PRODUCTION AND SPECTROSCOPIC INVESTIGATION OF THE HIGHEST VIBRATIONAL STATES IN H_2 ($X^1\Sigma_g^+$ $v = 13, 14$)

Table 5.1: Error budget for the two-photon frequencies for F0-X13 Q(J).

Contribution	Uncertainty ($\times 10^{-3} \text{ cm}^{-1}$)
Line profile (fitting)	0.5
Statistics	2
AC-Stark extrapolation	1
Frequency calibration	0.3
Cw-pulse offset (chirp)	0.6
Residual Doppler	< 0.1
DC-Stark effect	< 0.1
Total	2.4

and the uncertainties, are listed in Table 5.2.

5.4 Discussion

The dissociation of H_2S in the present study is performed via two-photon absorption at 281.8 nm instead of 291.5 nm as was used in the previous studies [84, 85], where the highest level observed in H_2 ($X^1\Sigma_g^+$) was $v = 12, J = 5$. The energy required for complete dissociation of ground state H_2S into an $\text{S}(^1\text{D}_2)$ atom and two H atoms is about $69935(25) \text{ cm}^{-1}$ [81]. The corresponding two-photon energy at 291.5 nm would reach only to about 1300 cm^{-1} below the H_2 dissociation limit, insufficient to produce H_2 fragments in $v = 13$ and $v = 14$. A 2+1 REMPI spectrum of H_2S shows a resonance at 281.8 nm, and when fixing the dissociation laser wavelength to this resonance at 281.8 nm the energetic region of 1000 cm^{-1} above the dissociation limit of H_2 can be probed and $v = 13, 14$ produced. The signal strength for odd- J transitions is generally stronger than for even- J transitions, reflecting the ortho-para distribution which is apparently maintained in the photolysis process. However, the signal intensity depends also on the efficiency of the autoionization induced by the setting of the third UV-laser.

Table 5.2: Measured frequencies for the two-photon F-X transitions probing the highly excited vibrational levels $X^1\Sigma_g^+$, $v = 13, 14$, with uncertainties indicated in parentheses. These experimental values are compared with predicted values obtained via the combination of computed results for $X^1\Sigma_g^+$ [52, 177] and experimental values for $F^1\Sigma_g^+$ [171]. The value for the F0 $J = 7$ level is absent in Ref. [171]. The uncertainties in the experimental F-state level energies were reevaluated from the data reported in the Supplementary Material of Ref. [171] and listed under δF_{exp} . Similarly the uncertainties in the calculated values of the X-levels, as determined from the H2SPECTRE program [177] are listed under δX_{theo} . All values in cm^{-1} .

	Exp.	δF_{exp}	δX_{theo}	Predicted	Diff.	
F0-X13	Q(1)	63 993.7920 (24)	0.004	0.0035	63 993.7956 (53)	-0.0036 (58)
	Q(2)	63 957.5160 (24)	0.002	0.0034	63 957.5236 (39)	-0.0076 (46)
	Q(3)	63 905.9305 (24)	0.010	0.0033	63 905.9369 (105)	-0.0064 (108)
Q(5)	Q(5)	63 771.9836 (24)	0.015	0.0028	63 771.9723 (152)	+0.0113 (154)
	Q(7)	63 637.7937 (24)		0.0021		
F1-X14	Q(1)	64 580.4274 (40)	0.009	0.0017	64 580.4096 (92)	+0.0178 (95)

Table 5.3: Combination difference with measured F0-X11 transitions in Ref. [84] and comparison with calculations in the ground electronic state. All values are presented in cm^{-1} , with uncertainties indicated in parentheses.

	F0-X13	F0-X11	X13-X11	Calculation	Difference
Q(1)	63 993.7920 (24)	66 438.2920 (15)	2 444.5000 (28)	2 444.5019 (53)	-0.0019 (60)
Q(3)	63 905.9305 (24)	66 250.6874 (15)	2 344.7569 (28)	2 344.7489 (52)	+0.0080(59)
Q(5)	63 771.9836 (24)	65 931.3315 (15)	2 159.3479 (28)	2 159.3459 (51)	+0.0021(58)
Q(7)	63 637.7937 (24)	65 510.6124 (20)	1 872.8187 (31)	1 872.8277 (48)	-0.0090 (57)

5. PHOTOLYSIS PRODUCTION AND SPECTROSCOPIC INVESTIGATION OF THE HIGHEST VIBRATIONAL STATES IN H₂ (X¹Σ_g⁺ v = 13, 14)

In Table 5.2 a comparison is made between measured transition frequencies and predicted frequencies extracted from the calculated binding energies of X¹Σ_g⁺(v = 13) levels [52, 177] and F¹Σ_g⁺-state level energies obtained from Fourier-Transform (FT) spectroscopic measurements [171]. The uncertainty of the X¹Σ_g⁺ state binding energies as obtained from the H2SPECTRE program suit [177] amounts nominally to 0.002 - 0.003 cm⁻¹ with computed values listed in Table 5.2. For the experimentally determined level energies of F0, obtained up to J = 5 only, we have reanalyzed the uncertainties, based on the data presented in the Supplementary Material of Ref. [171], because precision studies on the GK-X transition in H₂ [51] have shown that some levels in Ref. [171] exhibit a somewhat larger uncertainty than previously estimated. The reevaluated uncertainties are listed in Table 5.2. This comparison leads to fair agreement.

In order to test the full QED-relativistic calculations of the ground state binding energies, a further comparison is made using combination differences from experiment, independent of data on F-level energies from Ref. [171]. The previous experimental values on F0-X11 Q-transitions [84] are subtracted from the present values for F0-X13 Q-transitions to obtain vibrational intervals between X13 and X11 levels which can be compared with the same combination differences from the most advanced first principles calculations [52, 177]. Table 5.3 presents these comparisons for four sets of J-levels. The experimentally derived intervals between v = 11 and v = 13 agree with the calculations at a root-mean-square value of ±1.07σ.

These result provide a test on the accuracy of the *ab initio* computations for ground state levels, for the first time for the highest v-levels in the X¹Σ_g⁺ ground state of H₂. The current theoretical values are limited by non-adiabatic contributions to the relativistic energy [52]. Meanwhile, improved fully variational calculations have been developed, that led to an uncertainty less than 10⁻⁷ cm⁻¹, but as of yet only for the X¹Σ_g⁺ (v = 0, J = 0) ground state [22].

As for the F1-X14 Q(1) line no such comparison could be made, because the F1-X13 and F1-X12 Q(1) transitions appeared too weak in the high precision measurement. In the search of v = 14 in H₂, excitations to F0, F1 and F2 states were tested but only a single F1-X14 Q(1) line is confirmed. The absence of F0-X14 lines could be explained by the small Franck-Condon factor, which is about 70-times smaller than that for F1-X14 [191]. The assignment of F1-X14 Q(1) is verified by comparing autoionization spectra recorded in the region below the X⁺(v⁺ = 4, J⁺ = 1) ionization threshold as shown in Fig. 5.7. The F-outer-well state has nominally (2pσ_u)² character and we observe exclusively transitions to vibrationally autoionizing (1sσ)(npσ/π) Rydberg states, with n being the principal quantum number. To guide the assignment we carried out multichannel quantum-defect (MQDT) calculations as described in Ref. [192] using the quantum-defect functions derived in Ref. [193]. We

note that states with Σ^+ and Π^+ symmetry are subject to predissociation into the $\text{H} + \text{H}(n = 2)$ continuum, leading to broad resonances especially for low n -values. The interaction with the dissociation continuum was not included in our calculation, leading to deviations of the calculated term values for the low- n resonances on the order of 1 cm^{-1} . The experimental line positions for these states are however in good agreement with previously reported values and MQDT calculations including the combined ionization and dissociation continuum [194–196].

Autoionization spectra are recorded by fixing the PDA-spectroscopy laser on two-photon resonances probing F0 $J = 1$, F0 $J = 3$ and F1 $J = 1$, and are plotted on an energy scale relative to the X, $v = 0, J = 0$ state of H_2 . The fact that the autoionization spectrum from F0 $J = 1$, probed via X13 $J = 1$, exhibits the same resonances as the autoionization spectrum from F1 $J = 1$, probed via X14 $J = 1$, proves that the two-photon resonance at $64\,580.427 \text{ cm}^{-1}$ starts from a $J = 1$ line, which leads to an unambiguous assignment of the F1-X14 Q(1) transition. Unfortunately no other rotational levels in X14 could be found. There appears a strong transition at $64\,563.084 \text{ cm}^{-1}$, while the expected F1-X14 Q(3) is at $64\,562.883 \text{ cm}^{-1}$, exhibiting a 0.201 cm^{-1} difference. Also in this case an autoionization spectrum is recorded from this intermediate state, but that does not match with an autoionization spectrum from F0 $J = 3$. Hence the assignment of the F1-X14 Q(3) line is discarded.

As a byproduct of the present study the Stark slopes of the two-photon transitions are determined, results of which are shown in the insets of Figs. 5.4–5.6. Those represent the shift of line center as a result of the ac-Stark effect, i.e. the power density; a negative Stark slope corresponds to a red-shift of the lines for higher power densities. Stark slopes for the F0-X13 band are all negative, while that of the single transition in the F1-X14 band is found positive. In a previous study a negative Stark slope was found for lines in the F0-X11 band, where a very small J -dependent value was found for the F3-X12 band [84]. Similarly, in two-photon excitation to the inner well positive Stark slopes were found for the E0-X0 band [100] and the E0-X1 band [105]. These Stark slopes depend on the transition dipole moments in summation over all states in the molecule [197, 198] thus providing information on the quantum structure of the molecule, analysis of which is beyond the scope of this study.

5. PHOTOLYSIS PRODUCTION AND SPECTROSCOPIC INVESTIGATION OF THE HIGHEST VIBRATIONAL STATES IN H_2 ($X^1\Sigma_g^+$ $v = 13, 14$)

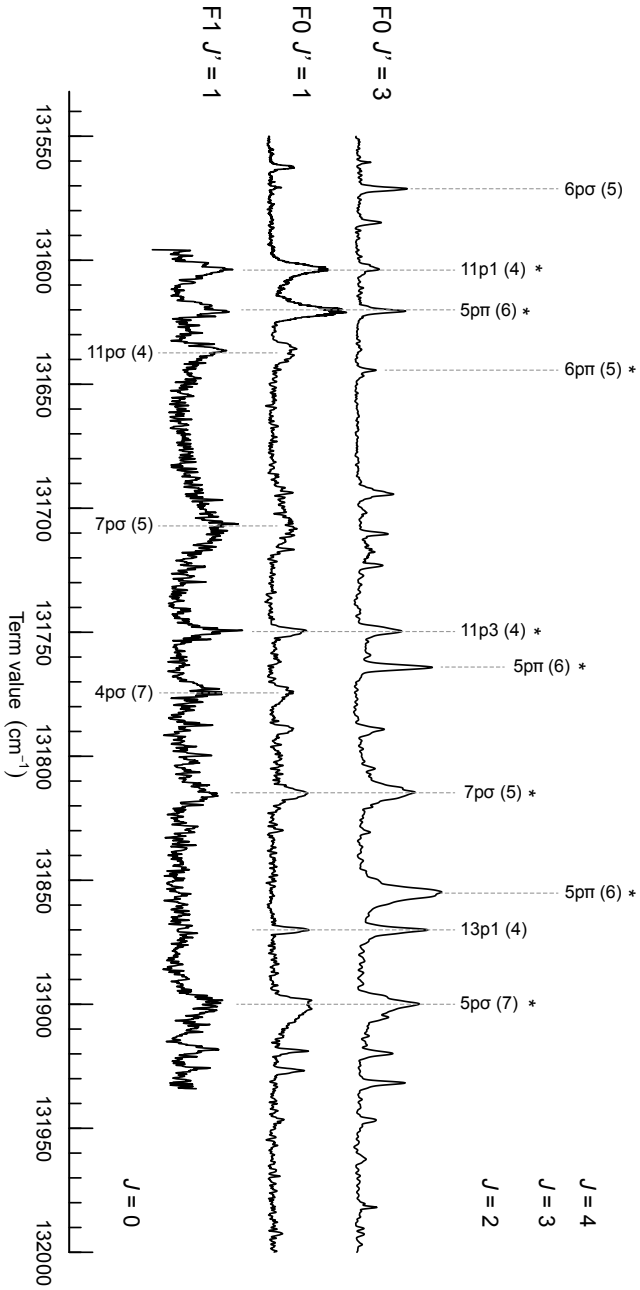


Figure 5.7: Autoionization spectra from $F0 J' = 1$, $F1 J' = 1$ and $F0 J' = 3$ intermediate levels. The horizontal axis reflects the total term value by adding the UV two-photon energy and the F-state level energy from Ref. [171]: 98376.0474 cm^{-1} for $F0 J = 1$, 100570.843 cm^{-1} for $F1 J = 1$ and 99437.1665 cm^{-1} for $F0 J = 3$. The resonances in the autoionization continuum are labeled in either Hund's case b) - $mp\lambda(v^+)$ - or d) - $mpN^+(v^+)$ -, where v^+ and N^+ are the vibrational and the rotational quantum numbers of the H_2^+ ion core. The total angular momentum quantum number J of the H_2 continuum resonance is given on the right. Previously observed resonances [194–196] are indicated by an asterisk.

5.5 Conclusion

In the present study two-photon UV-photolysis of H_2S was pursued, probing a two-photon absorption resonance at 281.8 nm, hence at sufficiently short wavelength to produce H_2 molecules in the highest vibrational levels: $v = 13, 14$. The transition energies of F-X (0,13) Q-branch lines have been measured at an accuracy of 0.0024 cm^{-1} . In comparing these results with previous measurements on F0-X11 Q-lines the experimental combination difference can be used to verify level intervals as computed with advanced quantum chemical calculations of the ground electronic state of H_2 , including non-adiabatic, relativistic and QED effects. This results in good agreement. Also the highest vibrational state $v = 14$ of H_2 has been produced through the two-photon photodissociation of H_2S . Only a single rotational level $J = 1$ could be observed. The assignment of this $X^1\Sigma_g^+$ ($v = 14, J = 1$) level was verified by recording and comparing autoionization spectra from various F-outer well states.

The total uncertainty in the present study is limited by measurement statistics, associated with the low concentration of H_2 fragments produced, and by strong ac-Stark effects resulting from the focused UV-laser beams required to obtain signal. Further improvement of the H_2S photolysis production process is critical for pursuing higher measurement accuracy. Under such improved conditions the entire rotational manifold $J = 0 - 3$ of bound levels in $v = 14$ might be probed and studied and implemented in QED-test of such weakly bound states at large internuclear separation. It has been a matter of debate whether the final level $J = 4$ is rotationally predissociative [199], only bound by non-adiabatic effects [41], or quasi-bound due to hyperfine effects [200]. As an outlook it may be hypothesized that also quasi-bound states in H_2 might be observed by the methods pursued here.

Acknowledgement

The authors thank Dr. Christian Jungen for fruitful discussions and for making available his MQDT-codes for calculating and assigning the autoionization resonances. WU acknowledges the European Research Council for an ERC Advanced grant (No: 670168).

Shape resonances in H₂ as photolysis reaction intermediates

Abstract

Shape resonances in H₂, produced as reaction intermediates in the photolysis of H₂S precursor molecules, are measured in a half-collision approach. Before desintegrating into two ground state H atoms, the reaction is quenched by two-photon Doppler-free excitation to the F electronically excited state of H₂. For $J = 13, 15, 17, 19$ and 21, resonances with lifetimes in the range of nano to milliseconds were observed with an accuracy of 30 MHz (1.4 mK). The experimental resonance positions are found to be in excellent agreement with theoretical predictions when non-adiabatic and quantum electrodynamical corrections are included. This is the first time such effects are observed in collisions between neutral atoms. From the potential energy curve of the H₂ molecule, now tested at high accuracy over a wide range of internuclear separations, the s-wave scattering length for singlet H(1s)+H(1s) scattering is determined at $a = 0.2735_{31}^{39} a_0$.

This chapter is reproduction of: Lai, K.-F.; and Salumbides, E. J.; Ubachs, W.; Beyer, M. Shape Resonances in H₂ as Photolysis Reaction Intermediates. *Phys. Rev. Lett.* **2021**, 127, 183001

6.1 Introduction

The understanding of resonance phenomena occurring in the encounter of colliding particles is of eminent importance in physics. As was first discovered by Fermi and co-workers [201], particles colliding in a partial wave with non-zero rotational angular momentum can be trapped behind a potential barrier - a phenomenon known as *shape resonances* [202]. These quasi-bound states are rare and occur incidentally through an interplay between the specific shape of a molecular potential and the centrifugal barrier $J(J+1)/2\mu R^2$, for a given partial wave J and colliding particles with reduced mass μ . A second manifestation of collision resonances, called *Feshbach resonances*, have attracted great attention in the field of ultracold atoms in the last decade [203–205]. Here the resonance occurs by coupling the continuum of one scattering channel to a bound molecular state from a different channel. This coupling can be the result of an intrinsic property of the molecule, like Coriolis interactions [206], or it can be caused by external magnetic [207] or electric [208] fields.

Magnetic Feshbach resonances play an important role in the study of cold interacting Bose and Fermi gases, but experimental studies have been mainly limited to s-wave resonances. Recently, resonances for higher partial waves $J \neq 0$ have been observed [209–211], which must be characterized as of mixed Feshbach/shape resonance character. A detailed understanding of higher partial wave magnetic Feshbach resonances requires therefore a good understanding of shape resonances [212].

Most Feshbach resonances have been observed using laser-coolable alkaline or earth-alkaline atoms, for which potential energy curves can be calculated to high accuracy, although in a phenomenological manner involving fitting of parameters [213, 214]. The H+H collision system stands out representing the interaction between the simplest atomic constituents, which allows the comparison of experimental results with full-fledged *ab initio* calculations. The H(1s) + H(1s) scattering is of fundamental interest in physics, playing a role in the formation of molecular hydrogen in the universe [215], frequency shifts in the hydrogen maser [216], in the precision metrology of atomic hydrogen and the determination of the Rydberg constant [217], and for the formation of hydrogen Bose-Einstein condensates [218]. The light mass of the hydrogen atom compared to all other studied systems, makes this collision uniquely sensitive to nonadiabatic effects, i.e., the effects of distant electronic states on a given collision channel [219].

We present in this letter the study of shape resonances in the collision of two ground state hydrogen atoms at an accuracy 10^{-5} relative to the collision energy. Five very narrow shape resonances with $J = 13, 15, 17, 19$ and 21 , with predicted lifetimes varying from ns to ms [72], have been observed at a precision high enough to identify for the first time nonadiabatic, as well as relativistic and

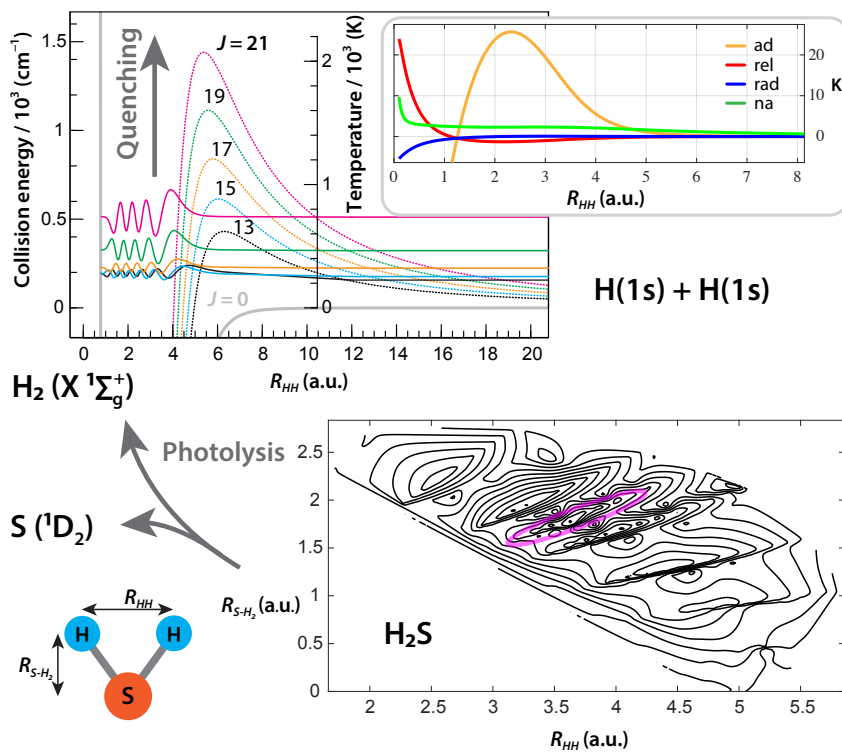


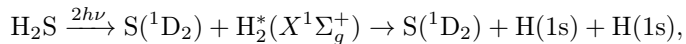
Figure 6.1: Potential energy surfaces for the electronic ground states of H_2S [220] and H_2 [22]. The H_2S equilibrium geometry is indicated with a magenta ellipse in the contour plot. For H_2 the radial wave functions (not to scale) of the observed shape resonances and the respective rotational barriers are shown. The inset displays the J -independent contribution of beyond-Born-Oppenheimer contributions to the potential.

QED effects in neutral atom-atom collisions. Previously nonadiabatic effects have been observed in the shape resonances of the ion-neutral H+H⁺ collision at a hundred times lower precision [186, 187].

6.2 Experiment

Being inaccessible to laser cooling with standard techniques, the study of controlled H+H collisions could take place in atomic beam scattering experiments or using a half-collision approach, i.e., by photodissociating molecular hydrogen. Given the narrow width of the resonances (50 nK–5 mK), the former seems unrealistic, whereas for the later only collisions between ground and excited H atoms could be probed [221].

Instead, we choose to photolyse hydrogen sulfide molecules at 281.8 nm, providing sufficient energy for a complete three particle dissociation [81, 82], according to:



to produce quasi-bound H₂^{*} molecules, existing as an intermediate reaction product before desintegrating into two H(1s) atoms. The reaction is interrupted - quenched - by probing the long-lived shape resonances H₂^{*} via two-photon Doppler-free excitation into the F¹Σ_g⁺, *v* = 0 electronically excited outer well of the EF state (denoted as F0 in the following). A third UV laser pulse probes the F0 population by photoionization and the resulting H₂⁺ ions are detected selectively using a multichannel plate detector after passing a time-of-flight mass separator. The latter distinguishes the weak H₂⁺ signals from rather strong H₂S⁺, SH⁺, S⁺ and H⁺ background signals. A more detailed description of the experimental setup and the narrow-band pulsed dye amplifier (PDA) laser is given in Ref. [222]. Calibrating the laser light using a wavemeter and accounting for frequency chirp induced by the amplifier, allows to reach an absolute accuracy of a few tens of MHz, corresponding to around 1 mK.

The H₂S [220] and H₂ [22] potential energy surfaces, displayed in Fig. 6.1, illustrate the excitation of the shape resonances. The mean distance between the protons in the equilibrium geometry of H₂S (indicated by a magenta ellipse) is comparable to the outer turning point of the H₂ potential, where the H₂^{*} radial wave functions have their largest amplitude, allowing an efficient production of the resonances in the spirit of the Franck-Condon principle. The radial wavefunctions of the shape resonances are depicted together with the respective centrifugal barriers, necessary for their formation. Centrifugal barriers with a height of a few hundred up to two thousand Kelvin are found for *J* = 15 – 21, resulting in a strongly reduced tunneling probability and a tiny amplitude of the radial wave function for large internuclear distance *R* (behind the barrier).

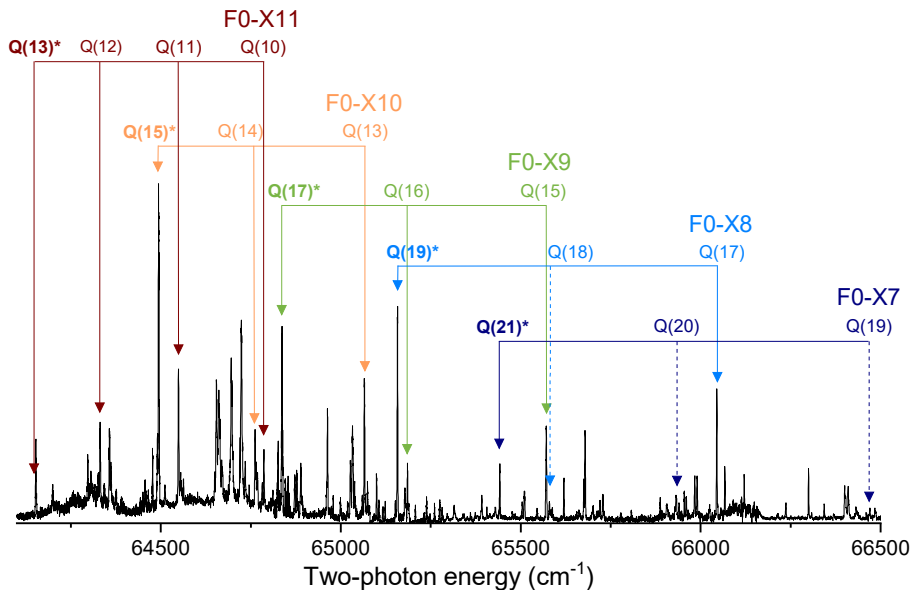


Figure 6.2: Overview spectra recorded in a two-laser scheme with two-photon UV-photolysis of H_2S , followed by 2+1 REMPI on $\text{F0-X}(v'')$ bands with a UV-tunable frequency-doubled dye laser. Transitions are labeled with quantum numbers of the ground level. Excitations from quasi-bound resonances are indicated with asterisk (*).

The contribution of the leading terms that go beyond the Born-Oppenheimer approximation - adiabatic, relativistic, radiative and nonadiabatic corrections - are depicted in the inset.

The product distribution of rovibrationally excited states H_2^* was measured in a two-color overview scan in the wavelength range 300 – 310 nm (plotted in Fig. 6.2) showing a forest of spectral lines in (v', v'') vibrational bands of the $\text{F}^1\Sigma_g^+ - \text{X}^1\Sigma_g^+$ system, detected via 2+1 resonance-enhanced multiphoton ionization. In this dense overview spectrum progressions of $\text{O}(\Delta J = -2)$, $\text{Q}(\Delta J = 0)$ and $\text{S}(\Delta J = 2)$ rotational branches in the various bands are detected. The assignment of the bound states in Fig. 6.2, and in particular of the shape resonances is based on a comparison with calculated values of the transition frequencies.

6.3 Theory

For this purpose highly accurate calculations of $X(v, J)$ levels were performed using the nonrelativistic quantum electrodynamics (NRQED) approach, in which relativistic, leading-order radiative and higher order QED corrections are added to a nonrelativistic Hamiltonian:

$$E(\alpha) = m_e \alpha^2 E^{(2)} + m_e \alpha^4 E^{(4)} + m_e \alpha^5 E^{(5)} \dots \quad (6.1)$$

The nonrelativistic energies $E^{(2)}$ are evaluated using non-adiabatic perturbation theory (NAPT) [52] accounting for terms up to $m_e \alpha^2 (m_e/m_p)^2$, while maintaining the computational efficiency of the Born-Oppenheimer (BO) approach through separating the electronic and nuclear Schrödinger equation. This is achieved by including R -dependent corrections to the potential energy curve and by employing R -dependent reduced masses in the nuclear Schrödinger equation $\mu_{\parallel}(R)$ and $\mu_{\perp}(R)$ defined in [22]. The radial nuclear Schrödinger equation (in atomic units) within NAPT is given by [22]

$$\left[-\frac{1}{R^2} \frac{\partial}{\partial R} \frac{R^2}{2\mu_{\parallel}(R)} \frac{\partial}{\partial R} + \frac{J(J+1)}{2\mu_{\perp}(R)R^2} + \mathcal{V}(R) \right] \phi_i(R) = E_i \phi_i(R). \quad (6.2)$$

Applying the ansatz $\chi_i(R) = R\phi_i(R) \exp\{-Z(R)\}$ to remove the first-order radial derivative [200, 223], the Schrödinger equation can be numerically solved using $\mathcal{V}(R) = \mathcal{E}_{\text{BO}} + \mathcal{E}_{\text{ad}} + \delta\mathcal{E}_{\text{na}}$, being the BO [15], adiabatic [16] and non-adiabatic [17] potential energy curve, respectively. Relativistic ($m_e \alpha^4$) and QED ($m_e \alpha^5$, $m_e \alpha^6$) corrections are included in the computation as described in Ref. [22]. The inset in Fig. 6.1 displays these corrections and illustrates their size compared to the BO energies.

We add an extension to the NAPT framework to calculate the positions and widths of the shape resonances using the time-delay matrix technique [224], with the phase shift η_J obtained for a given J by propagating the wave function to large internuclear distance, where $\lim_{R \rightarrow \infty} Z(R) = 0$, so that standard scattering boundary conditions can be applied.

The present numerical calculation reaches an accuracy on the order of 0.003 cm^{-1} for bound states and resonances, with the uncertainty originating mainly from terms proportional to $m_e \alpha^2 (m_e/m_p)^3$ that were neglected in the current NAPT approach. Exact agreement with the results of the H2SPECTRE program suite [177] was obtained for the bound levels and the resonance positions were found in agreement with previously calculated collision energies [72], although the present values are more accurate by a factor of 30. The resonance lifetimes are computed resulting in values ranging from 0.2 ms for $X(7,21)^*$ to 2 ns for $X(11,13)^*$.

Fig. 6.3 illustrates the non-adiabatic and leading-order relativistic and radiative contributions to the $\text{H}_2(v, J)$ dissociation energies for bound states and for the observed shape resonances with $J = 0 - 21$. It is evident, that nonadiabatic interactions affect mainly states with $v = 7 - 11$, as these states possess the largest vibrational kinetic energy [219], with the maximum reached for $v = 9$. The corrections of up to more than 100 GHz on the dissociation energies are positive, i.e., leading to larger dissociation energies, as it would be expected from interactions with distant states at higher energy. The calculations of the relativistic correction ($m_e\alpha^4$) on the order of several GHz reveal an increased sensitivity for levels with low v and high J , as was tested in Ref. [225]. Computations for the leading-order QED-corrections $m_e\alpha^5$ (also depicted in Fig. 6.3) show a larger sensitivity for levels with low v and low J and contribute on the order of 100 MHz to the resonance energies.

This suggests that narrow shape resonances are observed for a vibrational excitation that constitutes a precisely tailored test case for non-adiabatic effects in atomic collisions. As an example, the position of the $\text{X}(7,21)^*$ resonance is shifted by ~ 10 K, ~ 6 K, ~ 0.7 K and ~ 11 mK by the adiabatic, non-adiabatic, relativistic and radiative correction, respectively (see also the inset of Fig. 6.1; it should be noted that the non-adiabatic correction results mainly from the R -dependent reduced mass).

F0-level energies were obtained by solving the Schrödinger equation using Born-Oppenheimer [226], adiabatic [227] and relativistic [14] potential energy curves, while including leading-order radiative corrections taken from Ref. [228] for the hydrogen molecular ion and estimating the effects of nonadiabaticity based on Ref. [181]. The computations for the $\text{F0}(J)$ level energies yield values accurate to $\sim 1 \text{ cm}^{-1}$, which is sufficient to identify the lines in Fig. 6.2 and to prove the quasi-bound nature of the resonances. The assignments are verified by the calculation of Franck-Condon factors (FCF) in the F-X system. The shifting of the wave function of the H_2^* shape resonances towards larger internuclear separation causes the favorable condition of enhanced FCF, giving increased intensities for those lines probing H_2^* , as is experimentally observed (see Fig. 6.2).

6.4 Results and Discussions

Subsequently the shape resonances $X(v, J)$: (7,21), (8,19), (9,17), (10,15) and (11,13) are probed in a precision measurement, with the narrowband PDA-laser detecting the Doppler-free $\text{F}^1\Sigma_g^+ - \text{X}^1\Sigma_g^+$ two-photon transition. In Fig. 6.4 an example of a line probing $\text{X}(10,15)$ via a Q-line is presented. These precision measurements are performed for varying intensities allowing for assessment of the AC-Stark effect in extrapolation to zero field as shown. All five quasi-

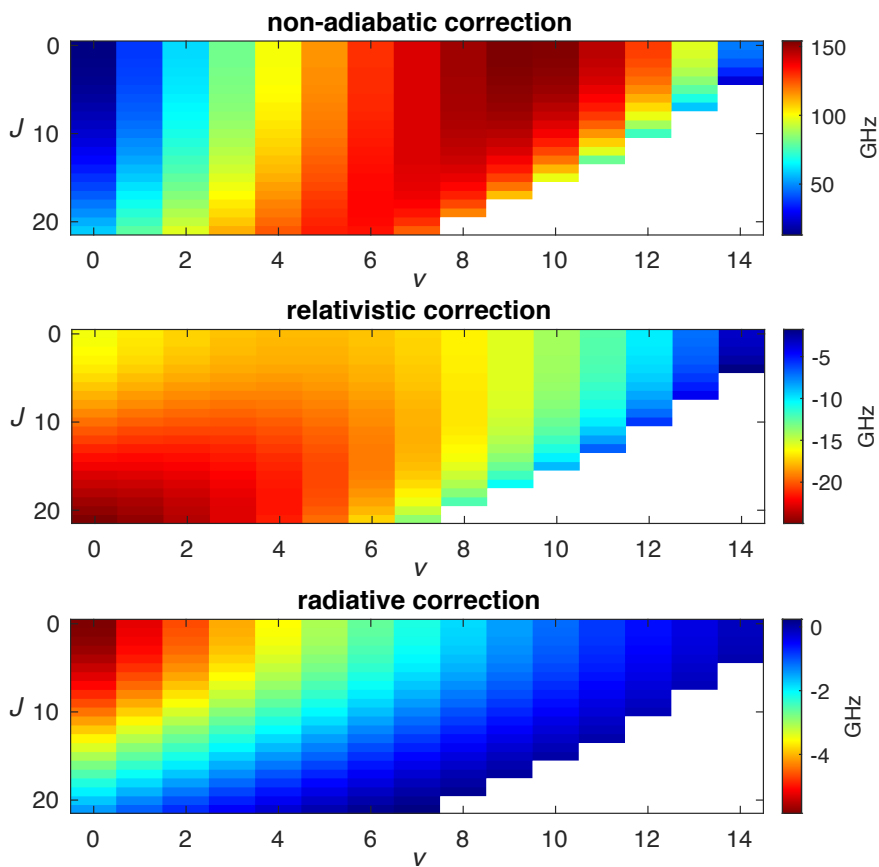


Figure 6.3: Color-map displaying the magnitude of contributions to the energies of (v, J) levels in H_2 , for both bound and quasi-bound levels, resulting from non-adiabatic, relativistic and radiative corrections to the BO-energies.

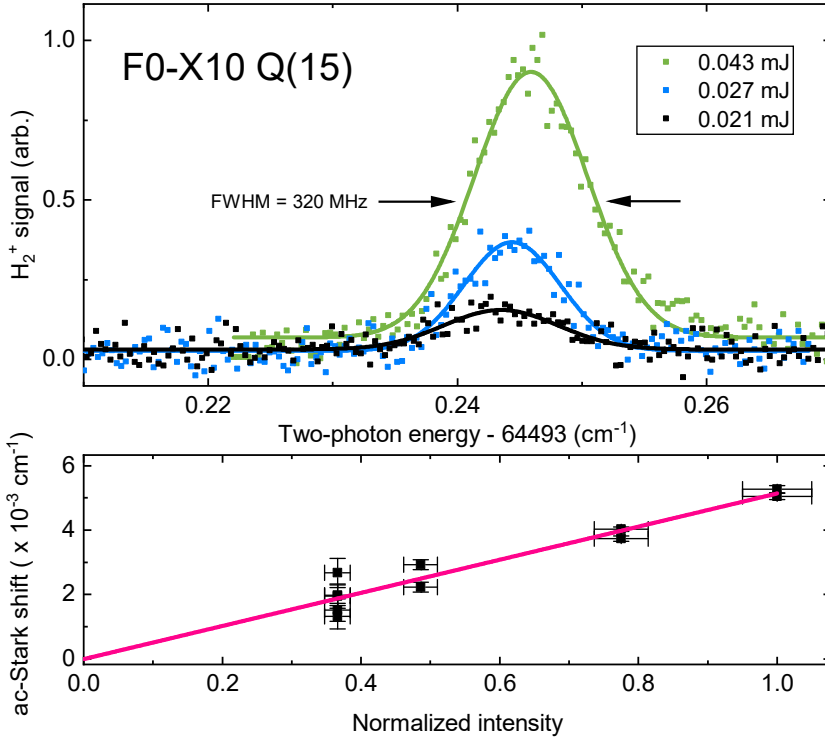


Figure 6.4: High-resolution excitation spectrum of a two-photon transition in the F-X system probing the shape resonance (10,15) via a Q-line. The lower panel shows the AC-Stark extrapolation to deduce the field-free transition frequency.

bound states have been excited via a Q-transition ($\Delta J = 0$), while some are also probed via an S- or O-transitions. The extrapolated zero-intensity values of the highly accurate transition frequencies are compiled in Table 6.1. Also some transitions from bound states are subjected to a precision measurement. Averaging over multiple measurement sequences yields an optimum uncertainty of $0.001 cm^{-1}$, while it is $0.002 cm^{-1}$ for somewhat weaker transitions (30 and 60 MHz, respectively); for a detailed error budget see Supplemental Material. The uncertainty is larger for the short-lived $H_2^*(11,13)$ resonance.

Although the transition frequencies probing the quasi-bound resonances were measured at high accuracy, this does not provide a direct means to determine collision energies. In order to make a comparison with theory possible, combination differences between resonances and bound states have been com-

Table 6.1: Measured frequencies for the two-photon F0-X transitions probing the quasi-bound levels H₂^{*}(X), with uncertainties indicated in parentheses. Also some transitions from bound H₂(X) levels are included.

H ₂ [*] (X)	Line	Exp. (cm ⁻¹)	Line	Exp. (cm ⁻¹)
(7,21)*	Q(21)	65 441.3575 (9)	O(21)	64 979.430 (10)
(8,19)*	Q(19)	65 157.9413 (21)	O(19)	64 734.8098 (9)
(8,19)*	S(19)	65 619.8599 (8)		
(9,17)*	Q(17)	64 837.2974 (19)	O(17)	64 454.775 (10)
(10,15)*	Q(15)	64 493.2404 (9)	O(15)	64 152.970 (20)
(11,13)*	Q(13)	64 146.930 (20)		
(8,17)	Q(17)	66 044.7046 (9)		
(9,15)	Q(15)	65 571.9063 (19)	S(15)	65 954.4505 (10)

Table 6.2: Comparison of experimental and calculated collision energies E_{Col} of observed shape resonances, and some bound states. Energy intervals with respect to X(10,15)* are determined from combination difference and shifted by the calculated dissociation energy of 186.4542(36) cm⁻¹ to give E_{Col} . Parentheses present the relative uncertainty to the X(10,15)* resonance. All values in cm⁻¹.

(v, J)	$E_{\text{Col}}^{\text{exp}}$	$E_{\text{Col}}^{\text{calc}}$	ΔE_{Col}
(7,21)*	505.9314 (28)	505.9310 (9)	0.0004 (29)
(8,19)*	327.4290 (25)	327.4291 (7)	-0.0001 (26)
(9,17)*	224.9414 (30)	224.9410(4)	0.0004 (30)
(10,15)*	186.4542	186.4542	0
(11,13)*	192.495 (28)	192.4945(6)	0.001 (28)
(9,15)	-892.2117 (21)	-892.2130(11)	0.0013 (24)
(8,17)	-982.4658 (25)	-982.4659 (12)	0.0001 (28)

puted with the results presented in Table 6.2. The X(10,15)* level was chosen as an anchor level and the collision energy was set to coincide with its theoretical value. Intervals can be calculated at higher accuracy than dissociation energies of single levels, because the neglected terms in the NAPT approach lead to an approximately equal shift of the X levels caused by the far distant states. Table 6.2 demonstrates that the deviations between experimental and computed combination differences are well within 0.001 cm^{-1} (30 MHz). This high level of agreement constitutes a test of the calculations of the potential energy curve, including all adiabatic, non-adiabatic, relativistic and QED contributions. It tests the H_2 potential specifically at large internuclear distances and for the non-adiabatic corrections. This importantly complements previous precision tests that probe the bottom and deeper part of the $\text{H}_2(\text{X})$ potential well in experiments on vibrational intervals in H_2 [33, 34, 67] and on the dissociation energy $D_0(\text{H}_2)$ [51, 69].

As was noticed in Ref. [229], a precise measurement of shape resonances can also be used to determine the scattering length. We used the H_2 potential energy curve, now tested experimentally over a wide range of energies (including the continuum) and internuclear distances, to determine the singlet scattering length for the $\text{H}(1s) + \text{H}(1s)$ collision. Because of the importance of non-adiabatic effects in this collision, different approaches for their treatment were vividly discussed in the literature [230]. Whereas previously reported scattering lengths obtained by different authors within the BO and adiabatic approximations were found to agree, the values for the non-adiabatic scattering length varied between $0.3006 a_0$ and $0.564 a_0$ (see Table 3 in Ref. [230] and references therein), depending on the used reduced masses and effective correction potentials employed to account for the non-adiabatic interactions. Using the novel techniques presented here, which allow to include BO, adiabatic, non-adiabatic, relativistic and QED contributions up to $m_e \alpha^6$, we obtain a scattering length of $a = 0.2735_{31}^{39} a_0$.

Non-adiabatic effects might also play a role in collisions of heavier atoms or in collisions of light atoms and molecules [231]. In case no *ab initio* data is available, effects of this kind can be taken into account by using the atomic reduced mass when solving the radial Schrödinger equation. We found that such an approach leads to an error of 0.8% and 0.001% on the X(10,15)* and X(7,21)* resonance position, respectively. The scattering length found in this way deviates by 3%. Although the scaling with the reduced mass results in nonadiabatic effects being reduced, for example by a factor of six in $\text{Li} + \text{Li}$ collisions, the crude treatment of non-adiabatic effects using atomic reduced masses might lead to a very large disagreement given the experimental accuracy of typical cold atom experiments. As was pointed out in Ref. [232], accurate R -dependent reduced masses accounting for the bulk of nonadiabatic effects can be even obtained from relatively crude molecular wavefunctions. This should

allow testing the approach presented here for collisions involving heavier atoms with the currently reachable precision of ab initio calculations. Such precision studies uniquely straddle the interface between ultracold collisions in atomic physics and bond forming phenomena in chemistry.

Because of the long lifetime of the observed shape resonances, a measurement of their energy-level structure with kHz precision appears possible, which is interesting, given their low sensitivity to QED effects (see Fig. 3). This allows to specifically test the accuracy of relativistic four-body calculations, while avoiding the evaluation of QED effects, representing today the major source of theoretical uncertainty.

Acknowledgement

The authors thank Prof. Frederic Merkt (ETH Zürich) for discussions motivating this work. This work is financially supported by the European Research Council through an ERC Advanced grant (No: 670168). MB acknowledges NWO for a VENI grant (VI.Veni.202.140).

Supplemental Material

The error budget for the frequency calibrations, presented in Table 6.3, contains a variety of contributions. Minor contributions relate to the calibration uncertainty of the cw-laser seeding the pulse-dye amplifier, of some 2 MHz (at the fundamental), while a residual Doppler shift from misalignment of the counter-propagating beams is reduced by Sagnac interferometry to below 3 MHz uncertainty. The chirp-induced frequency correction accounts for another 4.5 MHz uncertainty. The AC-Stark effect yields the largest contribution to the error budget. It is addressed by performing systematic measurements resulting in the AC-Stark slopes as indicated in Fig. 6.4. The uncertainty associated with AC-Stark results from the extrapolation to zero-power levels and depends on the obtained signal-to-noise ratio for individual lines. In order to reduce the contributions of the AC-Stark effect various campaigns of re-measurement of the Stark-slopes were carried out, thus turning the systematic effect into a statistical distribution of results. For some weak transition, for example F0-X11 Q(13) and F0-X10 O(15), this could not be done effectively, and only measurements at high laser power were performed leading to larger uncertainties.

Table 6.3: Uncertainty budget for the measurements of two-photon F0-X transitions. The uncertainty for the AC-Stark extrapolations is estimated for individual transitions, where the total uncertainties are listed in Table 6.1.

Contribution	Uncertainty (MHz)
Lineshape fitting	15
Frequency calibration	9
CW-pulse offset (chirp)	18
Residual Doppler effect	3
DC-Stark effect	<1
Subtotal (exl. AC-Stark)	25
AC-Stark effect	3 – 60

Precision measurement of quasi-bound resonances in H₂ and the H + H scattering length

Abstract

Quasi-bound resonances of H₂ are produced via two-photon photolysis of H₂S molecules as reactive intermediates or transition states, and detected before decay of the parent molecule into three separate atoms. Four centrifugally bound quantum resonances with lifetimes of multiple μ s, lying energetically above the dissociation limit of the electronic ground state X¹ Σ_g^+ of H₂, were observed as X(*v*, *J*) = (7,21)*, (8,19)*, (9,17)*, and (10,15)*, while also the short-lived (~ 1.5 ns) quasi-bound resonance X(11,13)* was probed. The present paper gives a detailed account on the identification of the quasi-bound or shape resonances, based on laser detection via F¹ Σ_g^+ - X¹ Σ_g^+ two-photon transitions, and their strongly enhanced Franck-Condon factors due to the shifting of the wave function density to large internuclear separation. In addition, the assignment of the rotational quantum number is verified by subsequent multi-step laser excitation into autoionization continuum resonances. Existing frameworks of full-fledged *ab initio* computations for the bound region in H₂, including Born-Oppenheimer, adiabatic, non-adiabatic, relativistic and quantum-electrodynamic contributions, are extended into the energetic range above the dissociation energy. These comprehensive calculations are compared to the accurate measurements of energies of quasi-bound resonances, finding excellent agreement. They show that the quasi-bound states are in particular sensitive to non-adiabatic contributions to the potential energy. From the potential energy curve and the correction terms, now tested at high accuracy over a wide range of energies and internuclear separations, the s-wave scattering length for singlet H+H scattering is determined at $a = 0.2735_{31}^{39} a_0$. It is for the first time that such an accurate value for a scattering length is determined based on fully *ab initio* methods including effects of adiabatic, non-adiabatic, relativistic and QED with contributions up to $m\alpha^6$.

This chapter is reproduction of: Lai, K.-F.; Salumbides, E. J.; Beyer, M.; Ubachs, W. Precision Measurement of Quasi-Bound Resonances in H₂ and the H+H Scattering Length. *Molecular Physics* **2021**, No., e2018063

7.1 Introduction

Chemically bonded diatomic molecules in their ground electronic configuration typically support large but finite numbers of quantum levels, which are assigned with vibrational and rotational quantum numbers (v, J). These bound levels lie energetically below the dissociation threshold. Advanced calculations including non-adiabatic, relativistic and quantum-electrodynamical (QED) contributions for H₂ reveal that this simplest neutral molecule has 302 such bound states in its ground electronic configuration ($X^1\Sigma_g^+$) [117]. All these bound rovibrational states exhibit long lifetimes in excess of 10^5 s [93]. The computational methods for the determination of H₂ level energies witnessed great progress, starting with the wave-mechanical explanation that H₂ is a bound system by Heitler and London [233]. This evolved further to quantum-mechanical methods for the calculation of the dissociation energy of H₂, using two-centered wave functions by James and Coolidge [6] and the computations by Kolos and Roothaan [234], via the accurate computations including relativistic effects by Wolniewicz [12, 13], to the state-of-the-art approaches involving 4-particle variational calculations augmented with QED computations [21, 59, 112, 235, 236].

Progress on the theoretical side was matched by increasingly precise measurements of the dissociation energy of the smallest neutral molecule [25, 27–29, 51, 69, 237, 238], now finding agreement between theory and experiment at the level of 10^{-5} cm⁻¹. The computations were verified via comparison with measurements of high-rotational angular momentum states [225] and vibrational intervals in H₂ [32, 34, 67, 105, 239]. These improvements both on the experimental and theoretical side have made the hydrogen molecule into a test ground for investigating the effect of fifth forces [113], extra dimensions of space-time [115], and for probing physics beyond the Standard Model [116].

In addition to the large set of bound quantum states there exists a class of molecular resonances bound by a positive centrifugal barrier of size $\hbar^2 J(J+1)/2\mu R^2$ (with μ the reduced mass of the molecule and R the internuclear distance) added to the potential energy of the rotationless molecule. Such resonances lie energetically above the dissociation threshold giving rise to quasi-bound states that are prone to tunneling through this centrifugal barrier, a process known as rotational predissociation [240]. Such features were discussed in terms of a 'mechanical instability' of molecules after observation of the breaking off of a rotational progression in the ground state of the HgH molecule as early as 1929, at the dawn of molecular quantum spectroscopy [241]. In that study it was explained that there exist only a limited number of such centrifugally bound states; for increasing values of J the potential energy again becomes repulsive. A similar phenomenon was observed in the case of AlH [242]. Recently, the quasi-bound resonances in the hydrogen molecular ion were probed and accurately measured via multi-step laser spectroscopy, reveal-

ing the $X^+ 2\Sigma_g^+(v^+, J^+) = (18,4)^*$ resonance in para- H_2^+ , and the $X^+(17,7)^*$ resonance in ortho- H_2^+ [186, 243]. These resonances in the three-particle quantum system appeared to have lifetimes of 10 - 25 ps due to their rapid tunneling through the centrifugal barrier.

The quasi-bound states studied here have previously been observed and assigned by Dabrowski [74] and by Roncin and Launay [75] in emission spectra of the Lyman and Werner bands with optical transitions terminating on such resonances. Over the years computations were performed for such resonances in the hydrogen neutral molecule [72, 199, 200] and these indicate that some of the resonances are long-lived with lifetimes in excess of μs , and even up to few 100 μs . This makes these quasi-bound resonances amenable in precision experiments with lasers of narrow bandwidth.

The ultraviolet photolysis of H_2S has proven to be an ideal target system for the production of highly energetic rovibrational states in the electronic ground configuration of H_2 . In an explorative study, Steadman and Baer demonstrated the production of vibrationally-excited H_2 as a product channel from H_2S photodissociation [80]. They assigned transitions between high-vibrational states in H_2 to both inner and outer well states in the $EF^1\Sigma_g^+$ double well potential. However, in the controlled two and three-laser studies probing $X(v'' = 11 - 14)$ [83–85, 222] only transitions to the $F^1\Sigma_g^+$ outer well could be confirmed. In an alternative study, starting from the photolysis of H_2CO , therewith producing H_2 vibrational states of intermediate quantum numbers $X(v'' = 3 - 9)$, two-photon transitions to both $EF^1\Sigma_g^+$ inner and outer well were found [190]. Precision spectroscopic measurements probing the vibrational states just below the dissociation threshold allowed for tests of molecular *ab initio* calculations for these quantum states exhibiting wave function density at large internuclear separation [222].

The present study, of which a preliminary report was published previously [244], explores the energy range just above the dissociation threshold of H_2 upon two-photon UV-photolysis of hydrogen sulfide molecules. This results in the detection of quasi-bound states in H_2 , using 2+1' resonance-enhanced multi-photon ionization, and in the accurate determination of the excitation energies of the long-lived resonances. State-of-the-art quantum calculations developed for the bound region are extended to the region above threshold and compared with measured resonance energies. Hence, the experiments on quasi-bound resonances allow for testing the potential energy curve of the H_2 molecule for a wide range of internuclear separations, that had not been explored before. The well-tested H_2 potential may then be applied to re-examine the H+H scattering dynamics and for the first time determine a value of the scattering length including effects of adiabatic, non-adiabatic, relativistic and QED with contributions up to $m\alpha^6$. Via this way the precision measurement

7. PRECISION MEASUREMENT OF QUASI-BOUND RESONANCES IN H_2 AND THE $H + H$ SCATTERING LENGTH

of the quasi-bound resonances provides detailed quantitative information on atomic scattering that uniquely bridges the gap between the ultracold physics of atomic hydrogen towards the chemical formation of molecular hydrogen.

7.2 Experimental

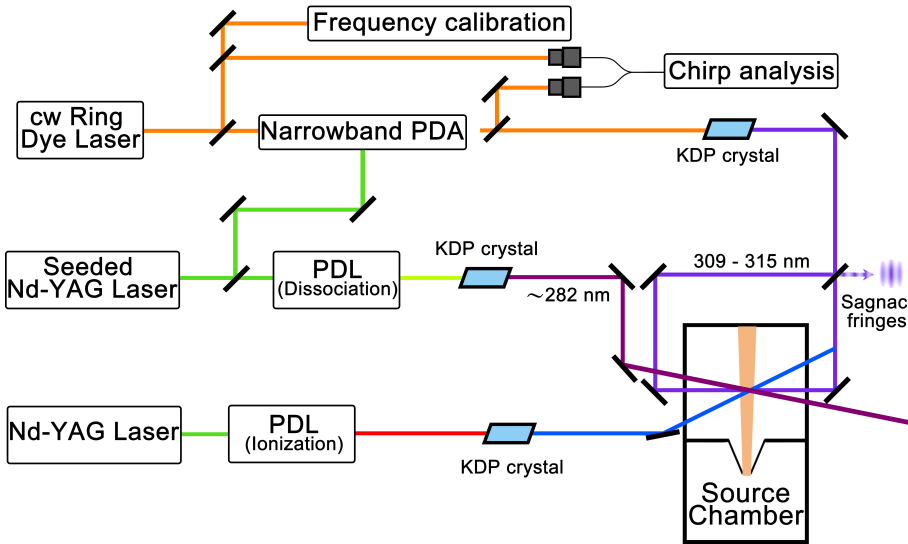
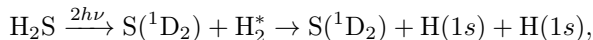


Figure 7.1: Layout of the experimental setup involving three independently tunable UV-lasers, and a molecular beam apparatus. For details see text.

The experimental setup, displayed in some detail in Fig. 7.1, is essentially similar to the one used previously for the detection of bound resonances below the dissociation threshold [84, 85, 222]. Two-photon UV-photolysis proceeds via the path:



where H_2^* signifies a quasi-bound resonance existing as an intermediate reaction product before tunneling and disintegrating in two $H(1s)$ atoms. To illustrate the efficiency of this excitation scheme regarding the production of the shape resonances, the potential energy surface of the electronic ground state of H_2S is displayed in Fig. 7.2, as a function of the $S-H_2$ and $H-H$ distance. The minimum of the potential is located around $R_{S-H_2} \approx 1.7 a_0$ and $R_{H-H} \approx 3.6 a_0$.

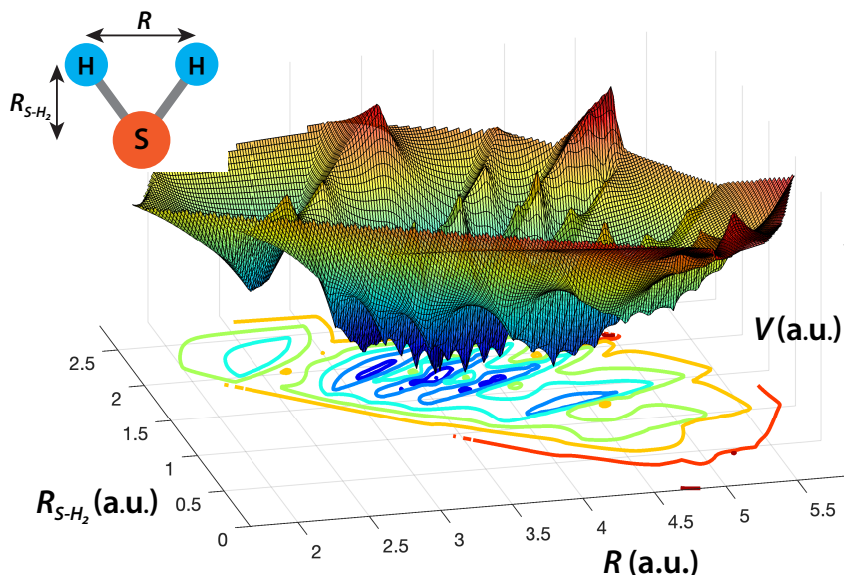


Figure 7.2: Potential energy surface for the electronic ground states of H_2S [220] as a function of the H-H (R) and S- H_2 distance.

Comparing this with the potential energy curve of the electronic ground state of H_2 (see lower part of Fig. 7.2), it can be seen that the second classical turning point is located at a similar value of $R_{\text{H-H}}$, with the corresponding maximal amplitude of the radial wave function. This minute change of the proton-proton distance explains the efficient production of the shape resonances, in line with the Franck-Condon principle.

An excitation spectrum of the H_2S molecule, probed via 2+1 UV resonance-enhanced multi-photon ionization is shown in Fig. 7.3. Two relatively strong and broad resonances, at excitation wavelengths between 276 and 292 nm, are observed in the H_2S^+ ion channel, and are therefore associated with excited states in H_2S . The sharp resonances, labeled with asterisks, are identified as strong S^+ ion signals from two-photon excitation of the S-atom, (^4S) $6p\ ^5\text{P}_1$, (^2D) $4p\ ^1\text{P}_1$, (^2D) $4p\ ^3\text{D}_1$ and (^2D) $4p\ ^1\text{F}_3 - 3p^4\ ^1\text{D}_2$ [245]. Production and precision spectroscopy of S atoms resulting from H_2S photolysis was investigated previously in our setup under similar conditions [246]. The strongest two resonances peaking at excitation energies of $68700\ \text{cm}^{-1}$ and $70900\ \text{cm}^{-1}$ are assigned as two-photon excitation to $4p\ ^1\text{B}_1$ (100) and $3d\ ^1\text{B}_2$, respectively. Processes related to the first level have been discussed extensively by Steadman

7. PRECISION MEASUREMENT OF QUASI-BOUND RESONANCES IN H_2 AND THE $\text{H} + \text{H}$ SCATTERING LENGTH

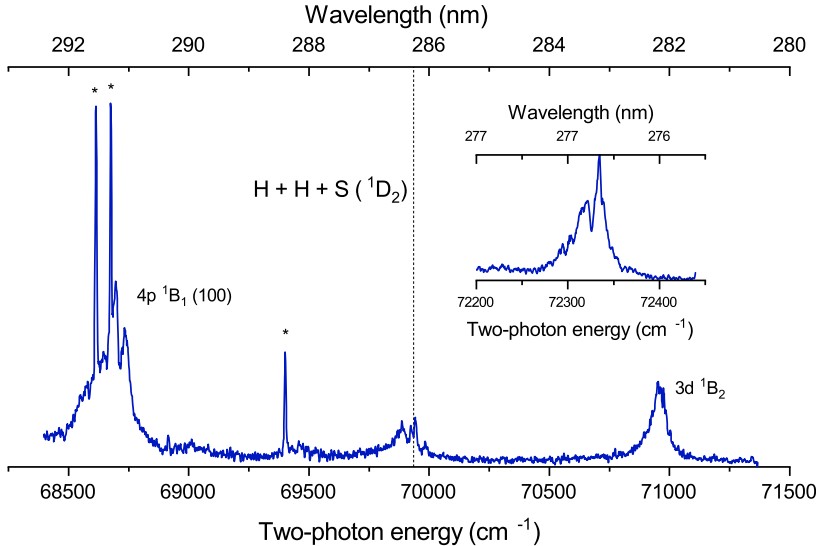


Figure 7.3: Two-photon excitation spectrum of the H_2S molecule with probing of H_2S^+ ion species. The three narrow signals labeled with asterisk corresponding to two-photon transitions in the sulphur atom. See text for details.

et al. [245]. The latter level is based on assignments in the absorption spectrum of Masuko et al. [247]. The selection rule for two-photon transitions from the 1A_1 ground state in H_2S allows to observe 1A_1 , 1A_2 , 1B_1 and 1B_2 , which cover all possible one-photon transitions. Masuko et al. proposed that the broad features peaking at wavelengths of 140.7 nm belong to two overlapping transitions, to $3d^1A_1$ and $3d^1B_2$ at 140.73 nm and 140.90 nm, respectively. However, Mayhew et al. assigned this feature to $3d^1B_2$ with a maximum at 140.72 nm based on the pattern of $n = 4$ in the same Rydberg series [248]. The *ab initio* calculations on H_2S excited state level energies and oscillator strengths have shown that the higher energy $3d^1A_1$ state has a stronger one-photon absorption compared to $3d^1B_2$ [249], in agreement with the assignment in Ref. [247]. The resonance peaking at 281.8 nm in the present work, equivalent to 140.9 nm in one-photon transition, shows a nearly symmetric profile, in contrast with the doublet structure observed in the absorption spectrum. Based on the limited information available, we follow the assignment of Ref. [247]. In addition, a pair of weak doublet structures observed at excitation at wavelengths of 286.0 and 276.5 nm are interpreted as part of a vibrational progression $3d^1B_1$ (000) and (100). Further study is needed to support the assignments.

The photolysis resonance at 291 nm was used for the production and investigation of H_2 molecules in $v = 11$ vibrational states [85]. For the production of H_2 in $v = 13, 14$ levels photolysis on the two-photon resonance at 281.8 nm was employed [222]. In the present experiment the wavelength of the dissociation laser is tuned to this two-photon absorption resonance in H_2S at 281.8 nm, providing sufficient energy to overcome the dissociation energy, at $69935(25) \text{ cm}^{-1}$, for a complete three particle dissociation [81, 82] with an excess of 1000 cm^{-1} above threshold. Here it is noted that by spin selection rules, photolysis of H_2S only produces H_2 molecules in combination with sulphur atoms in the $^1\text{D}_2$ electronically excited state. During all measurements this first photolysis laser is fixed at this wavelength of 281.8 nm, at the peak of the two-photon dissociation resonance of H_2S , for yielding an optimal amount of H_2^* . The excess energy is then released as kinetic energy in the product, giving H_2^* an additional momentum which makes them rapidly escape from the interaction zone. A fly-out time of 20 ns was measured from the interaction zone of the three overlapping UV-lasers.

The H_2^* short-lived resonances are probed in a three laser scheme, where two-photon UV photolysis of H_2S is followed by excitation of H_2^* via two-photon Doppler-free excitation into the $\text{F}^1\Sigma_g^+$, $v = 0$ electronically excited outer well state, denoted as F0 in the following. In the potential energy diagram of the H_2 molecule, depicted in Fig. 7.4, the wave functions of bound and a quasi-bound levels are plotted as a function of internuclear separation and at their respective excitation energies. It illustrates the binding and tunneling of these states, while it also shows the favorable Franck-Condon overlap of their wave functions with the F0 level in the excited outer well. A third UV laser then further excites the F0 population into the autoionization continuum, preferably on a strong autoionization resonance, after which H_2^+ species can be detected for signal recording.

The frequency calibration of the spectroscopy laser, probing the excitation of quasi-bound resonances to the F0-outer well state, is crucial because it determines the accuracy at which the energy of those resonances are determined. This laser is a traveling-wave Pulsed-Dye-Amplifier (PDA) amplifying the output of a continuous-wave (CW) ring-dye-laser, upon-frequency doubling delivering a pulsed output with a frequency bandwidth of $\sim 100 \text{ MHz}$ [95]. The absolute frequency calibration relies on saturated absorption spectroscopy of hyperfine-resolved I_2 using the CW-output of the ring laser as well as a wavemeter (Toptica High-Finesse WSU-30) [250]. Effects of frequency chirp in the pulsed output of the PDA is analysed and corrected for, following established methods [95]. Excitation of the two-photon transitions is established in a Doppler-free geometry with counter-propagating beams aligned in a Sagnac interferometric scheme [166].

The pulse sequences of the UV-lasers, all three with pulse durations $\sim 5 \text{ ns}$,

7. PRECISION MEASUREMENT OF QUASI-BOUND RESONANCES IN H_2 AND THE $H + H$ SCATTERING LENGTH

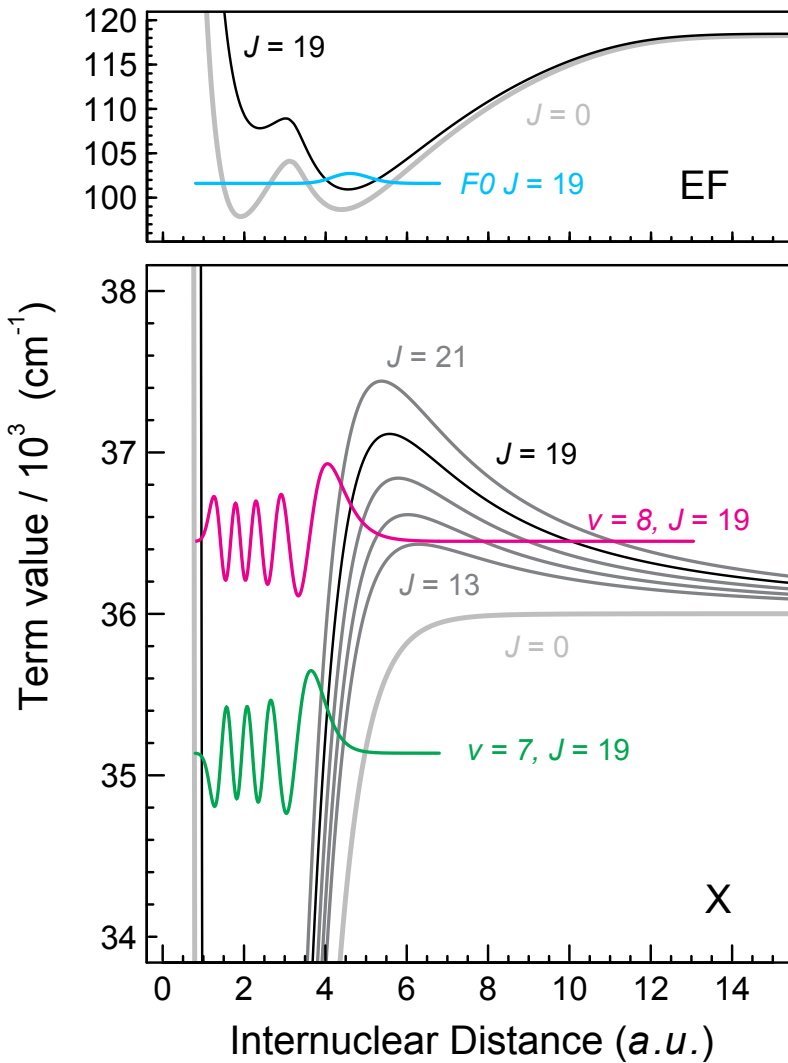


Figure 7.4: Potential energy curves for the $X^1\Sigma_g^+$ ground state and the $EF^1\Sigma_g^+$ excited states, drawn for the $J=0$ rotationless energies and for higher odd J values, including the centrifugal energy. Also wave functions for a bound $X(7,19)$ and quasi-bound $X(8,19)^*$ level are displayed. The wave function for the $F0(J=19)$ excited level (upper panel) indicates overlap at large internuclear separation (4-5 a.u.).

are such that delays of at least 10 ns are imposed to avoid possible AC-Stark effects induced by the photolysis and ionization lasers and to obtain the highest accuracy on the determination of level energies of the quasi-bound resonances. The AC-Stark effects of the spectroscopy laser are systematically investigated with extrapolation to zero-power densities. These procedures lead to measurement of two-photon transition frequencies upon averaging over multiple measurement sequences. The resulting accuracies of the X-EF spectroscopic measurements are discussed in Section 7.4.

For most of the measurements the ion optics are triggered at least 80 ns delayed from the spectroscopy laser, therewith creating a DC-field-free environment. For the weak transitions prompt H_2^+ ions produced from H_2S photolysis are separated by applying a DC-field of 1.3 kV/cm of opposite polarity during excitation. It was experimentally verified that such DC-fields do not cause a Stark shift at the present precision level. This finding is in agreement with calculations based on polarizabilities for the EF state [251] and X state [252], predicting a less than 1 MHz shift for the DC-field used.

7.3 Theory

In support of the experimental studies several calculations are performed. For testing the level structure, and the combination differences between the $\text{X}^1\Sigma_g^+(v, J)^*$ quasi-bound resonances, highly accurate computations are carried out for these levels. For assigning the quantum numbers of the quasi-bound resonances by their $\text{F}^1\Sigma_g^+ - \text{X}^1\Sigma_g^+$ transitions, computations are performed of the F0 levels, at a lower level of precision.

7.3.1 The $\text{X}^1\Sigma_g^+$ state

Level energies for the quasi-bound states are calculated using the nonrelativistic quantum electrodynamics (NRQED) approach, in which relativistic, leading-order radiative and higher-order QED corrections are added to a nonrelativistic Hamiltonian. The nonrelativistic energy is traditionally evaluated within the Born-Oppenheimer (BO) approximation by keeping the position of the nuclei fixed. Because of the light mass of the nuclei with respect to the mass of the electron, the adiabatic correction, scaling with m_e/m_p , and the nonadiabatic correction to the BO approximation are substantial in case of the hydrogen molecule. Nonrelativistic level energies can also be obtained directly by a variational solution of the full four-body Schrödinger equation, without invoking the BO approximation [21, 59, 112, 235]. Such beyond-BO calculations allow to reach an accuracy limited by the uncertainties of the fundamental constants, but are computationally expensive, because a separate variational calculation is needed for every single ro-vibrational level.

Nonadiabatic perturbation theory (NAPT) [52] maintains the computational efficiency of the BO approach through separating the electronic and nuclear Schrödinger equation, while preserving accuracy. This is achieved by including R -dependent corrections to the potential energy curve and by employing R -dependent reduced masses in the nuclear Schrödinger equation, accounting for leading-order nonadiabatic interactions on the order $(m_e/m_p)^2$. These methods were previously explored by Kutzelnigg and coworker [253, 254]. Because no full four-body nonrelativistic energies are available for the quasi-bound states reported here, level energies were obtained using NAPT as presented in Ref. [22].

The radial nuclear Schrödinger equation (in atomic units) within NAPT is given by [22]

$$\left[-\frac{1}{R^2} \frac{\partial}{\partial R} \frac{R^2}{2\mu_{\parallel}(R)} \frac{\partial}{\partial R} + \frac{J(J+1)}{2\mu_{\perp}(R)R^2} + \mathcal{V}(R) \right] \phi_i(R) = E_i \phi_i(R), \quad (7.1)$$

with the R -dependent vibrational (μ_{\parallel}) and rotational (μ_{\perp}) reduced masses

$$\frac{1}{2\mu_{\parallel}(R)} = \frac{1}{2\mu_a} + W_{\parallel}(R), \text{ and} \quad (7.2)$$

$$\frac{1}{2\mu_{\perp}(R)} = \frac{1}{2\mu_a} + W_{\perp}(R), \quad (7.3)$$

with $\mu_a = (m_p + 1)/2$ being the reduced atomic mass. The functions $W_{\parallel}(R)$ and $W_{\perp}(R)$ are defined in Ref. [22] and vanish for $R \rightarrow \infty$. The potential $\mathcal{V}(R)$ is given by

$$\mathcal{V}(R) = \mathcal{E}_{\text{BO}} + \mathcal{E}_{\text{ad}} + \delta\mathcal{E}_{\text{na}}, \quad (7.4)$$

representing the adiabatic [16] and nonadiabatic [17] corrections to the BO potential energy curve [15].

Commonly, a new radial function is defined as $f_i(R) = R\phi_i(R)$ to remove terms involving the first derivative $\partial/\partial R$ in Eq. (7.1), leading to a simplified equation involving only the second derivative and some multiplicative factors. However, because of the R -dependence of $\mu_{\parallel}(R)$, a term $W'_{\parallel}(R)(\partial/\partial R)$ remains, where $W'_{\parallel}(R)$ indicates the first derivative of $W_{\parallel}(R)$ with respect to R . Using the ansatz $\chi_i(R) = R\phi_i(R)\exp\{-Z(R)\}$ in Eq. (7.1) [200, 223], the first derivative term vanishes for $Z(R)$ fulfilling

$$\frac{dZ(R)}{dR} = \mu_{\parallel}W'_{\parallel}(R). \quad (7.5)$$

The radial Schrödinger equation, Eq. (7.1), can then be written as:

$$\left[-\frac{1}{2\mu_{\parallel}(R)} \frac{d^2}{dR^2} - \frac{\mu_{\parallel}(R)}{2} \left(W'_{\parallel}(R) \right)^2 + \frac{1}{2} W''_{\parallel}(R) + \frac{1}{R} W'_{\parallel}(R) + \frac{J(J+1)}{2\mu_{\perp}(R)R^2} + \mathcal{V}(R) \right] \chi_i(R) = E_i \chi_i(R), \quad (7.6)$$

which can be solved using the renormalized Numerov method introduced by Johnson [255].

Relativistic ($m\alpha^4$) and QED ($m\alpha^5$, $m\alpha^6$) corrections were evaluated as described in Ref. [22] using the BO nuclear wavefunction, obtained by solving Eq. (7.6) using the nuclear reduced mass $\mu_n = m_p/2$, $\mathcal{V}(R) = \mathcal{E}_{\text{BO}}$ and $Z(R) = 0$. The nonadiabatic part of the relativistic correction is known to be important and was also included [22], whereas we ignored higher-order QED and finite size corrections, which are below 1 MHz for the states considered here.

The potential energy functions, relativistic and QED corrections, as well as the R -dependent reduced masses and its derivatives were interpolated on a grid with 0.001 a_0 stepsize in the range $0.1a_0$ to $R_{\text{max}} = 25a_0$ using the H2SPECTRE program [22]. The CODATA2018 [110] values were used for the fundamental constants: $E_h = 219474.63136320(43) \text{ cm}^{-1}$, $m_p = 1836.15267343(11)$ and $\alpha = 7.2973525693(11) \times 10^{-3}$.

When comparing the nonadiabatic level energies, relativistic and QED corrections of the bound states obtained by solving Eq. (7.6) with the renormalized Numerov method, we found exact agreement with the results obtained by using H2SPECTRE, which is based on a discrete-variable representation [108]. The current version of H2SPECTRE does however not allow the calculation of quasi-bound states and resonances.

As for the quasi-bound states, resonance positions and widths are determined by calculating the phase shift for a given J by propagating the wave function to large internuclear distance, where

$$\lim_{R \rightarrow \infty} Z(R) = 0 \quad (7.7)$$

and

$$\lim_{R \rightarrow \infty} \chi(R; k) \propto kR(j_J(kR) \cos \eta_J - n_J(kR) \sin \eta_J), \quad (7.8)$$

where j_J and n_J are the spherical Bessel functions and $k = \sqrt{2\mu_a(E - \mathcal{V}(\infty))}$. The phase shift for a given energy $\eta_J(E)$ was derived from the values of the wave function at the two outermost grid points R_a and $R_b = R_{\text{max}}$ using

$$\tan \eta_J = \frac{K j_J(kR_a) - j_J(kR_b)}{K n_J(kR_a) - n_J(kR_b)}; \quad K = \frac{R_a \chi_J(R_b)}{R_b \chi_J(R_a)}. \quad (7.9)$$

The energy grid in the vicinity of a resonance was made adaptive by requiring a certain number of points per phase jump π .

7. PRECISION MEASUREMENT OF QUASI-BOUND RESONANCES IN H_2 AND THE $\text{H} + \text{H}$ SCATTERING LENGTH

Table 7.1: Contributions to the dissociation energies of the observed shape resonances of H_2 in cm^{-1} . A negative dissociation energy indicates that these levels lie above the dissociation threshold. A comparison is made with results from Selg [72].

Contribution / $X(v, J)^*$	(11,13)*	(10,15)*	(9,17)*	(8,19)*	(7,21)*
$m\alpha^2$	-192.2683(29)	-186.1598(36)	-224.5890(40)	-327.0262(43)	-505.4818(45)
adiabatic	3.1895	4.2857	5.3013	6.2827	7.2555
nonadiabatic	2.6847	3.2666	3.6583	3.9268	4.1120
$m\alpha^4$	-0.2254	-0.2945	-0.3540	-0.4076	-0.4570
BO	-0.2261	-0.2952	-0.3546	-0.4081	-0.4575
nonadiabatic	0.0007	0.0006	0.0006	0.0005	0.0004
$m\alpha^5$	-0.0008	0.0002	0.0021	0.0047	0.0079
$m\alpha^6$	-0.0001	-0.0001	-0.0001	-0.0001	-0.0001
Total	-192.4945(29)	-186.4542(36)	-224.9410(40)	-327.4291(43)	-505.9310(45)
Comparison [72]	-192.50	-186.46	-224.95	-327.43	-505.93
Γ_{FWHM} (kHz)	1×10^5	70	1	0.5	1
Lifetime (s)	2×10^{-9}	2×10^{-6}	2×10^{-4}	3×10^{-4}	2×10^{-4}

Resonance parameters are determined within the collision-time-delay approach developed by Smith [224]. For a single channel, the scattering matrix is $S = \exp[2i\eta_J]$ and the time-delay matrix Q is given by

$$Q = -iS^* \frac{dS}{dE} = 2 \frac{d\eta_J}{dE} = \frac{\Gamma}{(E - E_{\text{res}})^2 + (\Gamma/2)^2}, \quad (7.10)$$

where the energy-dependence of the background phase shift has been neglected. The resonance position corresponds to the position of the maximum of Q , i.e., the energy at which $\frac{d\eta_J}{dE}$ is maximal (point of inflexion of the phase-shift curve). The level width is given by

$$\Gamma^{(Q)} = \frac{4}{Q(E_{\text{res}})} = \frac{2}{\left. \frac{d\eta_J}{dE} \right|_{E=E_{\text{res}}}}. \quad (7.11)$$

The quasi-bound states in ortho- H_2 are known to have narrow width [72] and a very fine energy grid would be required to locate an increase of π in the phase shift. To obtain a first estimate of the level positions we choose to extend the effective potential in Eq. (7.4): the maximum height of the centrifugal barrier \mathcal{V}_{bar} at R_{bar} is determined and we set $\mathcal{V}(R > R_{\text{ext}}) = 0.5 \cdot \mathcal{V}_{\text{bar}}$ for R_{ext} being determined when $\mathcal{V}(R_{\text{ext}} > R_{\text{bar}}) = 0.5 \cdot \mathcal{V}_{\text{bar}}$. Under these conditions the quasi-bound states will appear as bound states and can be easily located. Nonadiabatic level energies found using the modified potential agree within 4 MHz for X(11,13)* and to better than 200 kHz for X(7,21)*, X(8,19)*, X(9,17)* and X(10,15)* with the energies found using Eq. (7.10). The nonadiabatic level energies for the five resonances in ortho- H_2 experimentally observed are given in Table 7.1.

The relativistic and QED corrections summarized in Table 7.1 are calculated using the BO nuclear wave functions obtained using the modified potential, which allows to circumvent the use of energy-normalized continuum wave function in the NAPT approach. This is expected to be an excellent approximation for the aimed precision and was verified by a scattering calculation that included the relativistic and QED corrections in Eq. (7.4). Deviations of level positions between 10 and 22 MHz were found, which we attribute to the fact that the nonadiabatic contributions to the relativistic correction (~ 20 MHz) are taken into account at a different level of approximation. The full-width-at-half-maximum (FWHM) is obtained using Eq. (7.11) and is given together with the natural lifetime at the bottom of Table 7.1.

7. PRECISION MEASUREMENT OF QUASI-BOUND RESONANCES IN H_2 AND THE $H + H$ SCATTERING LENGTH

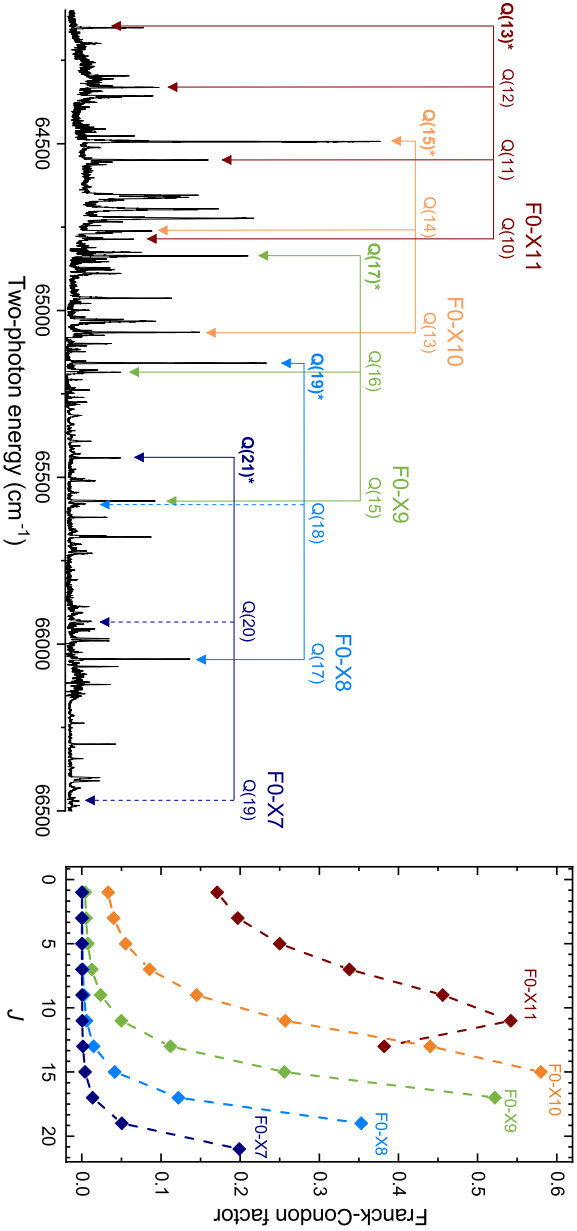


Figure 7.5: (Left): Overview spectra recorded in a two-laser scheme with two-photon UV-photolysis of H_2S , followed by $2+1$ REMPI on F-X(v', v'') bands with a UV-tunable frequency-doubled dye laser. Transitions are labeled with quantum numbers of the ground level. Excitations from quasi bound resonances are indicated with asterisk (*). The dashed arrows represent the calculated positions of unobserved transitions. (Right): Calculated Franck-Condon factors for the bands F-X($0, v''$) as a function of J .

7.4. Detection, identification and precision measurement of the quasi-bound resonances

The theoretical uncertainties are determined by the leading order terms neglected in the NAPT approach, which are estimated by scaling the second-order nonadiabatic $m\alpha^2$ corrections with $1/\mu_n$ [22] and are found to be between 87 and 135 MHz for the quasi-bound states. The computation of binding energies for the H_2^* quasi-bound resonances by Selg [72], at a claimed accuracy of 0.01 cm^{-1} , are found to agree with the present values within 0.01 cm^{-1} (or 300 MHz).

7.3.2 The $\text{F}^1\Sigma_g^+$ state

To predict transition frequencies for the F0-X transitions, term values of the $\text{EF}^1\Sigma_g^+$ electronic state were calculated using Born-Oppenheimer [226], adiabatic [227] and relativistic [14] potential energy curves. Leading order radiative corrections were taken into account by using the corresponding curves of the hydrogen molecular ion [228]. Nonadiabatic energies for the F0 states are reported for $J = 0 - 5$ in Ref. [181] and were obtained from a coupled-equations calculation including several *gerade* states. In the spirit of Ref. [256] the energy difference between the reported nonadiabatic and the current adiabatic term values are parametrized as $\Delta T_{\text{NA}} = a + bJ(J + 1)$, relating a to homogeneous and b to heterogeneous interactions. The found parameters $a = 0.67 \text{ cm}^{-1}$ and $b = -0.009 \text{ cm}^{-1}$ are expected to predict F0 term values with an accuracy of around 1 cm^{-1} . These renewed computations for the $\text{F0}(J)$ levels energies were performed since values for the highest J -levels were lacking in [179]. Based on a comparison with experimental values for $\text{F0}(J)$ at low J [171] the present computations are shown to be more accurate. Values for $\text{F0}(J)$, for the J -values relevant to the present study, are listed in Table 7.2.

7.4 Detection, identification and precision measurement of the quasi-bound resonances

The product distribution of rovibrationally excited states in H_2 , upon two-photon photolysis of H_2S , was first measured in an overview scan in the wavelength range 300 – 310 nm and displayed in Fig. 7.5. The overview spectrum shows many lines in (v', v'') vibrational bands in the $\text{F}^1\Sigma_g^+ - \text{X}^1\Sigma_g^+$ system, detected via 2+1 resonance-enhanced multiphoton ionization. Progressions of $\text{O}(\Delta J = -2)$, $\text{Q}(\Delta J = 0)$ and $\text{S}(\Delta J = 2)$ rotational branches are overlaid, thus forming a dense spectrum.

The assignment of the F0-X transitions originating in quasi-bound resonances is based on a comparison with computed level separations between $\text{X}^1\Sigma_g^+$ and $\text{F}^1\Sigma_g^+$ levels as presented in section 7.3. To obtain the excitation energies of H_2^* above $\text{X}^1\Sigma_g^+(v = 0, J = 0)$ the values for the binding energies

7. PRECISION MEASUREMENT OF QUASI-BOUND RESONANCES IN H₂ AND THE H + H SCATTERING LENGTH

of $X(v, J)$ are augmented with the value for the dissociation energy of H₂, for which the most recent experimental value was taken, $D_0 = 36118.069605$ (31) cm^{-1} [29], which is in excellent agreement with the theoretical value of $D_0 = 36118.069632$ (26) cm^{-1} [236]. From a combination of these values, included in Table 7.2, a prediction can be made for the F0-X transitions probing the quasi-bound resonances. Although the predictions are systematically off by $\sim 1 \text{ cm}^{-1}$ from measurement, they can be considered proof for the assignment of the H₂(v, J)^{*} levels. It is noted that the found deviations from experiment simply reflect the inaccuracy in the *ab initio* calculations for F0(J) levels, which is by itself considered very good for electronically excited states in H₂. The transitions are assigned in Fig. 7.5, where the transitions originating in quasi-bound resonances are marked with an asterisk (*).

7.4. Detection, identification and precision measurement of the quasi-bound resonances

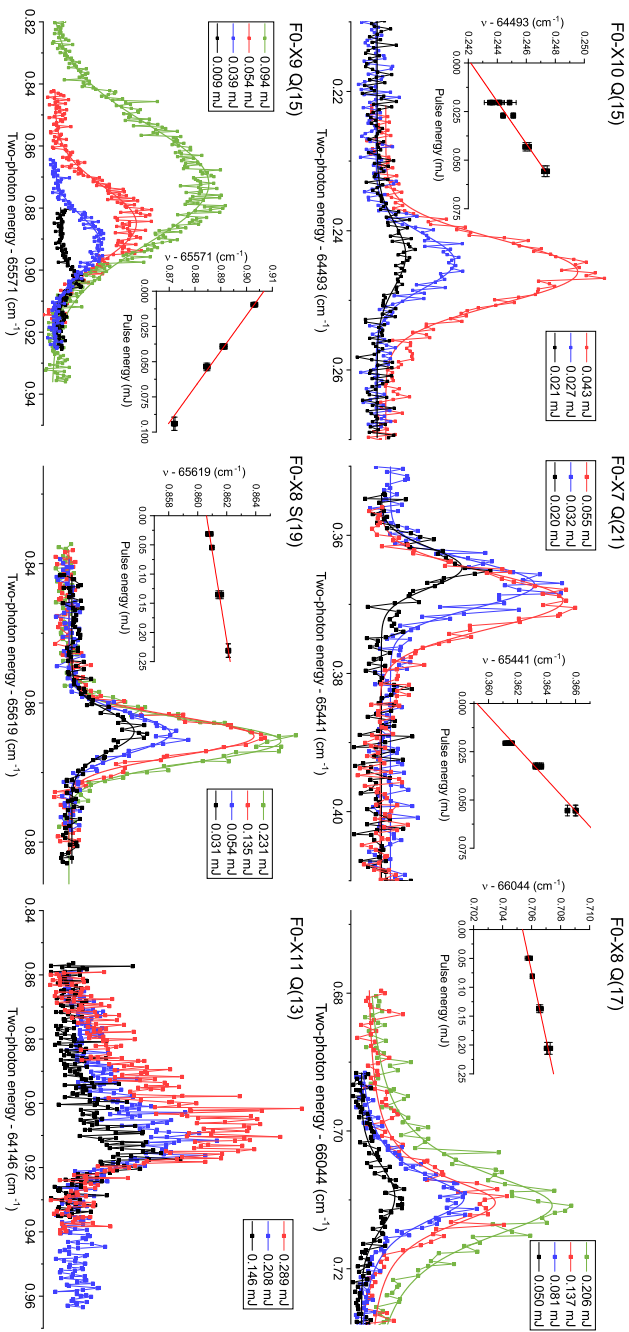


Figure 7.6: Excitation spectra of two photon transitions in the F-X system probing a number of quasi-bound resonances H₂^{*}, including from the X(11,13)^{*} short-lived one, and from the bound state X(9,15). The insets show the AC-Stark extrapolation from measurements at varying pulse energies to zero power levels.

The overview spectrum of Fig. 7.5 shows that the two-photon excitations originating in the H_2^* quasi-bound resonances are markedly more intense than the excitations for the bound resonances at lower rotational quantum number. This apparent deviation of the Franck-Condon principle is a direct consequence of the shift of wave function density of the quasi-bound levels to large internuclear separation (see also Fig. 7.4). A computation of J -dependent Franck-Condon factors for the F0-X transitions, results of which are displayed in Fig. 7.5, show this exquisite behavior. The Franck-Condon factors were calculated using the adiabatic wave functions and using box-normalization for the quasi-bound states. This provides further proof for an unambiguous assignment of the quasi-bound states detected experimentally.

In the experimental configuration with three UV-lasers non-overlapping in time, four quasi-bound resonances, $X(7,21)^*$, $X(8,19)^*$, $X(9,17)^*$ and $X(10,15)^*$, are probed in a precision scheme, with the narrowband PDA-laser detecting the Doppler-free $F^1\Sigma_g^+ - X^1\Sigma_g^+$ two-photon transition. In Fig. 7.6 several examples of the precision frequency measurements are presented, exciting quasi-bound resonances, further referred to as H_2^* , into the electronically excited F0 state, with a subsequent UV pulse for H_2^+ formation and detection. An excitation spectrum from the bound state $X(9,15)$ is also shown. The short-lived $X(11,13)^*$ quasi-bound resonance, with a lifetime of 1.6 ns, was probed in an experimental configuration with a 3 ns separation (and thus in part temporally overlapping) between dissociation laser and the (PDA)-probe laser, yielding a spectrum at low signal-to-noise ratio (see Fig. 7.6).

The spectroscopic measurements are performed for varying intensities allowing for the assessment of the AC-Stark effect in extrapolation to zero field as shown in the insets. All five quasi-bound states have been excited via a Q-transition ($\Delta J = 0$), while some are also probed via S- or O-transitions. The extrapolated zero-intensity values of the highly accurate transition frequencies are compiled in Table 7.2.

For the higher intensities used, the AC-Stark effect is the determining factor in the spectral linewidth, while for the lowest intensities the laser bandwidth of the PDA significantly contributes. The narrowest spectrum obtained is about 200 MHz FWHM, close to the PDA linewidth (including effects of frequency doubling and two-photon excitation). No broadening effect on the spectral line shape as a result of tunneling through the centrifugal barrier was found. Resonances with $X(v, J)^* = (7,21)$, $(8,19)$ and $(9,17)$ are predicted to have lifetimes in excess of 100 μs , while $X(10,15)^*$ lives for 2 μs (see Table 7.1). These lifetimes (short with respect to the bound states) lead to increased natural linewidths, but this is still below the frequency resolution under the present experimental conditions. In fact not even the short-lived $X(11,13)^*$ resonance exhibits a significant line broadening at the present resolution.

7.4. Detection, identification and precision measurement of the quasi-bound

Table 7.2: Measured frequencies for the two-photon F0-X transitions probing the quasi-bound levels H₂^{*}, with uncertainties indicated in parentheses. Also some transitions for bound H₂ levels are included, relevant for comparison. Computed values from the present work for the F0(*J*) levels are listed. Term values of the quasi-bound resonances X(*v*, *J*)^{*} are obtained from the dissociation energies given in Table 7.1 and adding the most recent theoretical values for the dissociation energy $D_0 = 36118.069605(31) \text{ cm}^{-1}$ [29]. For the bound states values from H2SPECTRE [52, 177] are taken. From a combination of these a calculation of two-photon transitions frequencies F0-X can be made. Finally, in the last column the deviations between experimental and predicted frequencies are listed as $\Delta_{\text{Exp.-Calc.}}$. All values in cm^{-1} .

X(<i>v</i> , <i>J</i>)	Transition	Exp.	F0(<i>J</i>) _{calc}	X(<i>v</i> , <i>J</i>) _{calc} [*]	Calculated	$\Delta_{\text{Exp.-Calc.}}$
(7,21) [*]	Q(21)	65 441.3575 (9)	102 064.12	36 624.0006	65 440.12	1.24
(7,21) [*]	O(21)	64 979.430 (10)	101 602.55	36 624.0006	64 978.55	0.88
(8,19) [*]	Q(19)	65 157.9413 (21)	101 602.55	36 445.4988	65 157.05	0.89
(8,19) [*]	S(19)	65 619.8599 (8)	102 064.12	36 445.4988	65 618.62	1.24
(8,19) [*]	O(19)	64 734.8098 (9) ^a	101 179.70	36 445.4988	64 734.20	0.61
(9,17) [*]	Q(17)	64 837.2974 (19)	101 179.70	36 343.0107	64 836.69	0.61
(9,17) [*]	O(17)	64 454.775 (10)	100 797.40	36 343.0107	64 454.39	0.39
(10,15) [*]	O(15)	64 152.970 (20) ^b	100 457.32	36 304.5238	64 152.80	0.17
(10,15) [*]	Q(15)	64 493.2404 (9)	100 797.40	36 304.5238	64 492.88	0.36
(11,13) [*]	Q(13)	64 146.930 (20) ^b	100 457.32	36 310.5641	64 146.76	0.17
(8,17)	Q(17)	66 044.7046 (9)	101 179.70	35 135.6038	66 044.10	0.61
(9,15)	Q(15)	65 571.9063 (19)	100 797.40	35 225.8567	65 571.54	0.36
(9,15)	S(15)	65 954.4505 (10)	101 179.70	35 225.8567	65 953.84	0.61

^a Measured both in DC-field free and in DC-field for prompt ion removal.

^b Measured with 3 ns delay, hence temporal overlap, between dissociation laser and spectroscopy laser.

7. PRECISION MEASUREMENT OF QUASI-BOUND RESONANCES IN H₂ AND THE H + H SCATTERING LENGTH

Table 7.3: Uncertainty budget for the measurements of two-photon F0-X transitions. The uncertainty for the AC-Stark extrapolations is estimated for individual transitions, where the total uncertainties are listed in Table 7.2.

Contribution	Uncertainty (MHz)
Lineshape fitting	15
Frequency calibration	9
CW-pulse offset (chirp)	18
Residual Doppler effect	3
DC-Stark effect	< 1
Subtotal (exl. AC-Stark)	25
AC-Stark effect	3 – 60

The error budget for the frequency calibrations, presented in Table 7.3, contains a variety of contributions. Minor contributions relate to the calibration uncertainty of the cw-laser seeding the PDA, of some 2 MHz, while a residual Doppler shift from misalignment of the counter-propagating beams is reduced by Sagnac interferometry to below 3 MHz uncertainty. The chirp-induced frequency correction accounts for another 4.5 MHz uncertainty. The AC-Stark effect yields the largest contribution to the error budget. It is addressed by performing systematic measurements resulting in the AC-Stark slopes as indicated in Fig. 7.6. The uncertainty associated with AC-Stark results from the extrapolation to zero-power levels and depends on the obtained signal-to-noise ratio for individual lines. In order to reduce the contributions of the AC-Stark effect various campaigns of remeasurement of the Stark-slopes were carried out, thus turning the systematic effect into a statistical distribution of results. For some weak transitions, for example F0-X11 Q(13) and F0-X10 O(15), this could not be done effectively, and only measurements at high laser power were performed leading to larger uncertainties. For each resonance targeted and listed in Table 7.2 the resulting final experimental uncertainty was deduced from the statistical and systematic contributions and by taking them in quadrature. This leads to a variety of resulting uncertainties, mainly associated with the number of measurement campaigns for each line and the obtainable signal-to-noise ratio. For the Q-branch lines an optimum accuracy was obtained at the level of 0.001 cm⁻¹, corresponding to 30 MHz. It is noted that the overall measurement uncertainty has been improved in comparison with previous work [222]; this is related to increased statistical averaging and stronger signal strength resulting from larger FC-factors for the measured transitions.

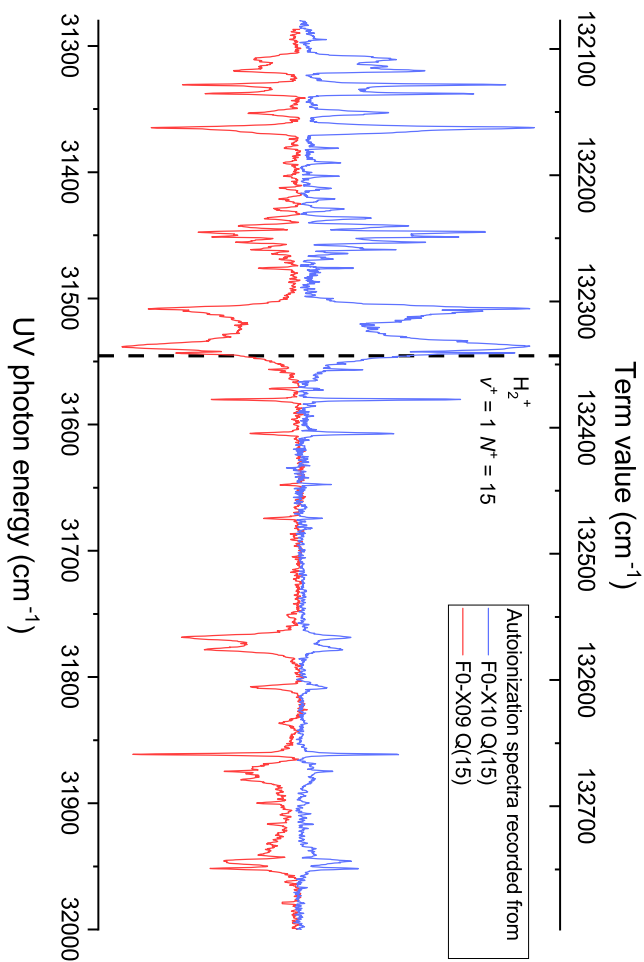


Figure 7.7: Two recordings of autoionization spectra after probing different two-photon transitions in the F-X system, one from the bound X(9,15) state and one from the quasi-bound X(10,15)* resonance. The similarity of the resonances in both spectra and the observation of a Rydberg series converging to the X+($v^+ = 1, N^+ = 15$) limit in H₂⁺ proves that a $J = 15$ state is probed at the intermediate level.

During the recording of the F0-X two-photon transitions by tuning the narrowband PDA-laser (see Fig. 7.6) the third UV-laser is parked on an arbitrary autoionization resonance for optimum H₂⁺ signal generation. Alternatively, when signal is found, either on bound states or on quasi-bound resonances, the wavelength of the third laser may be scanned while keeping the spectroscopy laser fixed. By this means the energy range in H₂ above 130 000 cm⁻¹ is probed relying on autoionization. In Fig. 7.7 autoionization spectra are displayed that were recorded after setting the spectroscopy laser on the two-photon transitions from X(*v* = 9, *J* = 15) bound and X(*v* = 10, *J* = 15)* quasi-bound states. The autoionization spectra are plotted against the term value corresponding to the total excitation energy in the H₂ molecule. The one-to-one correspondence between the autoionization resonances proves that these spectra are taken from an intermediate state with the same angular momentum *J*, thus proving that the quasi-bound resonance has *J* = 15. Note that the small differences in the intensities are caused by the differences in (vibrational) wave function overlap for *v* = 9 and *v* = 10 levels and the ionic states. The fact that an autoionizing Rydberg series is observed converging to the H₂⁺(*v*⁺ = 1, *N*⁺ = 15) provides further evidence that the intermediate state is *J* = 15. Such autoionization spectra were recorded for all quasi-bound resonances, therewith verifying their *J*-quantum numbers. Apart from providing additional proof on the assignment of resonances, this method gives access to H₂ Rydberg states with unprecedentedly high rotational angular momentum of the H₂⁺ ion core, to be explored in future.

7.5 Discussion

Five quasi-bound resonances were detected in a precision experiment. These resonances had previously been observed as terminal levels in emission via the Lyman and Werner bands in studies by Dabrowski [74] and by Roncin and Lounay [75] at an accuracy of 0.05 cm⁻¹. The precision of the present Doppler-free laser excitation study is much improved, by more than an order of magnitude. The novelty of the present work derives not only from the improved accuracy, but also on the fact that the centrifugally bound H₂^{*} resonances could be produced as a transition state in a photolysis process and thereupon detected via 2+1' resonance-enhanced multi-photon ionization before tunneling and separating into two H(1*s*) atoms.

7.5.1 Test of the H₂ potential

Although the quasi-bound resonances were probed in a precision experiment the detection pathway via the F¹Σ_g⁺ outer well state does not provide a means

Table 7.4: Combination differences between H_2^+ quasi-bound resonances, and some bound resonances. Level energies are plotted with respect to the $X(10,15)^*$ resonance. A comparison is made between experimental determination and computed values, while in the last column deviations are given. Note that these discrepancies relate to the inaccuracy in the calculation of $F0(J)$ levels, and not to inaccuracies in the bound and quasi-bound resonances on the ground state potential. All values in cm^{-1} .

$X(v, J)$	$T_{\text{rel}}^{\text{exp}}$	$T_{\text{rel}}^{\text{calc}}$	ΔT
(7,21)*	319.4772 (28)	319.4768 (9)	0.0004 (29)
(8,17)	-1168.9200 (25)	-1168.9200 (12)	0.0000 (28)
(8,19)*	140.9748 (25)	140.9750 (7)	-0.0002 (26)
(9,15)	-1078.6659 (21)	-1078.6671 (11)	0.0012 (24)
(9,17)*	38.4872 (30)	38.4869 (4)	0.0003 (30)
(10,15)*	0	0	0
(11,13)*	6.041 (28)	6.0404 (6)	0.001 (28)

to determine the (negative) binding energy of the resonances in a direct manner. Hence, the accurate first principles computations of $H_2^+(X)$, at an accuracy of $0.003 - 0.004 \text{ cm}^{-1}$ (cf. Table 7.1), cannot directly be compared with observation. In order to make a comparison possible, combination differences between resonances of bound and quasi-bound nature all lying near threshold, have been determined via the level diagram plotted in Fig. 7.8. The energy of all resonances is deduced relative to the $X(10,15)^*$ level and the experimental uncertainties are included via error propagation. Theoretical values for these combination differences are computed and a comparison with experiment is made in Table 7.4. The uncertainty of the higher-order terms in the NAPT approach are related to an interaction with distant electronically excited states. For this reason, the uncertainties for the individual $X(v, J)$ levels are not independent of each other, so that we estimated the accuracy of the calculated intervals by multiplying the non-adiabatic correction of the interval with $1/\mu_n$. Its outcome demonstrates that the deviations between experimental and computed combination differences are well within 0.001 cm^{-1} (30 MHz).

This excellent agreement constitutes a test of the high accuracy of the calculated potential energy curve of H_2 , including all adiabatic, non-adiabatic, relativistic and QED contributions as discussed in section 7.3. The unprecedented experimental accuracy for highly excited vibrational states verifies the computations in the NAPT-framework [52] for the H_2 potential specifically at large internuclear distances.

7. PRECISION MEASUREMENT OF QUASI-BOUND RESONANCES IN H_2 AND THE $\text{H} + \text{H}$ SCATTERING LENGTH

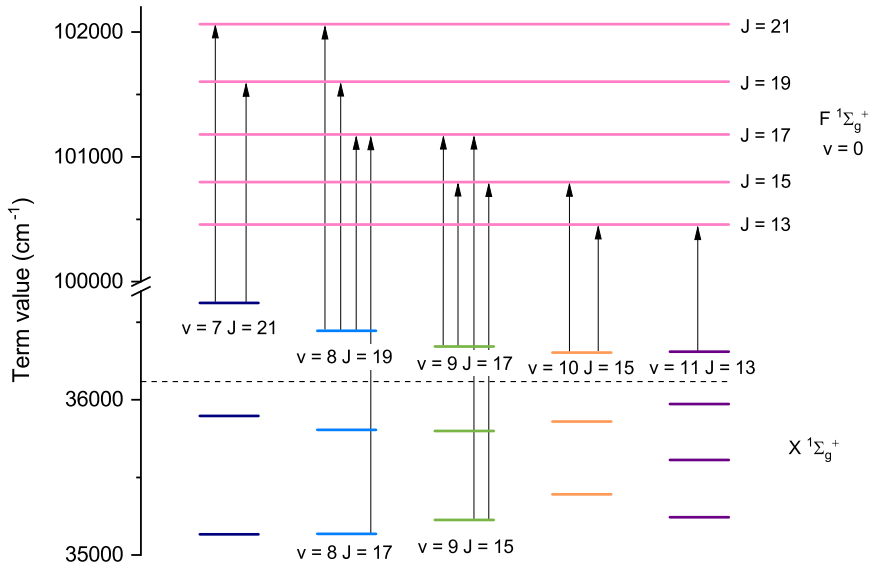


Figure 7.8: Level diagram of $X(v, J)$ and $F0(J)$ rotational levels with the $\text{H}_2(X^1\Sigma_g^+)$ dissociation limit given as a dashed line. Measured transitions, plotted as (black) arrows, connect all the observed quasi-bound resonance including measurements of weak S- and O- transitions. The energy intervals are determined from the combination differences and listed in Table 7.4.

This comes in addition to the tests of the theoretical framework near the bottom part of the H_2 potential. The rotationless fundamental vibrational interval ($\Delta v' = 1 - 0$) in H_2 was measured to an accuracy of 5 MHz in a molecular beam experiment [67]. This experimental value is in agreement within a single standard deviation, both with NAPT (uncertainty of 27 MHz) and with the more precise 4-particle non-Born-Oppenheimer calculation (at 9 MHz uncertainty). The S(3) line in the second overtone ($\Delta v' = 3 - 0$) was measured to high accuracy in Doppler-broadened cavity-ring down spectroscopy [34, 239]. A reanalysis of its collisional line shape, yielding an accuracy of 6 MHz [68], is again found in agreement with theory. The measurement of the first overtone ($\Delta v' = 2 - 0$) reached a lower accuracy of 30 MHz [33], also in agreement with theory. The Q($J = 1, 3, 5, 7$) level intervals for $\Delta v' = 11 - 13$ were determined with an accuracy between 84 and 93 MHz by using combination differences of F-X transitions, also agreeing with NAPT calculations [222]. Measurements of the dissociation energy (D_0) of H_2 also probe the bottom part of the potential. The most recent experimental determinations of $D_0(\text{H}_2)$ [29, 51, 69] are found

to be in agreement with theory [236] at the level of 1 MHz.

The combination of these experimental data allows the first specific test of the H_2 potential energy curves and the R -dependent reduced masses at the 90 MHz level over the entire relevant range of internuclear distances, as illustrated in Fig. 7.9. The upper panel of Fig. 7.9 displays the BO, adiabatic, non-adiabatic, relativistic and QED potential energy curves normalized to ± 1 around $R \approx 2.5 a_0$ for better comparison. The absolute values of the displayed BO, adiabatic and $m\alpha^4$ relativistic potential energy curves normalized to ± 1 amount to $\sim 38293 \text{ cm}^{-1}$, $\sim 18 \text{ cm}^{-1}$ and $\sim 0.9 \text{ cm}^{-1}$, respectively. Similarly, one finds 1.6 GHz, 8 MHz and 0.66 GHz for the $m\alpha^5$, $m\alpha^6$ and the non-adiabatic correction. The middle panel shows the R -dependent reduced vibrational and rotational masses, $\mu_{\parallel}(R)$ and $\mu_{\perp}(R)$, varying smoothly from the nuclear reduced mass at $R \rightarrow 0$, to the atomic reduced mass for $R \rightarrow \infty$. The lower panel displays the squared vibrational wavefunctions of the bound states for $v = 0$ and 3 (black solid line), and the observed X(11,13) quasi-bound state (colored solid line). It can be seen that the previous experimental studies with $v < 3$ tested the potential mainly for R below $2.5 a_0$. For the observed state X(3,2), 99% of the radial probability density is within the interval $[0.9, 2.5]a_0$, whereas the interval $[1, 6.6]a_0$ is presently probed by the X(11,13) state. At $6.6a_0$ the R -dependent reduced rotational and vibrational masses only deviate by 0.0003% and 0.002% from the asymptotic atomic reduced mass, respectively. The various parts of the potential reached their respective asymptotic value to within 2% or less, which amounts to 76 cm^{-1} , 0.09 cm^{-1} and 0.01 cm^{-1} for the BO, adiabatic and relativistic potential and less than 42 MHz for the remaining contributions.

7. PRECISION MEASUREMENT OF QUASI-BOUND RESONANCES IN H_2 AND THE $\text{H} + \text{H}$ SCATTERING LENGTH

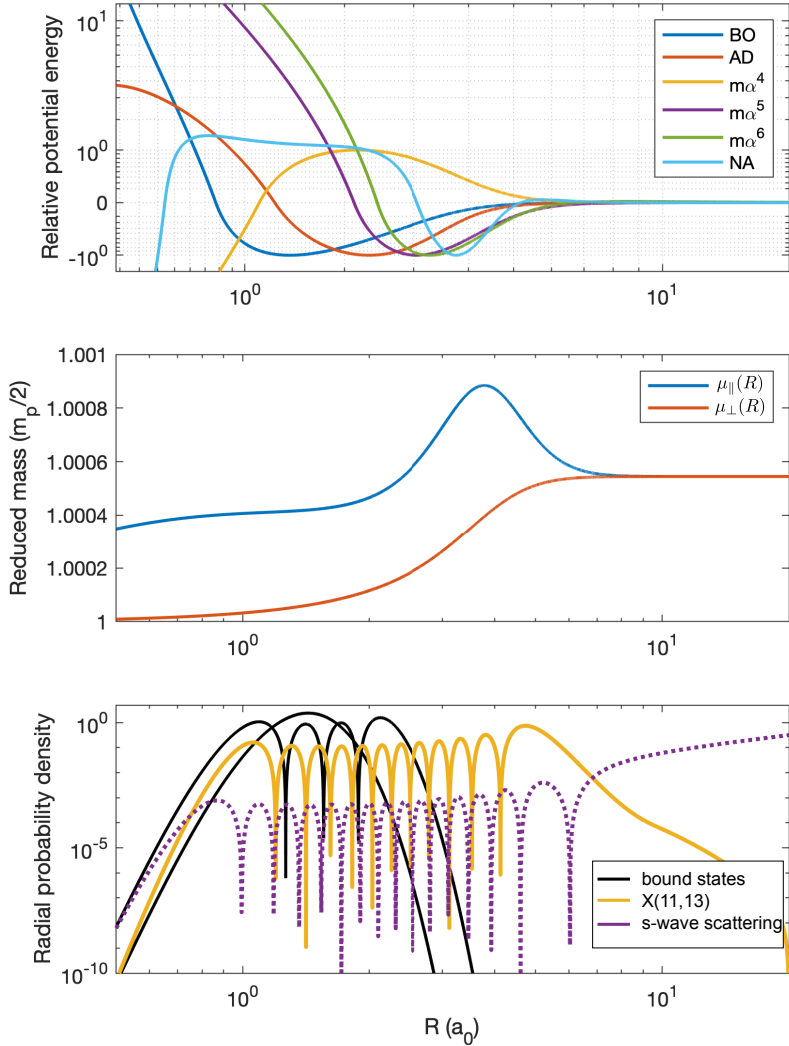


Figure 7.9: Upper panel: Range of the BO potential energy curve and the various corrections normalized to +1 or -1 around the mean internuclear distance for better comparison. Middle panel: R -dependent vibrational and rotational reduced masses, $\mu_{\parallel}(R)$ and $\mu_{\perp}(R)$, used to take non-adiabatic effects into account within the framework of NAPT. Lower panel: Radial probability density of the $v = 0, 3$ bound states (black solid line) and the X(11,13) quasi-bound state (colored solid line). The squared s -wave zero-energy wave function is shown for comparison (dotted line, not to scale).

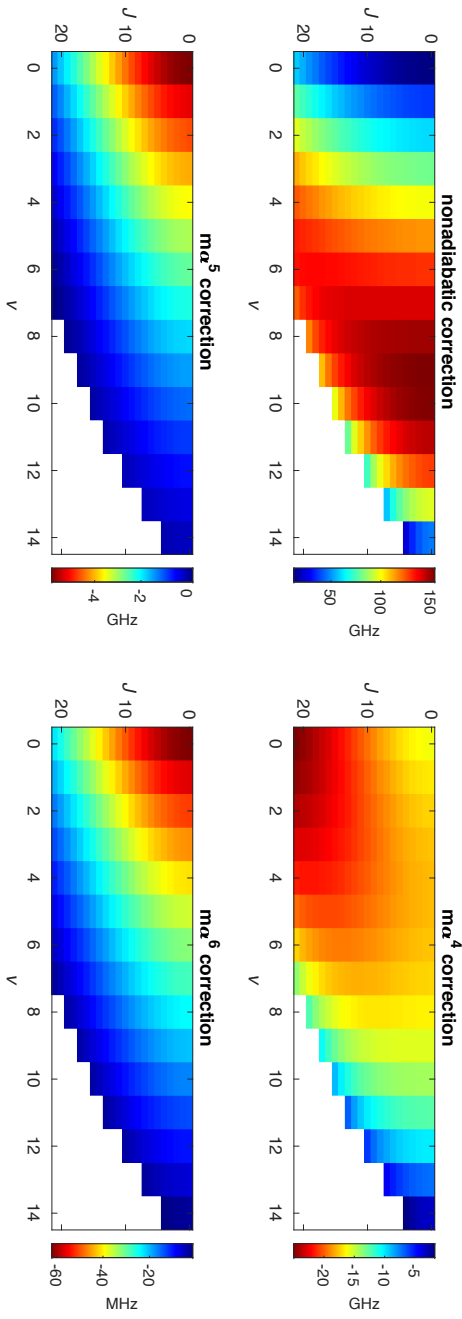


Figure 7.10: Nonadiabatic, ma^4 , ma^5 and ma^6 corrections for the bound states and the long-living quasi-bound states of H_2 for $J = 0 - 21$. Note that the uncertainties for the separate contributions scale with the actual values plotted here (see text).

In view of confronting experimental values for testing theoretical approaches it is illustrative to consider the numerical contributions of the nonadiabatic, relativistic and orders of QED corrections as included in the computations of section 7.3. In Fig. 7.10 the various contributions to the total energy are graphically displayed in a (v, J) color plot. While $m\alpha^n$ ($n = 4-6$) for relativistic and QED-contributions is smallest for the highest v -levels, the non-adiabatic correction has the largest contribution for vibrational levels $v = 7-11$, hence for the quasi-bound states probed in the current experiment. In the same manner Fig. 7.10 illustrates that the $m\alpha^4$ relativistic term is best tested through precision experiments on levels with low- v and high- J as was done previously [225].

It was long understood that the magnitude of the nonadiabatic corrections is related to the vibrational kinetic energy, which reaches its maximum for $v = 9$. That turns the present precision measurement of quasi-bound resonances into a specific test of computations of the non-adiabatic correction term in the computation of H₂ level energies. It should be noted that in Fig. 7.10 the values for the energy contributions are plotted, and that their uncertainties scale with the absolute values [22] ($1/\mu_n, < 2 \times 10^{-4}, 5 \times 10^{-4}, 3 \times 10^{-3}$, respectively).

The dissociation energy sets the most stringent test of the potential energy curves, because it probes the internuclear distances where the corrections are largest, as can be seen by comparing the top and lower panel of Fig. 7.9. The quasi-bound states, however, allow to test the potentials over a much wider range, while being particularly sensitive to the non-adiabatic effects. By scaling the individual potential energy surfaces and repeating the calculation of the dissociation energy D_0 (and quasi-bound intervals, given in brackets), upper limits are found to be: BO: 10^{-9} (5×10^{-7}), AD: 5×10^{-6} (8×10^{-4}), $m\alpha^4$: 6×10^{-4} (2×10^{-2}), $m\alpha^5$: 2×10^{-4} (4×10^{-1}), $m\alpha^6$: 2×10^{-2} (3×10^1) and NA: 1×10^{-3} (1), respectively. Using the quasi-bound intervals we also constrained a relative error of W_{\parallel} and W_{\perp} to 0.05 and 0.002, respectively.

7.5.2 H + H scattering

The H + H scattering process is of fundamental interest in physics, playing a role in the formation of molecular hydrogen in the universe [215], frequency shifts in the hydrogen maser [216], the magnitude of pressure shifts in the 1S-2S transition of atomic hydrogen for a determination of the Rydberg constant [217, 257], and for the formation of a Bose-Einstein condensate in hydrogen [218]. Because of the light atomic mass, non-adiabatic effects are especially important in this collision process and the question about the correct treatment of these was vividly discussed in the literature [230] (and references therein).

The scattering process can be described by a single parameter at low tem-

perature, the scattering length a given by

$$a = - \lim_{k \rightarrow 0} \frac{\tan \eta_{J=0}}{k}. \quad (7.12)$$

Whereas previously reported scattering lengths obtained by different authors within the BO and adiabatic approximations were found to agree, the values for the non-adiabatic scattering length varied between $0.3006 a_0$ and $0.564 a_0$ (see Table 3 in Ref. [230] and references therein), depending on the used reduced masses and effective correction potentials employed to account for the non-adiabatic interactions. Moreover, Wolniewicz attempted a direct solution of the coupled equations [258] but encountered elementary difficulties because of spurious nonadiabatic couplings for $R \rightarrow \infty$ related to the choice of coordinates used to describe molecular states, not suited for the description of the free atoms in the asymptotic region [259].

We choose here the NAPT approach that was experimentally verified with MHz precision up to $R \sim 6.6 a_0$, noting that at this distance the R -dependent masses and all potentials but the BO, adiabatic and relativistic potentials reached their asymptotic value (see section 7.5.1). The squared s-wave scattering wave function is displayed for comparison in the lower panel of Fig. 7.9. A comparison with the radial densities for the bound and quasi-bound states indicates that the whole range of internuclear distances with a significant potential energy term are probed. In addition, as can be seen from the middle panel of Fig. 7.9, the hump in the vibrational reduced mass $\mu_{||}(R)$ is completely located within the interval probed by the resonances, which allows a verification of the main part of the non-adiabatic correction to the scattering length. This allows for the first time to calculate scattering lengths employing an experimentally verified approach for taking the non-adiabatic interactions into account. Using the techniques presented in Section 7.3.1 we integrate the wavefunction outwards at $k_0 = 1 \times 10^{-7}$ a.u. to $R_{\max} = 500 a_0$ and obtain a scattering length for various level of approximation:

$$a = \begin{cases} 0.5699 a_0 & \text{BO} \\ 0.4160 a_0 & \text{AD} \\ 0.2572 a_0 & \text{NA} \\ 0.2735 a_0 & \text{NA}, m\alpha^4, m\alpha^5, m\alpha^6. \end{cases} \quad (7.13)$$

Using the dispersion coefficients for the BO [260] and adiabatic potentials [261] (the exchange interaction is negligible at this distance) we confirm that the asymptotic scattering length is obtained by using the extrapolation procedure given in [262]. The value obtained for the adiabatic scattering length agrees with the value given by Wolniewicz [258]. It is also interesting to note,

that the approximate nonadiabatic scattering length obtained using the atomic reduced mass is $0.2651 a_0$, deviating by only 3% from the value obtained using NAPT. The deviation to previously reported values obtained using the same approximation is related to the improved BO and adiabatic potential energy curves [263].

The obtained scattering lengths are verified by comparing to [264]

$$a = \frac{2\mu_n}{k^2} \int_0^\infty \sin(kR) \mathcal{V}(R) \chi(R; k = k_0) dR, \quad (7.14)$$

and we find agreement at the 0.02% level for the BO and adiabatic level of approximation. As was found in Ref. [263], Eq. (7.14) can also be used to estimate changes of the scattering length δa caused by a change of the potential $\delta \mathcal{V}(R)$, by replacing $\mathcal{V}(R) \rightarrow \delta \mathcal{V}(R)$ and $\sin(kR) \rightarrow \chi(R; k = k_0)$. We find $\delta a^{m\alpha^4} = 0.0156 a_0$, $\delta a^{m\alpha^5} = -0.0007 a_0$ and $\delta a^{m\alpha^6} = 0.0014 a_0$, respectively.

The experimental verification of the NAPT approach for the shape resonances can be used to determine an uncertainty of the scattering length. We studied the change of the scattering length when using the above-mentioned relative uncertainties for the individual parts of the potential or the R -dependent reduced masses. This allows to attribute the experimental uncertainty of the shape-resonance intervals (~ 90 MHz) to only one part of the nuclear Schrödinger equation. It is found that a change of the vibrational reduced mass μ_{\parallel} has the largest effect, resulting in an experimentally verified singlet scattering length of

$$a = 0.2735_{31}^{39} a_0. \quad (7.15)$$

7.6 Conclusion

In the present study five quasi-bound resonances of the H₂ molecule are produced in the two-photon UV photolysis of H₂S, where four of those persist as long-lived transition states. Proof of their production and detection is provided by comparing experimental two-photon transition frequencies to computed level intervals between F¹Σ_g⁺ and X¹Σ_g⁺ levels. Computation of rotational-state dependent Franck-Condon factors, compared with the observation of enhanced intensities, provides further verification of the assignments. Also the step-wise excitation from quasi-bound states into the continuum provides an angular momentum label as supporting evidence.

Highly accurate calculations of X¹Σ_g⁺(v, J) level energies are performed, for which an existing framework of non-adiabatic perturbation theory (NAPT) [52, 177] is extended into the region above the dissociation threshold. The present precision measurement allows for a test of the H₂ potential energy curve, comprising a Born-Oppenheimer potential, adiabatic, non-adiabatic and

relativistic corrections, as well as QED-corrections up to order ma^6 . The H_2 potential is tested now over a wide range of internuclear separations and energies, by comparison of computed level energies to a set of data on infrared transitions, dissociation energy and quasi-bound resonances at MHz accuracy. The precision measurement of the quasi-bound resonances specifically probes and tests the non-adiabatic correction to the H_2 potential. This well-tested H_2 potential can be applied in a computation of the scattering length, resolving a decade old disagreement in the determination of the non-adiabatic singlet s-wave scattering length of the $H(1s) + H(1s)$ collision.

Acknowledgement

The authors thank Prof. Frederic Merkt (ETH Zürich) for discussions motivating this work. This work is financially supported by the European Research Council through an ERC Advanced grant (No: 670168). MB acknowledges NWO for a VENI grant (VI.Veni.202.140).

Summary and outlook

In this thesis, spectroscopic studies on tritium-containing isotopologues and vibrationally excited and quasi-bound states of H_2 are presented.

In the studies of tritium-containing isotopologues, we have determined the fundamental vibration splitting of HT, DT and T_2 using the laser-based technique of Coherent Anti-Stokes Raman Spectroscopy (CARS). The measurement uncertainty achieved is below 0.0005 cm^{-1} for Q-branch transitions, presenting an over 100-times improvement over previous studies in the late 1980's. Additional benchmark measurements on residual D_2 in the DT gas cell were done to support our measurement accuracy. These results also triggered the collaboration with theoreticians to extend the well-developed NAPT calculation scheme to heavier tritium-containing isotopologues. The comparison over experimental values with the latest NAPT calculated values shows good agreement.

In order to push the measurement accuracy with the current experimental setup, quasi-cw CARS and saturated CARS have been explored. By replacing the pulsed probe laser with a continuous-wave laser, the uncertainty arising from the chirp effect is eliminated. However, the signals are greatly reduced which severely hampers precision studies on the limited amount tritium sample. Saturated CARS allows us to achieve sub-Doppler resolution for line center determination. The power requirement for pump and probe laser is large such that ac-Stark broadening causes the line to adopt an asymmetric line profile, which hinders the determination of the central frequency.

Recently, Pachucki and Komasa have published the four-body calculation with variational method for nonrelativistic energy of tritium-containing isotopologues [45], where the leading-order non-adiabatic correction contributes the largest uncertainty in the NAPT scheme. In this novel approach, the uncertainty of nonrelativistic energy is down to 10^{-7} cm^{-1} with the new method and the leading-order QED correction becomes the largest contribution to total uncertainty. This corresponds to about 10^{-5} cm^{-1} for the fundamental vibrational splitting. Obviously, another leap in accuracy of experimental measurement is needed to meet this new state-of-the-art theory. In an alternative approach to study tritium-bearing isotopologues, cavity-enhanced spectroscopy such as the NICE-OHMS technique delivering Doppler-free saturated spectra might bring the measurement uncertainty down to sub-MHz level as was shown recently for HD [265, 266].

For the second part of the thesis, we made use of photodissociation of H_2S to prepare highly ro-vibrationally excited H_2 . These states are probed by F-X transitions using Doppler-free two-photon excitation. In a first study, $v = 13$ and 14 vibrational states have been detected, which lie only tens to hundreds cm^{-1} below the dissociation threshold. The measurement uncertainty for $v = 13$ states is estimated to be $2.4 \times 10^{-3} \text{ cm}^{-1}$. By taking combination differences with precision measurement of $v = 11$ levels, vibrational splittings are determined at about $3 \times 10^{-3} \text{ cm}^{-1}$. Results agree well with the calculated value from the NAPT approach.

In addition, five quasi-bound resonances $(v, J) = (7, 21)^*$, $(8, 19)^*$, $(9, 17)^*$, $(10, 15)^*$ and $(11, 13)^*$, with ns to μs lifetime, have been detected. The unexpected strong signal strength probing these quasi-bound states is explained by the enhanced Franck-Condon factors which were computed. With this advantage, some of S-/O- branches can be measured with similar accuracy. By taking the combination differences of 13 transitions, the relative level energies between these quasi-bound resonances and two bound states, $(8, 17)$ and $(9, 15)$, are determined at an uncertainty of $3 \times 10^{-2} \text{ cm}^{-1}$ for $(11, 13)^*$ and about $3 \times 10^{-3} \text{ cm}^{-1}$ for the others.

The well-developed NAPT calculation scheme on bound states $\text{H}_2 \text{X}^1\Sigma_g^+$ by Pachucki and coworkers is extended to quasi-bound resonances with inclusion of relativistic and QED corrections. The calculation shows excellent agreement with the experimental values obtained. The measurements on these highly ro-vibrationally excited states offer a test on the potential energy at large internuclear distance, in particular for the non-adiabatic contribution. The singlet s-wave scattering length of $\text{H}(1s)+\text{H}(1s)$ collision is also calculated including the leading order non-adiabatic contribution, and $m\alpha^4$, $m\alpha^5$ and $m\alpha^6$ relativistic and QED terms.

Our measurement uncertainty is comparable to the uncertainty of NAPT calculations for the highly excited ro-vibrational states. The measurement uncertainty is limited by the measurement statistics and the ac-Stark analysis. The observed spectral linewidth is close to the theoretical instrumental linewidth, which is about 150 MHz, limited by the pulse width of PDA system. Replacing the PDA system with the comb-locked Ti-Sa system used in the determination of the $\text{GK}^1\Sigma_g^+ - \text{X}^1\Sigma_g^+$ transition [267], with proper frequency mixing, could greatly reduce the spectral linewidth to improve the measurement statistics, as well as the frequency calibration. Nonetheless, the improvement of efficiency of preparing excited states of H_2 will be the major task. The photolysis of H_2S at 281.8 nm is assigned to be a two-photon forbidden $3p \rightarrow 3d$ transition under atomic selection rules and leads to a smaller absorption cross-section. It is worth trying to use shorter wavelength of dissociation laser to search for stronger $3p \rightarrow 4f$ transition of H_2S . Instead of using H_2S , other precursors such as formaldehyde have shown the possibility of producing ro-

vibrationally excited H_2 by one-photon absorption [190]. A better efficiency in producing excited states of H_2 would strongly help in improving measurement uncertainty and exploring the unobserved $v = 14, J = 4$ state with only 0.08 cm^{-1} below the dissociation limit and the quasi-bound resonances with much shorter lifetime. Due to the isotopic shift and smaller zero-point energy for D_2S and HDS , the energy required for complete dissociation of D_2S and HDS is larger than for H_2S . Aside from the efficiency in producing the vibrationally excited states of molecular hydrogen, a stronger two-photon absorption band for D_2S and HDS at shorter wavelength is necessary for the future exploration of the quasi-bound resonances of D_2 and HD .

Bibliography

- [1] A. Züttel, L. Schlapbach, and A. Borgschulte, *History of Hydrogen*, ch. 2, pp. 7–21. John Wiley & Sons, Ltd, 2008.
- [2] H. Cavendish, “Xix. Three papers, containing experiments on factitious air,” *Philos. Trans. R. Soc. Lond.*, vol. 56, pp. 141–184, 1766.
- [3] R. Ramachandran and R. K. Menon, “An overview of industrial uses of hydrogen,” *Int. J. Hydrog. Energy*, vol. 23, no. 7, pp. 593–598, 1998.
- [4] Z. Abdin, A. Zafaranloo, A. Rafiee, W. Mérida, W. Lipiński, and K. R. Khalilpour, “Hydrogen as an energy vector,” *Renew. Sust. Energ. Rev.*, vol. 120, p. 109620, 2020.
- [5] G. Herzberg, *Molecular Spectra and Molecular Structure I: Spectra of Diatomic Molecules*. D. Van Nostrand, 2nd ed., 1950.
- [6] H. M. James and A. S. Coolidge, “The ground state of the hydrogen molecule,” *J. Chem. Phys.*, vol. 1, pp. 825–835, 1933.
- [7] W. Kołos and C. C. J. Roothaan, “Correlated orbitals for the ground state of the hydrogen molecule,” *Rev. Mod. Phys.*, vol. 32, pp. 205–210, 1960.
- [8] W. Kołos and L. Wolniewicz, “Nonadiabatic theory for diatomic molecules and its application to the hydrogen molecule,” *Rev. Mod. Phys.*, vol. 35, pp. 473–483, 1963.
- [9] W. Kołos and L. Wolniewicz, “Accurate adiabatic treatment of the ground state of the hydrogen molecule,” *J. Chem. Phys.*, vol. 41, pp. 3663–3673, 1964.
- [10] W. Kołos and L. Wolniewicz, “Improved theoretical ground-state energy of the hydrogen molecule,” *J. Chem. Phys.*, vol. 49, pp. 404–410, 1968.
- [11] L. Wolniewicz and K. Dressler, “The EF, GK, and $\text{H}\bar{\text{H}}^1\Sigma_g^+$ states of hydrogen. improved ab initio calculation of vibrational states in the adiabatic approximation,” *J. Chem. Phys.*, vol. 82, no. 7, p. 3292, 1985.
- [12] L. Wolniewicz, “Relativistic energies of the ground state of the hydrogen molecule,” *J. Chem. Phys.*, vol. 99, pp. 1851–1868, 1993.
- [13] L. Wolniewicz, “Nonadiabatic energies of the ground state of the hydrogen molecule,” *J. Chem. Phys.*, vol. 103, pp. 1792–1799, 1995.

- [14] L. Wolniewicz, "Relativistic corrections to the energies of the EF, GK, and $\text{H}\bar{\text{H}}\ ^1\Sigma_g^+$ states of the hydrogen molecule," *J. Chem. Phys.*, vol. 109, no. 6, p. 2254, 1998.
- [15] K. Pachucki, "Born-Oppenheimer potential for H_2 ," *Phys. Rev. A*, vol. 82, p. 032509, 2010.
- [16] K. Pachucki and J. Komasa, "Accurate adiabatic correction in the hydrogen molecule," *J. Chem. Phys.*, vol. 141, p. 224103, 2014.
- [17] K. Pachucki and J. Komasa, "Leading order nonadiabatic corrections to rovibrational levels of H_2 , D_2 , and T_2 ," *J. Chem. Phys.*, vol. 143, p. 034111, 2015.
- [18] M. Puchalski, J. Komasa, and K. Pachucki, "Relativistic corrections for the ground electronic state of molecular hydrogen," *Phys. Rev. A*, vol. 95, p. 052506, 2017.
- [19] M. Puchalski, J. Komasa, P. Czachorowski, and K. Pachucki, "Complete $\alpha^6 m$ corrections to the ground state of H_2 ," *Phys. Rev. Lett.*, vol. 117, p. 263002, 2016.
- [20] E. Mátyus and M. Reiher, "Molecular structure calculations: A unified quantum mechanical description of electrons and nuclei using explicitly correlated gaussian functions and the global vector representation," *J. Chem. Phys.*, vol. 137, no. 2, p. 024104, 2012.
- [21] L. M. Wang and Z.-C. Yan, "Relativistic corrections to the ground state of H_2 calculated without using the Born-Oppenheimer approximation," *Phys. Rev. A*, vol. 97, p. 060501, 2018.
- [22] J. Komasa, M. Puchalski, P. Czachorowski, G. Lach, and K. Pachucki, "Rovibrational energy levels of the hydrogen molecule through nonadiabatic perturbation theory," *Phys. Rev. A*, vol. 100, p. 032519, 2019.
- [23] E. E. Witmer, "Critical potentials and the heat of dissociation of hydrogen as determined from its ultra-violet band spectrum," *Phys. Rev.*, vol. 28, pp. 1223–1241, 1926.
- [24] H. Beutler, "The dissociation heats of the hydrogen molecule H_2 , determined at 850 angstrom from the rotation structure on the long-wave border of the absorption continuum," *Zeitschr. f. Phys. Chem.*, vol. 29B, pp. 315–327, 1935.
- [25] G. Herzberg and A. Monfils, "The dissociation energies of the H_2 , HD, and D_2 molecules," *J. Mol. Spectr.*, vol. 5, pp. 482–498, 1961.

-
- [26] E. E. Eyler and N. Melikechi, "Near-threshold continuum structure and the dissociation energies of H₂, HD, and D₂," *Phys. Rev. A*, vol. 48, p. R18, 1993.
- [27] Y. P. Zhang, C. H. Cheng, J. T. Kim, J. Stanojevic, and E. E. Eyler, "Dissociation energies of molecular hydrogen and the hydrogen molecular ion," *Phys. Rev. Lett.*, vol. 92, p. 203003, 2004.
- [28] J. Liu, E. J. Salumbides, U. Hollenstein, J. C. J. Koelemeij, K. S. E. Eikema, W. Ubachs, and F. Merkt, "Determination of the ionization and dissociation energies of the hydrogen molecule," *J. Chem. Phys.*, vol. 130, p. 174306, 2009.
- [29] M. Beyer, N. Hölsch, J. Hussels, C.-F. Cheng, E. J. Salumbides, K. S. E. Eikema, W. Ubachs, C. Jungen, and F. Merkt, "Determination of the interval between the ground states of para- and ortho-H₂," *Phys. Rev. Lett.*, vol. 123, p. 163002, 2019.
- [30] A. Fast and S. A. Meek, "Sub-ppb measurement of a fundamental band rovibrational transition in HD," *Phys. Rev. Lett.*, vol. 125, p. 023001, 2020.
- [31] A. Fast and S. A. Meek, "Precise measurement of the D₂ S₁(0) vibrational transition frequency," *Mol. Phys.*, p. e1999520, 2021.
- [32] A. Campargue, S. Kassi, K. Pachucki, and J. Komasa, "The absorption spectrum of H₂: CRDS measurements of the (2-0) band, review of the literature data and accurate ab initio line list up to 35 000 cm⁻¹," *Phys. Chem. Chem. Phys.*, vol. 14, pp. 802–815, 2012.
- [33] S. Kassi and A. Campargue, "Electric quadrupole transitions and collision-induced absorption in the region of the first overtone band of H₂ near 1.25 μm," *J. Mol. Spectr.*, vol. 300, pp. 55 – 59, 2014.
- [34] C.-F. Cheng, Y. R. Sun, H. Pan, J. Wang, A.-W. Liu, A. Campargue, and S.-M. Hu, "Electric-quadrupole transition of H₂ determined to 10⁻⁹ precision," *Phys. Rev. A*, vol. 85, p. 024501, 2012.
- [35] P. Maddaloni, P. Malara, E. De Tommasi, M. De Rosa, I. Ricciardi, G. Gagliardi, F. Tamassia, G. Di Lonardo, and P. De Natale, "Absolute measurement of the S(0) and S(1) lines in the electric quadrupole fundamental band of D₂ around 3 μm," *J. Chem. Phys.*, vol. 133, p. 154317, 2010.

- [36] S. Kassi, A. Campargue, K. Pachucki, and J. Komasa, "The absorption spectrum of D₂: Ultrasensitive cavity ring down spectroscopy of the (2-0) band near 1.7 μm and accurate ab initio line list up to 24 000 cm^{-1} ," *J. Chem. Phys.*, vol. 136, p. 184309, 2012.
- [37] S. Kassi and A. Campargue, "Electric quadrupole and dipole transitions of the first overtone band of HD by CRDS between 1.45 and 1.33 μm ," *J. Mol. Spectrosc.*, vol. 267, no. 1-2, pp. 36–42, 2011.
- [38] L.-G. Tao, A.-W. Liu, K. Pachucki, J. Komasa, Y. R. Sun, J. Wang, and S.-M. Hu, "Toward a Determination of the Proton-Electron Mass Ratio from the Lamb-Dip Measurement of HD," *Phys. Rev. Lett.*, vol. 120, p. 153001, 2018.
- [39] F. M. J. Cozijn, P. Dupré, E. J. Salumbides, K. S. E. Eikema, and W. Ubachs, "Sub-Doppler frequency metrology in HD for tests of fundamental physics," *Phys. Rev. Lett.*, vol. 120, p. 153002, 2018.
- [40] E. Fasci, A. Castrillo, H. Dinesan, S. Gravina, L. Moretti, and L. Gianfrani, "Precision spectroscopy of HD at 1.38 μm ," *Phys. Rev. A*, vol. 98, p. 022516, 2018.
- [41] K. Pachucki and J. Komasa, "Nonadiabatic corrections to rovibrational levels of H₂," *J. Chem. Phys.*, vol. 130, p. 164113, 2009.
- [42] K. Pachucki and J. Komasa, "Nonadiabatic rotational states of the hydrogen molecule," *Phys. Chem. Chem. Phys.*, vol. 20, pp. 247–255, 2018.
- [43] K. Pachucki and J. Komasa, "Nonrelativistic energy levels of HD," *Phys. Chem. Chem. Phys.*, vol. 20, no. 41, pp. 26297–26302, 2018.
- [44] K. Pachucki and J. Komasa, "Nonrelativistic energy levels of D₂," *Phys. Chem. Chem. Phys.*, vol. 21, no. 20, pp. 10272–10276, 2019.
- [45] K. Pachucki and J. Komasa, "Nonrelativistic energy of tritium-containing hydrogen molecule isotopologues." Submitted to *Mol. Phys.*
- [46] K. Piszczatowski, G. Łach, M. Przybytek, J. Komasa, K. Pachucki, and B. Jeziorski, "Theoretical determination of the dissociation energy of molecular hydrogen," *J. Chem. Theory Comput.*, vol. 5, pp. 3039–3048, 2009.
- [47] K. Pachucki and J. Komasa, "Gerade-ungerade mixing in the hydrogen molecule," *Phys. Rev. A*, vol. 83, p. 042510, 2011.

-
- [48] J. Liu, D. Sprecher, C. Jungen, W. Ubachs, and F. Merkt, "Determination of the ionization and dissociation energies of the deuterium molecule (D_2)," *J. Chem. Phys.*, vol. 132, p. 154301, 2010.
- [49] D. Sprecher, J. Liu, C. Jungen, W. Ubachs, and F. Merkt, "Communication: The ionization and dissociation energies of HD," *J. Chem. Phys.*, vol. 133, p. 111102, 2010.
- [50] R. K. Altmann, L. S. Dreissen, E. J. Salumbides, W. Ubachs, and K. S. E. Eikema, "Deep-ultraviolet frequency metrology of H_2 for tests of molecular quantum theory," *Phys. Rev. Lett.*, vol. 120, p. 043204, 2018.
- [51] C.-F. Cheng, J. Hussels, M. Niu, H. L. Bethlem, K. S. E. Eikema, E. J. Salumbides, W. Ubachs, M. Beyer, N. Hölsch, J. A. Agner, F. Merkt, L.-G. Tao, S.-M. Hu, and C. Jungen, "Dissociation energy of the hydrogen molecule at 10^{-9} accuracy," *Phys. Rev. Lett.*, vol. 121, p. 013001, 2018.
- [52] P. Czachorowski, M. Puchalski, J. Komasa, and K. Pachucki, "Nonadiabatic relativistic correction in H_2 , D_2 , and HD," *Phys. Rev. A*, vol. 98, p. 052506, 2018.
- [53] M. L. E. Oliphant, P. Harteck, and E. Rutherford, "Transmutation effects observed with heavy hydrogen," *Proc. Math. Phys. Eng. Sci.*, vol. 144, no. 853, pp. 692–703, 1934.
- [54] L. W. Alvarez and R. Cornog, "Helium and hydrogen of mass 3," *Phys. Rev.*, vol. 56, pp. 613–613, 1939.
- [55] L. L. Lucas and M. P. Unterweger, "Comprehensive review and critical evaluation of the half-life of tritium," *J. Res. Natl. Inst. Stand. Technol.*, vol. 105, pp. 541–549, 2000.
- [56] S. Kaufman and W. F. Libby, "The natural distribution of tritium," *Phys. Rev.*, vol. 93, pp. 1337–1344, 1954.
- [57] J. D. Happell, G. Östlund, and A. S. Mason, "A history of atmospheric tritium gas (HT) 1950–2002," *Tellus B Chem. Phys. Meteorol.*, vol. 56, no. 3, pp. 183–193, 2004.
- [58] R. J. Pearson, A. B. Antoniazzi, and W. J. Nuttall, "Tritium supply and use: a key issue for the development of nuclear fusion energy," *Fusion Eng. Des.*, vol. 136, pp. 1140–1148, 2018. Special Issue: Proceedings of the 13th International Symposium on Fusion Nuclear Technology (ISFNT-13).

- [59] M. Puchalski, J. Komasa, A. Spyzkiewicz, and K. Pachucki, "Dissociation energy of molecular hydrogen isotopologues," *Phys. Rev. A*, vol. 100, p. 020503, 2019.
- [60] G. H. Dieke and F. S. Tomkins, "The molecular spectrum of hydrogen. the fulcher bands of TH and T₂," *Phys. Rev.*, vol. 76, pp. 283–289, 1949.
- [61] G. H. Dieke, "The molecular spectrum of hydrogen and its isotopes," *J. Mol. Spectrosc.*, vol. 2, pp. 494–517, 1958.
- [62] H. G. M. Edwards, D. A. Long, and H. R. Mansour, "Pure rotational and vibration-rotational raman spectra of tritium, ³H₂," *J. Chem. Soc., Faraday Trans. 2*, vol. 74, pp. 1203–1207, 1978.
- [63] H. G. M. Edwards, D. A. Long, H. R. Mansour, and K. A. B. Najm, "The pure rotational and vibration-rotational Raman spectra of ¹H³H and ²H³H," *J. Raman Spectrosc.*, vol. 8, no. 5, pp. 251–254, 1979.
- [64] D. K. Veirs and G. M. Rosenblatt, "Raman line positions in molecular hydrogen: H₂, HD, HT, D₂, DT, and T₂," *J. Mol. Spectrosc.*, vol. 121, pp. 401–419, 1987.
- [65] M.-C. Chuang and R. N. Zare, "Rotation-vibration spectrum of HT: Line position measurements of the 1-0, 4-0, and 5-0 bands," *J. Mol. Spectrosc.*, vol. 121, no. 2, pp. 380 – 400, 1987.
- [66] T. M. Trivikram, M. Schlösser, W. Ubachs, and E. J. Salumbides, "Relativistic and QED effects in the fundamental vibration of T₂," *Phys. Rev. Lett.*, vol. 120, p. 163002, 2018.
- [67] G. D. Dickenson, M. L. Niu, E. J. Salumbides, J. Komasa, K. S. E. Eikema, K. Pachucki, and W. Ubachs, "Fundamental vibration of molecular hydrogen," *Phys. Rev. Lett.*, vol. 110, p. 193601, 2013.
- [68] P. Weisło, I. E. Gordon, C.-F. Cheng, S.-M. Hu, and R. Ciuryło, "Collision-induced line-shape effects limiting the accuracy in Doppler-limited spectroscopy of H₂," *Phys. Rev. A*, vol. 93, p. 022501, 2016.
- [69] N. Hölsch, M. Beyer, E. J. Salumbides, K. S. E. Eikema, W. Ubachs, C. Jungen, and F. Merkt, "Benchmarking theory with an improved measurement of the ionization and dissociation energies of H₂," *Phys. Rev. Lett.*, vol. 122, no. 10, p. 103002, 2019.
- [70] R. J. LeRoy and R. B. Bernstein, "Dissociation energy and vibrational terms of ground-state (X ¹Σ_g⁺) hydrogen," *J. Chem. Phys.*, vol. 49, no. 10, pp. 4312–4321, 1968.

-
- [71] T. G. Waech and R. B. Bernstein, "Calculated spectrum of quasibound states for $H_2(^1\Sigma_g^+)$ and resonances in $H + H$ scattering," *J. Chem. Phys.*, vol. 46, no. 12, pp. 4905–4911, 1967.
- [72] M. Selg, "Observable quasi-bound states of the H_2 molecule," *J. Chem. Phys.*, vol. 136, no. 11, p. 114113, 2012.
- [73] G. Herzberg and L. L. Howe, "The Lyman bands of molecular hydrogen," *Can. J. Phys.*, vol. 37, no. 5, pp. 636–659, 1959.
- [74] I. Dabrowski, "The Lyman and Werner bands of H_2 ," *Can. J. Phys.*, vol. 62, no. 12, pp. 1639–1664, 1984.
- [75] J.-Y. Roncin and F. Launay, "Atlas of the vacuum ultraviolet emission spectrum of molecular hydrogen," *J. Phys. Chem. Ref. Data, Monograph 4*, pp. 1–443, 1994.
- [76] P. M. Aker, G. J. Germann, and J. J. Valentini, "State-to-state dynamics of $H+HX$ collisions. I. the $H+HX \rightarrow H_2+X$ ($X=Cl,Br,I$) abstraction reactions at 1.6 eV collision energy," *J. Chem. Phys.*, vol. 90, pp. 4795–4808, 1989.
- [77] D. Kliner, K. Rinnen, M. Buntine, D. Adelman, and R. N. Zare, "Product internal-state distribution for the reaction $H + HI \rightarrow H_2+I$," *J. Chem. Phys.*, vol. 95, no. 3, p. 1663, 1991.
- [78] D. Robie, L. Jusinski, and W. Bischel, "Generation of highly vibrationally excited H_2 and detection by 2+1 resonantly enhanced multiphoton ionization," *Appl. Phys. Lett.*, vol. 56, no. 8, pp. 722–724, 1990.
- [79] A. Pomerantz, F. Ausfelder, R. N. Zare, and W. Huo, "Line strength factors for $E, F^1\Sigma_g^+(v' = 0, J' = J'')-X^1\Sigma_g^+(v'', J'')$ (2+1) REMPI transitions in molecular hydrogen," *Can. J. Chem.*, vol. 82, p. 723, 2004.
- [80] J. Steadman and T. Baer, "The production and characterization by resonance enhanced multiphoton ionization of H_2 ($v = 10 - 14$) from photodissociation of H_2S ," *J. Chem. Phys.*, vol. 91, pp. 6113–6119, 1989.
- [81] J. Zhou, Y. Zhao, C. S. Hansen, J. Yang, Y. Chang, Y. Yu, G. Cheng, Z. Chen, Z. He, S. Yu, H. Ding, W. Zhang, G. Wu, D. Dai, C. M. Western, M. N. Ashfold, K. Yuan, and X. Yang, "Ultraviolet photolysis of H_2S and its implications for SH radical production in the interstellar medium," *Nat. Comm.*, vol. 11, p. 1547, 2020.

- [82] Y. Zhao, Z. Luo, Y. Chang, Y. Wu, S.-e. Zhang, Z. Li, H. Ding, G. Wu, J. S. Campbell, C. S. Hansen, S. W. Crane, C. M. Western, M. N. R. Ashfold, K. Yuan, and X. Yang, “Rotational and nuclear-spin level dependent photodissociation dynamics of H₂S,” *Nat. Comm.*, vol. 12, p. 4459, 2021.
- [83] M. L. Niu, E. J. Salumbides, and W. Ubachs, “Communication: Test of quantum chemistry in vibrationally hot hydrogen molecules,” *J. Chem. Phys.*, vol. 143, p. 081102, 2015.
- [84] T. M. Trivikram, M. L. Niu, P. Wcisło, W. Ubachs, and E. J. Salumbides, “Precision measurements and test of molecular theory in highly excited vibrational states of H₂ ($v = 11$),” *Appl. Phys. B*, vol. 122, p. 294, 2016.
- [85] T. M. Trivikram, E. J. Salumbides, C. Jungen, and W. Ubachs, “Excitation of H₂ at large internuclear separation: outer well states and continuum resonances,” *Mol. Phys.*, vol. 117, no. 21, pp. 2961–2971, 2019.
- [86] W. C. Martin, R. Zalubas, and A. Musgrove, “Energy levels of sulfur, S I through S XVI,” *J. Phys. Chem. Ref. Data*, vol. 19, no. 4, pp. 821–880, 1990.
- [87] D. Hanneke, S. Fogwell, and G. Gabrielse, “New Measurement of the Electron Magnetic Moment and the Fine Structure Constant,” *Phys. Rev. Lett.*, vol. 100, no. 12, p. 120801, 2008.
- [88] R. Bouchendira, P. Cladé, S. Guellati-Khélifa, F. Nez, and F. Biraben, “New determination of the fine structure constant and test of the quantum electrodynamics,” *Phys. Rev. Lett.*, vol. 106, p. 080801, 2011.
- [89] R. H. Parker, C. Yu, W. Zhong, B. Estey, and H. Müller, “Measurement of the fine-structure constant as a test of the Standard Model,” *Science*, vol. 360, no. 6385, pp. 191–195, 2018.
- [90] C. G. Parthey, A. Matveev, J. Alnis, B. Bernhardt, A. Beyer, R. Holzwarth, A. Maistrou, R. Pohl, K. Predehl, T. Udem, T. Wilken, N. Kolachevsky, M. Abgrall, D. Rovera, C. Salomon, P. Laurent, and T. W. Hänsch, “Improved Measurement of the Hydrogen $1s^{\circ}2s$ Transition Frequency,” *Phys. Rev. Lett.*, vol. 107, p. 203001, 2011.
- [91] R. Pohl, A. Antognini, F. Nez, F. D. Amaro, F. Biraben, J. M. R. Cardoso, D. S. Covita, A. Dax, S. Dhawan, L. M. P. Fernandes, A. Giesen, T. Graf, T. W. Hänsch, P. Indelicato, L. Julien, C. Y. Kao, P. Knowles, E.-O. L. Bigot, Y.-W. Liu, J. A. M. Lopes, L. Ludhova, C. M. B. Monteiro, F. Mulhauser, T. Nebel, P. Rabinowitz, J. M. F. dos Santos, L. A.

- Schaller, K. Schuhmann, C. Schwob, D. Taqqu, J. F. C. A. Veloso, and F. Kottmann, "The size of the proton," *Nature*, vol. 466, pp. 213–216, 2010.
- [92] J. Shapiro and G. Breit, "Metastability of $2s$ states of hydrogenic atoms," *Phys. Rev.*, vol. 113, pp. 179–181, 1959.
- [93] J. H. Black and A. Dalgarno, "Interstellar H_2 - The population of excited rotational states and the infrared response to ultraviolet radiation," *Astroph. J.*, vol. 203, pp. 132–142, 1976.
- [94] C. Schwartz and R. J. Le Roy, "Nonadiabatic eigenvalues and adiabatic matrix elements for all isotopes of diatomic hydrogen," *J. Mol. Spectrosc.*, vol. 121, pp. 420–439, 1987.
- [95] K. S. E. Eikema, W. Ubachs, W. Vassen, and W. Hogervorst, "Lamb shift measurement in the $1\ ^1S$ ground state of helium," *Phys. Rev. A*, vol. 55, no. 3, p. 1866, 1997.
- [96] M. Schlösser, X. Zhao, M. T. Trivikram, W. Ubachs, and E. J. Salumbides, "Cars spectroscopy of the ($v = 0 \rightarrow 1$) band in T_2 ," *J. Phys. B*, vol. 50, no. 21, p. 214004, 2017.
- [97] S. Xu, R. van Dierendonck, W. Hogervorst, and W. Ubachs, "A dense grid of reference iodine lines for optical frequency calibration in the range 595–655 nm," *J. Mol. Spectrosc.*, vol. 201, no. 2, pp. 256–266, 2000.
- [98] M. S. Fee, K. Danzmann, and S. Chu, "Optical heterodyne measurement of pulsed lasers - toward high-precision pulsed spectroscopy," *Phys. Rev. A*, vol. 45, pp. 4911–4924, 1992.
- [99] S. Gangopadhyay, N. Melikechi, and E. E. Eyler, "Optical phase perturbations in nanosecond pulsed amplification and second-harmonic generation," *J. Opt. Soc. Am. B*, vol. 11, pp. 231–241, 1994.
- [100] S. Hannemann, E. J. Salumbides, S. Witte, R. T. Zinkstok, E. J. van Duijn, K. S. E. Eikema, and W. Ubachs, "Frequency metrology on the $EF^1\Sigma_g^+ - X^1\Sigma_g^+$ (0,0) transition in H_2 , HD, and D_2 ," *Phys. Rev. A*, vol. 74, p. 062514, 2006.
- [101] M. J. Dyer and W. K. Bischel, "Optical Stark shift spectroscopy: Measurement of the $v = 1$ polarizability in H_2 ," *Phys. Rev. A*, vol. 44, pp. 3138–3143, 1991.

- [102] L. A. Rahn and G. J. Rosasco, "Measurement of the density shift of the H_2 $Q(0 - 5)$ transitions from 295 to 1000 K," *Phys. Rev. A*, vol. 41, p. 3698, 1990.
- [103] G. J. Rosasco, A. D. May, W. S. Hurst, L. B. Petway, and K. C. Smyth, "Broadening and shifting of the Raman Q branch of HD," *J. Chem. Phys.*, vol. 90, pp. 2115–2124, 1989.
- [104] G. J. Rosasco, W. J. Bowers, W. S. Hurst, J. P. Looney, K. C. Smyth, and A. D. May, "Simultaneous forward–backward Raman scattering studies of D_2 broadened by D_2 , He, and Ar," *J. Chem. Phys.*, vol. 94, pp. 7625–7633, 1991.
- [105] M. L. Niu, E. J. Salumbides, G. D. Dickenson, K. S. E. Eikema, and W. Ubachs, "Precision spectroscopy of the $X^1\Sigma_g^+$, $v = 0 \rightarrow 1$ ($J = 0 - 2$) rovibrational splittings in H_2 , HD and D_2 ," *J. Mol. Spectr.*, vol. 300, pp. 44–54, 2014.
- [106] M. Puchalski, J. Komasa, and K. Pachucki, "Nuclear spin-spin coupling in HD, HT, and DT," *Phys. Rev. Lett.*, vol. 120, p. 083001, 2018.
- [107] K. Pachucki and J. Komasa, "Rovibrational levels of HD," *Phys. Chem. Chem. Phys.*, vol. 12, pp. 9188–9196, 2010.
- [108] D. T. Colbert and W. H. Miller, "A novel discrete variable representation for quantum mechanical reactive scattering via the S-matrix Kohn method," *J. Chem. Phys.*, vol. 96, pp. 1982–1991, 1992.
- [109] M. Eides, H. Grotch, and V. Shelyuto, "Theory of light hydrogenlike atoms," *Phys. Rep.*, vol. 342, pp. 63–261, 2001.
- [110] E. Tiesinga, P. J. Mohr, D. B. Newell, and B. N. Taylor, "CODATA Recommended Values of the Fundamental Physical Constants: 2018," *J. Phys. Chem. Ref. Data*, vol. 50, no. 3, p. 033105, 2021.
- [111] I. Angeli and K. P. Marinova, "Table of experimental nuclear ground state charge radii: An update," *Atom. Data Nucl. Data*, vol. 99, no. 1, pp. 69–95, 2013.
- [112] M. Puchalski, A. Spyszkiwicz, J. Komasa, and K. Pachucki, "Nonadiabatic relativistic correction to the dissociation energy of H_2 , D_2 , and HD," *Phys. Rev. Lett.*, vol. 121, p. 073001, 2018.
- [113] E. J. Salumbides, J. C. J. Koelemeij, J. Komasa, K. Pachucki, K. S. E. Eikema, and W. Ubachs, "Bounds on fifth forces from precision measurements on molecules," *Phys. Rev. D*, vol. 87, p. 112008, 2013.

-
- [114] J. Biesheuvel, J.-P. Karr, L. Hilico, K. S. E. Eikema, W. Ubachs, and J. C. J. Koelemeij, “Probing QED and fundamental constants through laser spectroscopy of vibrational transitions in HD^+ ,” *Nat. Comm.*, vol. 7, p. 10385, 2016.
- [115] E. J. Salumbides, A. N. Schellekens, B. Gato-Rivera, and W. Ubachs, “Constraints on extra dimensions from precision molecular spectroscopy,” *New J. Phys.*, vol. 17, p. 033015, 2015.
- [116] W. Ubachs, J. C. J. Koelemeij, K. S. E. Eikema, and E. J. Salumbides, “Physics beyond the Standard Model from hydrogen spectroscopy,” *J. Mol. Spectrosc.*, vol. 320, pp. 1 – 12, 2016.
- [117] J. Komasa, K. Piszczatowski, G. Łach, M. Przybytek, B. Jeziorski, and K. Pachucki, “Quantum electrodynamics effects in rovibrational spectra of molecular hydrogen,” *J. Chem. Theory Comput.*, vol. 7, pp. 3105–3115, 2011.
- [118] M. Aker *et al.*, “Improved upper limit on the neutrino mass from a direct kinematic method by KATRIN,” *Phys. Rev. Lett.*, vol. 123, p. 221802, 2019.
- [119] A. Saenz, S. Jonsell, and P. Froelich, “Improved Molecular Final-State Distribution of HeT^+ for the β -Decay Process of T_2 ,” *Phys. Rev. Lett.*, vol. 84, pp. 242–245, 2000.
- [120] N. Doss, J. Tennyson, A. Saenz, and S. Jonsell, “Molecular effects in investigations of tritium molecule β decay endpoint experiments,” *Phys. Rev. C*, vol. 73, p. 025502, 2006.
- [121] L. I. Bodine, D. Parno, and R. Robertson, “Assessment of molecular effects on neutrino mass measurements from tritium β decay,” *Phys. Rev. C*, vol. 91, p. 035505, 2015.
- [122] M. Kleesiek, J. Behrens, G. Drexlin, K. Eitel, M. Erhard, J. A. Formaggio, F. Glück, S. Groh, M. Hötzel, S. Mertens, A. W. P. Poon, C. Weinheimer, and K. Valerius, “ β -Decay spectrum, response function and statistical model for neutrino mass measurements with the KATRIN experiment,” *Eur. Phys. J. C*, vol. 79, p. 204, 2019.
- [123] T. M. James, M. Schlösser, S. Fischer, M. Sturm, B. Bornschein, R. J. Lewis, and H. H. Telle, “Accurate depolarization ratio measurements for all diatomic hydrogen isotopologues: Depolarization ratios for all diatomic hydrogen isotopologues,” *J. Raman Spectrosc.*, vol. 44, pp. 857–865, 2013.

- [124] M. Schlösser, H. Seitz, S. Rupp, P. Herwig, C. G. Alecu, M. Sturm, and B. Bornschein, "In-Line Calibration of Raman Systems for Analysis of Gas Mixtures of Hydrogen Isotopologues with Sub-Percent Accuracy," *Anal. Chem.*, vol. 85, pp. 2739–2745, 2013.
- [125] M. Schloesser, B. Bornschein, S. Fischer, F. Kassel, S. Rupp, M. Sturm, T. James, and H. Telle, "Raman spectroscopy at the tritium laboratory karlsruhe," *Fusion Sci. Technol.*, vol. 67, no. 3, 2015.
- [126] M. Schlösser, X. Zhao, M. T. Trivikram, W. Ubachs, and E. J. Salumbides, "CARS spectroscopy of the ($v = 0 \rightarrow 1$) band in T_2 ," *J. Phys. B*, vol. 50, no. 21, p. 214004, 2017.
- [127] K.-F. Lai, P. Czachorowski, M. Schlösser, M. Puchalski, J. Komasa, K. Pachucki, W. Ubachs, and E. J. Salumbides, "Precision tests of non-adiabatic perturbation theory with measurements on the DT molecule," *Phys. Rev. Research*, vol. 1, p. 033124, 2019.
- [128] A. B. Sazonov and E. P. Magomedbekov, "Hydrogen isotope equilibration induced by tritium radiation - ab initio approach to reaction kinetics," *Fusion Sci. Technol.*, vol. 60, no. 4, pp. 1383–1386, 2011.
- [129] W. M. Jones, "Equilibria in Hydrogen—Tritium Mixtures. Steady States and Initial Reaction Rates at 76.7°K," *J. Chem. Phys.*, vol. 47, pp. 4675–4679, 1967.
- [130] W. M. Tolles, J. W. Nibler, J. R. McDonald, and A. B. Harvey, "A Review of the Theory and Application of Coherent Anti-Stokes Raman Spectroscopy (CARS)," *Appl. Spectrosc.*, vol. 31, pp. 253–271, 1977.
- [131] R. P. Lucht and R. L. Farrow, "Calculation of saturation line shapes and intensities in coherent anti-Stokes Raman scattering spectra of nitrogen," *J. Opt. Soc. Am. B*, vol. 5, pp. 1243–1252, 1988.
- [132] S. Hannemann, E.-J. van Duijn, and W. Ubachs, "A narrow-band injection-seeded pulsed titanium:sapphire oscillator-amplifier system with on-line chirp analysis for high-resolution spectroscopy," *Rev. Scient. Instrum.*, vol. 78, no. 10, p. 103102, 2007.
- [133] S. Stellmer and F. Schreck, "Reservoir spectroscopy of $5s5p\ ^3P_2 - 5snd\ ^3D_{1,2,3}$ transitions in strontium," *Phys. Rev. A*, vol. 90, p. 022512, 2014.
- [134] L. A. Rahn, R. L. Farrow, M. L. Koszykowski, and P. L. Mattern, "Observation of an optical stark effect on vibrational and rotational transitions," *Phys. Rev. Lett.*, vol. 45, pp. 620–623, 1980.

-
- [135] H. Moosmüller, C. Y. She, and W. M. Huo, “Optical Stark effect in the four-wave mixing and stimulated Raman spectra of N₂,” *Phys. Rev. A*, vol. 40, pp. 6983–6998, 1989.
- [136] S. Nazemi, A. Javan, and A. S. Pine, “Collisional effects on the rovibrational transitions of the HD fundamental band,” *J. Chem. Phys.*, vol. 78, pp. 4797–4805, 1983.
- [137] H2SPECTRE ver 7.0 Fortran source code, P. Czachorowski, PhD Thesis, University of Warsaw, Poland, 2019.
- [138] R. P. Lucht and R. L. Farrow, “Saturation effects in coherent anti-Stokes Raman scattering spectroscopy of hydrogen,” *J. Opt. Soc. Am. B*, vol. 6, pp. 2313–2325, 1989.
- [139] A. Owyong and P. Esherick, “Sub-Doppler Raman saturation spectroscopy,” *Opt. Lett.*, vol. 5, pp. 421–423, 1980.
- [140] L. Li, B.-X. Yang, and P. M. Johnson, “Alternating-current stark-effect line shapes in multiphoton ionization spectra,” *J. Opt. Soc. Am. B*, vol. 2, pp. 748–752, 1985.
- [141] R. L. Farrow and L. A. Rahn, “Optical stark splitting of rotational Raman transitions,” *Phys. Rev. Lett.*, vol. 48, pp. 395–398, 1982.
- [142] T. Lundeen, S. Y. Hou, and J. W. Nibler, “Nonresonant third order susceptibilities for various gases,” *J. Chem. Phys.*, vol. 79, pp. 6301–6305, 1983.
- [143] S. Druet, J.-P. Taran, and C. J. Bordé, “Line shape and Doppler broadening in resonant CARS and related nonlinear processes through a diagrammatic approach,” *J. Phys. France*, vol. 40, no. 9, pp. 819–840, 1979.
- [144] G. J. Rosasco and W. S. Hurst, “Measurement of resonant and nonresonant third-order nonlinear susceptibilities by coherent Raman spectroscopy,” *Phys. Rev. A*, vol. 32, pp. 281–299, 1985.
- [145] A. Raj, H.-O. Hamaguchi, and H. A. Witek, “Polarizability tensor invariants of H₂, HD, and D₂,” *J. Chem. Phys.*, vol. 148, p. 104308, 2018.
- [146] J. W. Hahn and E. S. Lee, “Measurement of nonresonant third-order susceptibilities of various gases by the nonlinear interferometric technique,” *J. Opt. Soc. Am. B*, vol. 12, p. 1021, 1995.
- [147] V. Kaufman, “The spectrum of neutral sulfur (S I) in the vacuum ultraviolet,” *Phys. Scripta*, vol. 26, pp. 439–442, 1982.

- [148] V. N. Sarma and Y. N. Joshi, "New lines of atomic sulphur and atomic mercury observed in the vacuum ultraviolet region," *Physica B+C*, vol. 123, pp. 349–352, 1984.
- [149] Y. N. Joshi, M. Mazzoni, A. Nencioni, W. H. Parkinson, and A. Cantu, "Photoabsorption spectrum of atomic sulphur," *J. Phys. B: At. Mol. Phys.*, vol. 20, pp. 1203–1213, 1987. Publisher: IOP Publishing.
- [150] J. Zhou, B. Jones, X. Yang, W. M. Jackson, and C. Y. Ng, "A vacuum ultraviolet laser photoionization and pulsed field ionization study of nascent $S(^3P_{2,1,0})$ and $S(^1D_2)$ formed in the 193.3 nm photodissociation of CS_2 ," *J. Chem. Phys.*, vol. 128, p. 014305, 2008.
- [151] R. Frerichs, "Zum Bogenspektrum des Schwefels," *Z. Phys.*, vol. 80, pp. 150–160, 1933.
- [152] K. W. Meissner, O. Bartelt, and L. Eckstein, "Zur Kenntnis des Schwefel-Bogenspektrums," *Z. Phys.*, vol. 86, pp. 54–76, 1933.
- [153] L. R. Jakobsson, "Infrared spectrum of neutral sulphur atom," *Ark. f. Fysik*, vol. 34, no. 1, p. 19, 1967.
- [154] A. Baćłowski and J. Musielok, "Experimental studies of selected LS-allowed and LS-forbidden transitions of neutral sulfur from the infrared part of the spectrum," *J. Phys. B: Atomic, Molecular and Optical Physics*, vol. 44, p. 135002, 2011.
- [155] T. V. Venkitachalam and A. S. Rao, "Resonance-enhanced multiple-photon ionisation spectroscopy of excited sulphur atoms," *Appl. Phys. B*, vol. 52, pp. 102–107, 1991.
- [156] S. Woutersen, J. B. Milan, W. J. Buma, and C. A. de Lange, "Resonance-enhanced multiphoton-ionization photoelectron spectroscopy of even-parity autoionizing Rydberg states of atomic sulphur," *J. Chem. Phys.*, vol. 106, no. 17, pp. 6831–6838, 1997.
- [157] J. W. McConkey, D. J. Burns, K. A. Moran, and J. A. Kernahan, "Wavelengths and relative A-coefficients for the forbidden lines of atomic sulphur," *Nature*, vol. 217, pp. 538–539, 1968.
- [158] K. B. S. Eriksson, "Observed transitions between the levels of the ground configuration in S I," *Astroph. J.*, vol. 222, p. 398, 1978.
- [159] J. Brown, K. Evenson, and L. Zink, "Atomic sulfur: Frequency measurement of the $J = 0 - 1$ fine-structure transition at 56.3 microns by laser magnetic resonance," *Astrophys. J.*, vol. 431, 1994.

-
- [160] V. Kaufman and W. C. Martin, "Wavelengths and energy level classifications for the spectra of sulfur (S I through S XVI)," *J. Phys. Chem. Ref. Data*, vol. 22, no. 2, pp. 279–375, 1993.
- [161] D. C. Morton, "Atomic data for resonance absorption lines. III. Wavelengths longward of the Lyman limit for the elements hydrogen to gallium," *Astroph. J. Suppl. Series*, vol. 149, pp. 205–238, 2003.
- [162] M. L. Niu, F. Ramirez, E. J. Salumbides, and W. Ubachs, "High-precision laser spectroscopy of the CO $A^1\Pi - X^1\Sigma^+$ (2,0), (3,0), and (4,0) bands," *J. Chem. Phys.*, vol. 142, no. 4, p. 044302, 2015.
- [163] J. Steadman and T. Baer, "The production and spectroscopy of excited sulfur atoms from the two-photon dissociation of H_2S ," *J. Chem. Phys.*, vol. 89, pp. 5507–5513, 1988.
- [164] P. A. Cook, S. R. Langford, R. N. Dixon, and M. N. R. Ashfold, "An experimental and ab initio reinvestigation of the Lyman- α photodissociation of H_2S and D_2S ," *J. Chem. Phys.*, vol. 114, no. 4, pp. 1672–1684, 2001.
- [165] N. Melikechi, S. Gangopadhyay, and E. E. Eyler, "Phase dynamics in nanosecond pulsed dye-laser amplification," *J. Opt. Soc. Am. A*, vol. 11, pp. 2402–2411, 1994.
- [166] S. Hannemann, E. J. Salumbides, and W. Ubachs, "Reducing the first-order Doppler shift in a Sagnac interferometer," *Opt. Lett.*, vol. 32, no. 11, p. 1381, 2007.
- [167] S. N. Dixit, D. A. Levin, and B. V. McKoy, "Resonant enhanced multiphoton ionization studies in atomic oxygen," *Phys. Rev. A*, vol. 37, pp. 4220–4228, 1988.
- [168] W. Ubachs, K. S. E. Eikema, W. Hogervorst, and P. C. Cacciani, "Narrow-band tunable extreme-ultraviolet laser source for lifetime measurements and precision spectroscopy," *J. Opt. Soc. Am. B*, vol. 14, pp. 2469–2476, 1997.
- [169] T. Carette, C. Drag, O. Scharf, C. Blondel, C. Delsart, C. Froese Fischer, and M. Godefroid, "Isotope shift in the sulfur electron affinity: Observation and theory," *Phys. Rev. A*, vol. 81, p. 042522, 2010.
- [170] A. E. Kramida, "The program LOPT for least-squares optimization of energy levels," *Comp. Phys. Comm.*, vol. 182, pp. 419–434, 2011.

- [171] D. Bailly, E. Salumbides, M. Vervloet, and W. Ubachs, "Accurate level energies in the $EF^1\Sigma_g^+$, $GK^1\Sigma_g^+$, $H^1\Sigma_g^+$, $B^1\Sigma_u^+$, $C^1\Pi_u$, $B^1\Sigma_u^+$, $D^1\Pi_u$, $I^1\Pi_g$, $J^1\Delta_g$ states of H_2 ," *Mol. Phys.*, vol. 108, pp. 827–846, 2010.
- [172] T. Lyman, "The spectrum of hydrogen in the region of extremely short wavelengths," *Astroph. J.*, vol. 23, pp. 181–210, 1906.
- [173] G. Herzberg and C. Jungen, "Rydberg series and ionization potential of the H_2 molecule," *J. Mol. Spectrosc.*, vol. 41, pp. 425–486, 1972.
- [174] W. A. Chupka, "Photoionization of molecular Rydberg states: H_2 , $C^1\Pi_u$ and its doubly excited states," *J. Chem. Phys.*, vol. 87, pp. 1488–1498, 1987.
- [175] G. Herzberg, "Quadrupole rotation-vibration spectrum of the hydrogen molecule," *Nature*, vol. 163, p. 170, 1949.
- [176] K. Dressler and L. Wolniewicz, "Improved adiabatic corrections for the $B^1\Sigma_u^+$, $C^1\Pi_u$, and $D^1\Pi_u$ states of the hydrogen molecule and vibrational structures for H_2 , HD, and D_2 ," *J. Chem. Phys.*, vol. 85, no. 5, p. 2821, 1986.
- [177] H2SPECTRE ver 7.0 Fortran source code, University of Warsaw, Poland, 2019.
- [178] E. E. Marinero, R. Vasudev, and R. N. Zare, "The E,F $^1\Sigma_g^+$ double-minimum state of hydrogen: Two-photon excitation of inner and outer wells," *J. Chem. Phys.*, vol. 78, pp. 692–699, 1983.
- [179] G. D. Dickenson, E. J. Salumbides, M. Niu, C. Jungen, S. C. Ross, and W. Ubachs, "Precision spectroscopy of high rotational states in H_2 investigated by Doppler-free two-photon laser spectroscopy in the $EF^1\Sigma_g^+$ - $X^1\Sigma_g^+$ system," *Phys. Rev. A*, vol. 86, p. 032502, 2012.
- [180] E. Reinhold, W. Hogervorst, and W. Ubachs, "Observation of a highly excited long-lived valence state in H_2 ," *Phys. Rev. Lett.*, vol. 78, pp. 2543–2546, 1997.
- [181] S. Yu and K. Dressler, "Calculation of rovibronic structures in the lowest nine excited $^1\Sigma_g^+$ + $^1\Pi_g$ + $^1\Delta_g$ states of H_2 , D_2 , and T_2 ," *J. Chem. Phys.*, vol. 101, no. 9, p. 7692, 1994.
- [182] E. Reinhold, A. de Lange, W. Hogervorst, and W. Ubachs, "Observation of the $I^1\Pi_g$ outer well state in H_2 and D_2 ," *J. Chem. Phys.*, vol. 109, no. 22, pp. 9772–9782, 1998.

-
- [183] W. Kołos, “Ab initio potential energy curves and vibrational levels for the B'' and B' states of the hydrogen molecule,” *J. Mol. Spectr.*, vol. 62, pp. 429–441, 1976.
- [184] A. de Lange, W. Hogervorst, and W. Ubachs, “Double-well states of ungerade symmetry in H₂: First observation and comparison with ab initio calculations,” *Phys. Rev. Lett.*, vol. 86, pp. 2988–2991, 2001.
- [185] E. Reinhold and W. Ubachs, “Heavy Rydberg states,” *Mol. Phys.*, vol. 103, pp. 1329–1352, 2005.
- [186] M. Beyer and F. Merkt, “Observation and calculation of the quasibound rovibrational levels of the electronic ground state of H₂⁺,” *Phys. Rev. Lett.*, vol. 116, p. 093001, 2016.
- [187] M. Beyer and F. Merkt, “Half-collision approach to cold chemistry: Shape resonances, elastic scattering, and radiative association in the H⁺ + H and D⁺ + D collision systems,” *Phys. Rev. X*, vol. 8, p. 031085, 2018.
- [188] N. Mukherjee, W. E. Perreault, and R. N. Zare, “Stark-induced adiabatic Raman ladder for preparing highly vibrationally excited quantum states of molecular hydrogen,” *J. Phys. B*, vol. 50, p. 144005, 2017.
- [189] W. E. Perreault, H. Zhou, N. Mukherjee, and R. N. Zare, “Harnessing the power of adiabatic curve crossing to populate the highly vibrationally excited H₂ ($v = 7, j = 0$) level,” *Phys. Rev. Lett.*, vol. 124, p. 163202, 2020.
- [190] M. S. Quinn, K. Nauta, and S. H. Kable, “Disentangling the H₂ EF(¹Σ_g⁺) ($v' = 0 - 18$) - X (¹Σ_g⁺) ($v'' = 3 - 9$) (2+1) REMPI spectrum via 2D velocity-mapped imaging,” *Mol. Phys.*, vol. 119, no. 1-2, p. e1836412, 2020.
- [191] U. Fantz and D. Wunderlich, “Franck–Condon factors, transition probabilities, and radiative lifetimes for hydrogen molecules and their isotopomers,” *Atomic Data and Nuclear Data Tables*, vol. 92, pp. 853–973, 2006.
- [192] C. Jungen and O. Atabek, “Rovibronic interactions in the photoabsorption spectrum of molecular hydrogen and deuterium: An application of multichannel quantum defect methods,” *J. Chem. Phys.*, vol. 66, pp. 5584–5609, 1977.
- [193] D. Sprecher, C. Jungen, and F. Merkt, “Determination of the binding energies of the np Rydberg states of H₂, HD, and D₂ from high-resolution

- spectroscopic data by Multichannel Quantum-Defect Theory,” *J. Chem. Phys.*, vol. 140, p. 104303, 2014.
- [194] M. Glass-Maujean, C. Jungen, A. Spielfiedel, H. Schmoranzer, I. Tulin, A. Knie, P. Reiss, and A. Ehresmann, “Experimental and theoretical studies of excited states of H₂ observed in the absorption spectrum: I. The 5pπ D'' ¹Π_u state,” *J. Mol. Spectros.*, vol. 293 - 294, pp. 1–10, 2013.
- [195] M. Glass-Maujean, C. Jungen, H. Schmoranzer, I. Tulin, A. Knie, P. Reiss, and A. Ehresmann, “Experimental and theoretical studies of excited states of H₂ observed in the absorption spectrum: II. The 6pπ and 7pπ ¹Π_u states,” *J. Mol. Spectros.*, vol. 293 - 294, pp. 11–18, 2013.
- [196] M. Glass-Maujean, C. Jungen, H. Schmoranzer, I. Tulin, A. Knie, P. Reiss, and A. Ehresmann, “Experimental and theoretical studies of excited states of H₂ observed in the absorption spectrum: III. The 5pσ, 6pσ and 7pσ states,” *J. Mol. Spectros.*, vol. 293 - 294, pp. 19–26, 2013.
- [197] B. Girard, N. Billy, J. Vigue, and J. Lehmann, “Evidence for a dynamical stark effect in CO (A¹Π) two-photon excitation,” *Chem. Phys. Lett.*, vol. 102, no. 2, pp. 168–173, 1983.
- [198] W. M. Huo, K. P. Gross, and R. L. McKenzie, “Optical stark effect in the two-photon spectrum of NO,” *Phys. Rev. Lett.*, vol. 54, pp. 1012–1015, 1985.
- [199] R. J. Le Roy and R. B. Bernstein, “Shape resonances and rotationally predissociating levels: The atomic collision time-delay functions and quasi-bound level properties of H₂ (X¹Σ_g⁺),” *J. Chem. Phys.*, vol. 54, pp. 5114–5126, 1971.
- [200] M. Selg, “A quasi-bound rovibrational state of hydrogen molecule resulting from hyperfine proton-electron spin-spin interaction,” *Eur. Phys. Lett.*, vol. 96, no. 1, p. 10009, 2011.
- [201] E. Fermi, E. Amaldi, O. D’Agostino, F. Rasetti, E. Segrè, and E. Rutherford, “Artificial radioactivity produced by neutron bombardment,” *Proc. Royal Soc. London. Series A*, vol. 146, pp. 483–500, 1934.
- [202] G. Breit and E. Wigner, “Capture of slow neutrons,” *Phys. Rev.*, vol. 49, pp. 519–531, 1936.
- [203] S. Inouye, M. R. Andrews, J. Stenger, H. J. Miesner, D. M. Stamper-Kurn, and W. Ketterle, “Observation of Feshbach resonances in a Bose–Einstein condensate,” *Nature*, vol. 392, pp. 151–154, 1998.

-
- [204] M. Theis, G. Thalhammer, K. Winkler, M. Hellwig, G. Ruff, R. Grimm, and J. H. Denschlag, “Tuning the scattering length with an optically induced Feshbach resonance,” *Phys. Rev. Lett.*, vol. 93, p. 123001, 2004.
- [205] C. Chin, R. Grimm, P. Julienne, and E. Tiesinga, “Feshbach resonances in ultracold gases,” *Rev. Mod. Phys.*, vol. 82, pp. 1225–1286, 2010.
- [206] M. Glass-Maujean, J. Breton, and P. M. Guyon, “Accidental predissociation of the $4p\pi^1\Pi_u^+$ state of H_2 ,” *Phys. Rev. Lett.*, vol. 40, pp. 181–184, 1978.
- [207] C. A. Regal, M. Greiner, and D. S. Jin, “Observation of resonance condensation of fermionic atom pairs,” *Phys. Rev. Lett.*, vol. 92, p. 040403, 2004.
- [208] A. Carrington, C. A. Leach, R. E. Moss, T. C. Steimle, M. R. Viant, and Y. D. West, “Microwave electronic spectroscopy, electric field dissociation and photofragmentation of the H_2^+ ion,” *J. Chem. Soc. Faraday Trans.*, vol. 89, no. 4, pp. 603–614, 1993.
- [209] X.-C. Yao, R. Qi, X.-P. Liu, X.-Q. Wang, Y.-X. Wang, Y.-P. Wu, H.-Z. Chen, P. Zhang, H. Zhai, Y.-A. Chen, and J.-W. Pan, “Degenerate Bose gases near a d-wave shape resonance,” *Nature Physics*, vol. 15, pp. 570–576, 2019.
- [210] M. Gerken, B. Tran, S. Häfner, E. Tiemann, B. Zhu, and M. Weidemüller, “Observation of dipolar splittings in high-resolution atom-loss spectroscopy of 6Li p -wave Feshbach resonances,” *Phys. Rev. A*, vol. 100, p. 050701, 2019.
- [211] L.-H. Li, Y. Hai, B.-K. Lyu, G.-R. Wang, and S.-L. Cong, “Feshbach resonances of nonzero partial waves at different collision energies,” *J. Phys. B*, vol. 54, p. 115201, 2021.
- [212] B. Gao, E. Tiesinga, C. J. Williams, and P. S. Julienne, “Multichannel quantum-defect theory for slow atomic collisions,” *Phys. Rev. A*, vol. 72, p. 042719, 2005.
- [213] K. M. Jones, E. Tiesinga, P. D. Lett, and P. S. Julienne, “Ultracold photoassociation spectroscopy: Long-range molecules and atomic scattering,” *Rev. Mod. Phys.*, vol. 78, pp. 483–535, 2006.
- [214] J. M. Hutson and P. Soldán, “Molecule formation in ultracold atomic gases,” *Int. Rev. Phys. Chem.*, vol. 25, no. 4, pp. 497–526, 2006.

- [215] R. C. Forrey, “Quadrupole association and dissociation of hydrogen in the early Universe,” *J. Phys. B: At. Mol. Opt. Phys.*, vol. 49, p. 194002, 2016.
- [216] J. P. Wittke and R. H. Dicke, “Redetermination of the hyperfine splitting in the ground state of atomic hydrogen,” *Phys. Rev.*, vol. 103, pp. 620–631, 1956.
- [217] A. Matveev, N. Kolachevsky, C. M. Adhikari, and U. D. Jentschura, “Pressure shifts in high-precision hydrogen spectroscopy: II. Impact approximation and Monte-Carlo simulations,” *J. Phys. B*, vol. 52, p. 075006, 2019.
- [218] D. G. Fried, T. C. Killian, L. Willmann, D. Landhuis, S. C. Moss, D. Kleppner, and T. J. Greytak, “Bose-Einstein condensation of atomic hydrogen,” *Phys. Rev. Lett.*, vol. 81, pp. 3811–3814, 1998.
- [219] J. H. Van Vleck, “On the isotope corrections in molecular spectra,” *J. Chem. Phys.*, vol. 4, pp. 327–338, 1936.
- [220] G. Tarczay, A. G. Császár, O. L. Polyansky, and J. Tennyson, “Ab initio rovibrational spectroscopy of hydrogen sulfide,” *J. Chem. Phys.*, vol. 115, no. 3, pp. 1229–1242, 2001.
- [221] Q. Meng, J. Wang, and Y. Mo, “Angle-resolved Beutler-Fano profile and dynamics for the predissociation of H_2 ,” *Phys. Rev. A*, vol. 93, p. 050501, 2016.
- [222] K.-F. Lai, M. Beyer, E. J. Salumbides, and W. Ubachs, “Photolysis production and spectroscopic investigation of the highest vibrational states in H_2 ($X^1\Sigma_g^+ v = 13, 14$),” *J. Phys. Chem. A*, vol. 125, pp. 1221–1228, 2021.
- [223] J. P. Leroy and R. Wallace, “Renormalized Numerov method applied to eigenvalue equations: extension to include single derivative terms and a variety of boundary conditions,” *J. Phys. Chem.*, vol. 89, pp. 1928–1932, 1985.
- [224] F. T. Smith, “Lifetime matrix in collision theory,” *Phys. Rev.*, vol. 118, pp. 349–356, 1960.
- [225] E. J. Salumbides, G. D. Dickenson, T. I. Ivanov, and W. Ubachs, “QED effects in molecules: Test on rotational quantum states of H_2 ,” *Phys. Rev. Lett.*, vol. 107, p. 043005, 2011.

-
- [226] M. Siłkowski, M. Zientkiewicz, and K. Pachucki, “Accurate Born-Oppenheimer potentials for excited Σ^+ states of the hydrogen molecule,” *Adv. Quant. Chem.*, vol. 83, pp. 255–267, 2021.
- [227] L. Wolniewicz and K. Dressler, “Adiabatic potential curves and nonadiabatic coupling functions for the first five excited $^1\Sigma_g^+$ states of the hydrogen molecule,” *J. Chem. Phys.*, vol. 100, no. 1, p. 444, 1994.
- [228] V. I. Korobov, “Ro-vibrational states of H_2^+ . Variational calculations,” *Mol. Phys.*, vol. 116, no. 1, pp. 93–98, 2018.
- [229] B. E. Londoño, J. E. Mahecha, E. Luc-Koenig, and A. Crubellier, “Shape resonances in ground-state diatomic molecules: General trends and the example of RbCs ,” *Phys. Rev. A*, vol. 82, p. 012510, 2010.
- [230] M. J. Jamieson, A. S. Cheung, and H. Ouerdane, “Dependence of the scattering length for hydrogen atoms on effective mass,” *Eur. Phys. J. D*, vol. 56, pp. 181–188, 2010.
- [231] P. Paliwal, N. Deb, D. M. Reich, A. v. d. Avoird, C. P. Koch, and E. Narevicius, “Determining the nature of quantum resonances by probing elastic and reactive scattering in cold collisions,” *Nature Chemistry*, vol. 13, pp. 94–98, 2021.
- [232] W. Kutzelnigg, “Which masses are vibrating or rotating in a molecule?,” *Mol. Phys.*, vol. 105, pp. 2627–2647, 2007.
- [233] W. Heitler and F. London, “Wechselwirkung neutraler Atome und homopolare Bindung nach der Quantenmechanik,” *Zeitschr. f. Phys.*, vol. 44, pp. 455–472, 1927.
- [234] W. Kołos and C. C. J. Roothaan, “Accurate electronic wave functions for the H_2 molecule,” *Rev. Mod. Phys.*, vol. 32, pp. 219–232, 1960.
- [235] B. Simmen, E. Mátyus, and M. Reiher, “Elimination of the translational kinetic energy contamination in pre-Born–Oppenheimer calculations,” *Mol. Phys.*, vol. 111, no. 14–15, pp. 2086–2092, 2013.
- [236] M. Puchalski, J. Komasa, P. Czachorowski, and K. Pachucki, “Non-adiabatic QED Correction to the Dissociation Energy of the Hydrogen Molecule,” *Phys. Rev. Lett.*, vol. 122, p. 103003, 2019.
- [237] G. Herzberg, “Dissociation energy and ionization potential of molecular hydrogen,” *Phys. Rev. Lett.*, vol. 23, pp. 1081–1083, 1969.

- [238] A. Balakrishnan, V. Smith, and B. P. Stoicheff, "Dissociation energy of the hydrogen molecule," *Phys. Rev. Lett.*, vol. 68, pp. 2149–2152, 1992.
- [239] S.-M. Hu, H. Pan, C.-F. Cheng, Y. R. Sun, X.-F. Li, J. Wang, A. Campargue, and A.-W. Liu, "The $v = 3 - 0$ S(0)-S(3) electric quadrupole transitions of H₂ near 0.8 μm ," *Astroph. J.*, vol. 749, p. 76, 2012.
- [240] G. Herzberg, *Spectra of Diatomic molecules, Second edition*. Van Nostrand, 1950.
- [241] O. Oldenberg, "Über den Zerfall von Molekülen durch Rotation," *Z. Phys.*, vol. 56, p. 563–575, 1929.
- [242] E. Bengtsson and R. Rydberg, "The band spectrum of Aluminium hydride," *Z. Phys.*, vol. 59, pp. 540–557, 1930.
- [243] M. Beyer and F. Merkt, "Structure and dynamics of H₂⁺ near the dissociation threshold: A combined experimental and computational investigation," *J. Mol. Spectr.*, vol. 330, pp. 147–157, 2016.
- [244] K.-F. Lai, E. J. Salumbides, W. Ubachs, and M. Beyer, "Shape resonances in H₂ as photolysis reaction intermediates," *Phys. Rev. Lett.*, vol. 127, p. 183001, 2021.
- [245] J. Steadman, S. K. Cole, and T. Baer, "Visible and ultraviolet resonance enhance multiphoton ionization photoelectron spectroscopy of H₂S in the one-photon wavelength region 143–158 nm," *J. Chem. Phys.*, vol. 89, no. 9, pp. 5498–5506, 1988.
- [246] K.-F. Lai, E. J. Salumbides, and W. Ubachs, "Two-photon doppler-free ultraviolet laser spectroscopy on sulphur atoms," *J. Phys. B: At. Mol. Opt. Phys.*, vol. 53, p. 175002, 2020.
- [247] H. Masuko, Y. Morioka, M. Nakamura, E. Ishiguro, and M. Sasanuma, "Absorption spectrum of the H₂S molecule in the vacuum ultraviolet region," *Can. J. Phys.*, vol. 57, no. 5, pp. 745–760, 1979.
- [248] C. A. Mayhew, J.-P. Connerade, M. A. Baig, M. N. R. Ashfold, J. M. Bayley, R. N. Dixon, and J. D. Prince, "High-resolution studies of the electronic spectra of H₂S and D₂S," *J. Chem. Soc., Faraday Trans. 2*, vol. 83, pp. 417–434, 1987.
- [249] M. Pericou-Cayere, M. Gelize, and A. Dargelos, "Ab initio calculations of electronic spectra of H₂S and H₂S₂," *Chemical Physics*, vol. 214, no. 1, pp. 81–89, 1997.

- [250] K.-F. Lai, V. Hermann, T. M. Trivikram, M. Diouf, M. Schlösser, W. Ubachs, and E. J. Salumbides, “Precision measurement of the fundamental vibrational frequencies of tritium-bearing hydrogen molecules: T₂, DT, HT,” *Phys. Chem. Chem. Phys.*, vol. 22, pp. 8973–8987, 2020.
- [251] J. Komasa, “In search for the negative polarizability states - the state of hydrogen molecule,” *Adv. Quant. Chem.*, vol. 48, pp. 151–159, 2005.
- [252] W. Kołos and L. Wolniewicz, “Polarizability of the hydrogen molecule,” *J. Chem. Phys.*, vol. 46, no. 4, pp. 1426–1432, 1967.
- [253] W. Kutzelnigg, “Which masses are vibrating or rotating in a molecule?,” *Mol. Phys.*, vol. 105, no. 19-22, pp. 2627–2647, 2007.
- [254] R. Jaquet and W. Kutzelnigg, “Non-adiabatic theory in terms of a single potential energy surface. The vibration–rotation levels of H₂⁺ and D₂⁺,” *Chem. Phys.*, vol. 346, no. 1, pp. 69–76, 2008.
- [255] B. R. Johnson, “New numerical methods applied to solving the one-dimensional eigenvalue problem,” *J. Chem. Phys.*, vol. 67, pp. 4086–4093, 1977.
- [256] L. Wolniewicz and J. Poll, “On the higher vibration-rotational levels of HD⁺ and H₂⁺,” *Mol. Phys.*, vol. 59, no. 5, pp. 953–964, 1986.
- [257] U. D. Jentschura, C. M. Adhikari, R. Dawes, A. Matveev, and N. Koblachevsky, “Pressure shifts in high-precision hydrogen spectroscopy. I. Long-range atom-atom and atom-molecule interactions,” *J. Phys. B*, vol. 52, p. 075005, 2019.
- [258] L. Wolniewicz and G. Staszewska, “¹Σ_u⁺ - X¹Σ_g⁺ transition moments for the hydrogen molecules,” *J. Mol. Spectr.*, vol. 217, pp. 181–185, 2003.
- [259] A. K. Belyaev, “Revised Born-Oppenheimer approach and a reprojection method for inelastic collisions,” *Phys. Rev. A*, vol. 82, p. 060701, 2010.
- [260] Z.-C. Yan, J. F. Babb, A. Dalgarno, and G. W. F. Drake, “Variational calculations of dispersion coefficients for interactions among H, He, and Li atoms,” *Physical Review A*, vol. 54, pp. 2824–2833, 1996.
- [261] M. Przybytek and B. Jeziorski, “Long-range asymptotic expansion of the diagonal Born–Oppenheimer correction,” *Chem. Phys.*, vol. 401, pp. 170–179, 2012.
- [262] R. Szmytkowski, “Analytical calculations of scattering lengths in atomic physics,” *Journal of Physics A: Mathematical and General*, vol. 28, pp. 7333–7345, 1995.

- [263] M. J. Jamieson and A. Dalgarno, “How a change in the interaction potential affects the s-wave scattering length,” *Journal of Physics B: Atomic, Molecular and Optical Physics*, vol. 31, pp. L219–L222, 1998.
- [264] T. Wu and T. Ohmura, *Quantum Theory of Scattering*. Englewood, NJ: Prentice-Hall, 1962.
- [265] M. L. Diouf, F. M. J. Cozijn, B. Darquié, E. J. Salumbides, and W. Ubachs, “Lamb-dips and Lamb-peaks in the saturation spectrum of HD,” *Opt. Lett.*, vol. 44, p. 4733, 2019.
- [266] M. L. Diouf, F. M. J. Cozijn, K.-F. Lai, E. J. Salumbides, and W. Ubachs, “Lamb-peak spectrum of the HD (2-0) P(1) line,” *Phys. Rev. Research*, vol. 2, p. 023209, 2020.
- [267] J. Hussels, *Improved determination of the dissociation energy of H_2 , HD and D_2* . PhD thesis, Vrije Universiteit Amsterdam, 2021.

List of publications

The following publications are reproduced as chapters in this thesis:

- Chapter 2:** K.-F. Lai, P. Czachorowski, M. Schlösser, M. Puchalski, J. Komasa, K. Pachucki, W. Ubachs, E.J. Salumbides,
"Precision Tests of Nonadiabatic Perturbation Theory with Measurements on the DT Molecule."
Phys. Rev. Res., vol. 1, no. 3, p. 033124, 2019.
- Chapter 3:** K.-F. Lai, V. Hermann, T.M. Trivikram, M. Diouf, M. Schlösser, W. Ubachs, E.J. Salumbides,
"Precision Measurement of the Fundamental Vibrational Frequencies of Tritium-Bearing Hydrogen Molecules: T₂, DT, HT."
Phys. Chem. Chem. Phys. vol. 22, no. 16, pp. 8973–8987, 2020
- Chapter 4:** K.-F. Lai, E.J. Salumbides, W. Ubachs,
"Two-Photon Doppler-Free Ultraviolet Laser Spectroscopy on Sulphur Atoms."
J. Phys. B: At. Mol. Opt. Phys., vol. 53, no. 17, p. 175002, 2020
- Chapter 5:** K.-F. Lai, M. Beyer, E. J. Salumbides, and W. Ubachs,
"Photolysis Production and Spectroscopic Investigation of the Highest Vibrational States in H₂ (X¹Σ_g⁺ v = 13, 14)."
J. Phys. Chem. A, vol. 125, pp. 1221–1228, 2021
- Chapter 6:** K.-F. Lai, M. Beyer, E. J. Salumbides, and W. Ubachs,
"Shape Resonances in H₂ as Photolysis Reaction Intermediates."
Phys. Rev. Lett., vol. 127, p. 183001, 2021
- Chapter 7:** K.-F. Lai, E. J. Salumbides, M. Beyer, and W. Ubachs,
"Precision Measurement of Quasi-Bound Resonances in H₂ and the H+H Scattering Length."
Mol. Phys., p. e2018063, 2021

The author also contributed to the following publications:

- M. L. Diouf, F. M. J. Cozijn, K.-F. Lai, E. J. Salumbides, and W. Ubachs,
“Lamb-peak spectrum of the HD (2-0) P(1) line,”
Phys. Rev. Research, vol. 2, no. 2, p. 023209, 2020
- K.-F. Lai, W. Ubachs, N. De Oliveira, and E. J. Salumbides,
“Fourier-Transform VUV Spectroscopy of $^{14,15}\text{N}$ and $^{12,13}\text{C}$,”
Atoms, vol. 8, no. 3, 2020
- K.-F. Lai, D. Manalili, W. Ubachs, R. Cooke, M. Pettini, N. de Oliveira,
E.J. Salumbides,
“Vacuum UV Fourier-transform spectroscopy of ^{16}O and ^{18}O ,”
Submitted.

Acknowledgment

Throughout the four-year studies, it is full of different challenges. I would like to take this opportunity to express my sincere gratitude to people who support me.

To begin with, I would like to thank my promotor Wim Ubachs for providing me the opportunity to study and work here in Amsterdam. Wim, your knowledge and experience are so valuable to my work. You always come up with different ideas to solve experimental problems and give a new direction to the projects. And I love to hear you sharing the stories in the old times.

To my copromotor Edcel Salumbides, you are a great listener. Whenever we encountered difficulties and felt frustrated, you can always find ways to motivate and inspire us during the difficult times. Sometimes, you are the one to connect the argument from both sides during a heated debate. The creativity and the knowledge to solve experimental problems amazed me a lot. Furthermore, I would like to thank my copromotor Maximillian Beyer. Without your contribution to the theoretical calculation, the work on ro-vibrational excited state of H_2 would not be complete. Your enthusiasm and the knowledge of spectroscopic techniques and molecular theories really surprises me.

To my H_2 lab member, Madhu Trivikram, we had only a few weeks to walk through the experimental setup before you went back India. But it would not be possible to learn the operations of the setup and the programs without your help. Even years later when I have switched to the H_2S project, you have spent time to discuss with me about the previous results and give me directions for the following measurements. Cunfeng Cheng, it is really nice to meet you in Amsterdam. You and Edcel are always a big help in the lab, especially when we are searching for some optics and devices. I enjoy to hear the stories when you were in China. Meissa Diouf, who is also my housemate, you were a master student and working with CARS project when I started my PhD studies. Thanks for helping me both in laboratory work and life in Europe in the early stage. I miss the time we had played basketball at VU and sportcentre. You have a broad range of interests and always can find topics to chat with. Without having you as my housemate, the life would be really dull. Frank Cozijn, you have taught me a lot of knowledge about the vacuum system, cryogenic system and cavity design. I owe you thanks for solving the dirty circulating cooling water problem. Thanks to Joël Hussels for helping out with the YAG lasers and teaching us how to work with your setup. There are too many subtle details on the crystal, the alignment and the power control of pump lasers which are crucial to have a normal operation. Yuanqing Wang, you are a quiet guy as we know. It is grad that we have spend a few months living in same apartment and get to know you more. I wish you all the best in China.

ACKNOWLEDGMENT

This work will not be smooth without the help from our group technician Rob Kortekaas. Big thank to Rob for helping me cleaning up the diffusion pump because dealing with the gas system contaminated with H_2S is a smelly task. Thanks to our secretary Marja Herronen for arranging the admission, the immigration and housing affairs. I would also like to acknowledge the help from the other group members. Thanks to Yuri van der Werf, Raphael Jannin, Kees Steinebach, Maarten Mooij and the colleagues for setting up nice working environment.

I would like to acknowledge our collaborators who contributed to this work. I want to thank Krzysztof Pachucki, Jacek Komasa, Mariusz Puchalski and Paweł Czażchorowski for providing calculations of the tritium-bearing isotopologues level energies. Magnus Schlösser and Valentin Hermann, thank you for assisting the CARS measurement and providing tritium sample. Besides the work at VU, I had opportunity to visit the SOLEIL synchrotron facility in France. I am grateful to Nelson de Oliveira for the help in the measurements.

Last but not the least, I want to thank my family members and friends, who live in Hong Kong, for all the supports and caring.